Austrian Journal of Technical and Natural Sciences

2025, No 5–6

PREMIER Publishing

Vienna
2025

Austrian Journal of Technical and Natural Sciences

Scientific journal

№ 5–6 2025

ISSN 2310-5607

Proofreading Kristin Theissen
Cover design Andreas Vogel
Additional design Stephan Friedman
Editorial office Premier Publishing s.r.o.
Praha 8 – Karlín, Lyčkovo nám. 508/7, PSČ 18600
E-mail: pub@ppublishing.org
Homepage: ppublishing.org

Austrian Journal of Technical and Natural Sciences is an international, English language, peer-reviewed journal. The journal is published in electronic form.

The decisive criterion for accepting a manuscript for publication is scientific quality. All research articles published in this journal have undergone a rigorous peer review. Based on initial screening by the editors, each paper is anonymized and reviewed by at least two anonymous referees. Recommending the articles for publishing, the reviewers confirm that in their opinion the submitted article contains important or new scientific results.

Premier Publishing is not responsible for the stylistic content of the article. The responsibility for the stylistic content lies on an author of an article.

Instructions for authors

Full instructions for manuscript preparation and submission can be found through the Premier Publishing home page at: http://ppublishing.org.

Material disclaimer

The opinions expressed in the conference proceedings do not necessarily reflect those of the Premier Publishing, the editor, the editorial board, or the organization to which the authors are affiliated.

Premier Publishing is not responsible for the stylistic content of the article. The responsibility for the stylistic content lies on an author of an article.

Included to the open access repositories:

TOGETHER WE REACH THE GOAL SJIF 2024 = 6.62 (Scientific Journal Impact Factor Value for 2024).

Included to the Uzbekistan OAK journals bulletin.

The Austrian Journal of Technical and Natural Sciences, No 5–6
ISSN 2310-5607

PREMIER Publishing
ppublishing.org

Section 1. Biology

DOI:10.29013/AJT-25-5.6-3-7

BOTANICAL AND MORPHOLOGICAL CHARACTERISTICS OF POPULUS PRUINOSA

Baltabaev Muratbay Toremuratovich [1], ***Otenova Farida Tolegenovna*** [1], ***Abilova Aizada Azamatovna*** [1]

[1] Nukus State Pedagogical Institute named after Ajiniyaz Republic of Karakalpakstan

Cite: *Baltabaev M.T., Otenova F.T., Abilova A.A. (2025). Botanical and Morphological Characteristics of Populus Pruinosa. Austrian Journal of Technical and Natural Sciences 2025, No. 5–6.* https://doi.org/10.29013/AJT-25-5.6-3-7

Abstract

The article presents a scientific study of the botanical and morphological characteristics of the blue poplar, a tree species growing in Karakalpakstan. A detailed description of the leaves, flowers, bark, shoots, root system and general appearance of the tree is given. Phenological stages such as budding, flowering and leaf fall are clearly defined. Both natural and vegetative methods of reproduction are considered. The species' resistance to salinity and drought, ecological adaptability and importance in the tugai ecosystem are emphasized.

Keywords*: vegetation period, shoot, leaves, stem, bud, swelling seeds, flower, peduncle, root system, vegetative reproduction, stamen, flowering*

Introduction

Poplars belong to the genus *Populus* L. of the *Salicaceae* family (Korovin O. N., Bakhiyev A. B., Tadjitdinov M. T., Sarybayev B.Sh., 1982. 23 p.). This genus includes 17 species in Uzbekistan, and four species of poplars are found in Karakalpakstan. The main and most stable representative of woody plants in the forests of the territory of Karakalpakstan is the poplar tree.

In the recent works of several authors of the "Central Asian Works Guide" for Karakalpakstan, the species of poplar P. *pruinosa* and P. *euphratica* are indicated, mainly in our flora P. *pruinosa* and P. *ariana* grow (Bakhiev A. B., 1974, p. 239–243).

Populus pruinosa has lanceolate, oval, velvety leaves. Branch leaves are bud-shaped, with 3–7 slightly curved teeth, uniformly bluish-green on both sides, smooth, and slightly wrinkled on the petioles. The male catkins are drooping or slanted upwards, bright reddish-brown in color, while the female catkins are egg-shaped and yellow. Its range corresponds to P. *diversifolia* in the north and P. *ariana* in the south. The tree reaches a height of up to 18 meters and a diameter of 80–90 cm.The tip of the tree is

wide, sharp, up to 10 in diameter. The shell is initially brown, green, then yellowish-gray, with deep cracks. Branches are round, green or gray. The shape of the leaf blade changes with age, but the diversity of colors is less noticeable than in other species. The leaf is 3.5 cm long and 4 cm wide, broad, bud-shaped or round, with a wedge-shaped base and 3–7 barely noticeable teeth. It is bluish, hard, and dew-shaped on both sides. The stem length of the branches is 2.1 cm, and they are very wrinkled from the sides. Annual branches are round, crooked, with green, reddish, gray, dew-like, and drooping bark.

The vegetative buds are 7 mm long, elongated, attached to the branch, and brown. The leaves of annual branches are 6–9 cm long and 3–7 cm wide, ovate, with a slightly wedge-shaped and pointed base. The leaf stalks are 1 cm long and curved from the sides. Male flower buds are 12–13 mm long. The inflorescences are 4–5 cm long and 1–1.5 cm thick. They are cylindrical, reddish-brown, multi-flowered (26–50), and have a white-haired stem. Flowers on a hairy stem are up to 1 mm long. The inside of the flower is cellular, lanceolate, uneven, with sharp teeth. There are 15–31 stamens, slightly longer than the outside of the flower. The stamens are oval, up to 2 mm long, and the stamen stem is 1.5 mm long and reddish-brown.

The flower is plate-shaped, with toothed edges. Female flower buds are 10–12 mm long, oval, with a convex or flat surface, a rounded or slightly pointed tip, attached to the branch, and brownish-yellow in color. Egg-like. There are 20–35 flowers on a yellowish-green, 1 cm long hairy stalk. The inflorescence is cellular, lanceolate, with irregular teeth or smooth. The flower surface is plate-shaped, tuberous, and the stigma is yellow. The tubers are 10–11 mm long and attached to 1.5–5 mm long stalks. They are egg-shaped, with seeds 0.8–0.9 mm long and 0.1–0.5 mm thick. The length of the egg-shaped, yellow or gray, yellowish hairs is 5.5 times longer than the length of the seeds. The tree is white, the kernel is yellow, hard. The root is taproot, strongly branched. The root is soft and brown. The shell is gray. Geographic distribution floodplains of the Syr Darya, Amu Darya, Murghab, and Tedjen rivers. In Karakalpakstan, *Populus pruinosa* is found in Nurimtubek, Baday forest, Esbergen inlet, Samanbay forest, Shortanbay forest, Shagal forest and in irrigation canals between villages.

Material and Methods

Phenology of Poplar observations were conducted on a 10–15-year-old poplar tree in the botanical garden. Furthermore, observations were conducted on the poplars in the Shagal grove and around the city of Nukus. Baday, Bekboy, Nazarxon, Shoqay, Nurim, and other forests were visited (Gladysheva A. I., 1967, 22 p).

During our research period (2023–2025), the budding of the P. *pruinosa* species under study continued from the second decade of March and the first decade of April until the third decade of November. The beginning of the growing season depends on the air temperature. The earliest germination was observed in 2023, with an average air temperature of +6, 10. In the studied species P. *pruinosa*, germination occurs later than in P. *ariana*.

Results and Discussion

The autumn coloring and change in leaf color of the studied poplar species began at the end of September. Under the same soil and climatic conditions, this process begins later in P. *pruinosa* than in P. *ariana*. Defoliation begins in late October and early November. In this process, P. *ariana* begins early, while P. *pruinosa* is the last. During the research years, the defoliation period lasted 25–31 days. However, this period can change every year (table 1).

Table 1. *Phenological observation of species*

Observation date	The results of observation
March 25	Beginning of vegetation. The bud began to sprout, and the buds began to open.
April 9	The plants have started budding. A green cone of leaves appeared.
April 14	The first flowers opened, or the branches began to sprout.

Observation date	The results of observation
April 19	Complete plant. More than half of the flowers or the tips of the branches have sprouted. Flowers have bloomed (less than half of the flowers remained).
April 20	A green cone of leaves appeared. The leaves are small, just beginning to emerge from the buds on the branch. The plant has bloomed.
April 29	The branches are growing, only unripe buds are visible, the buds are green, like a hump.
May 14	The leaves have reached normal size, but they haven't fully developed yet.
May 24	The branches hardened, except for the growing tips.
May 29	The leaves have grown, but haven't reached normal size. The buds are green, small, and have scales.
June 8	A bud at the tip of the branch has appeared, but it doesn't grow. Most leaves have fully grown, and there are still young leaves at the tips of the branches. The buds are green.
June 23	The branches have reached normal size, and the scales are green.
July 3	The branch has stopped growing lengthwise, a bud has appeared at the tip, the branch has not yet hardened and is not fully covered with tissue. All the leaves have reached normal size. They will last until July 28th.
August 2	The branch has hardened and is covered with fabric. The buds reach normal size, the scales harden, and continue until September 25th.
November 30	The plant is leafless.

Flowering. The buds of P. *pruinosa* are arranged alternately on the branches, adhering to the branch, with a number of 5–13. Generative budding occurs in July on the P. *pruinosa* willow tree under study. The male flower buds of P. *pruinosa* are fully formed by July 25th, while the female flower buds are fully formed by July 25th.

Also, the size of the flower buds is 3 mm long and 2 mm wide. Flower buds emerge and develop on the branches of this year and differentiate until the beginning of the next year's vegetation. Thus, the flower buds are always biennial.

The bud consists mainly of three layers, reddish-yellow in color, measuring 12 mm in length and 4.5 mm in width. The first outer shell covers the surface of the bud. It is pinkish-white, 4 mm long and 4 mm wide, and has teeth. The inner surface is sticky, reddish-black, and contains a sticky substance. The base of the bud is hairy, the tip is split in two, and the cortex is convex. The second shell is 10 mm long and 4.4 mm wide, shiny, light yellow, red, with a greenish-white base. The third shell is 10 mm long and 3.5 mm wide, elongated, pinkish, and covered with a light yellow thin film on the outside.

Flower pollen. In 2020–23, the flower pollen length was 11 mm, cylindrical, sharp, reddish-black, with light red hairs on the outside, two petals, reddish-green, with a light-colored, hairy stem. Two types of willow buds differ from each other. The male flower structure consists of stamens, numbering 31–53 on each flower. The number of flowers in the pollen is 31–48 (Bakiyev A., Qaniyazov S. K., 2003). The female flower has only a pistil, similar in shape to thepistil of the P. *ariana* species. Under favorable weather conditions, P. *pruinosa's* flower buds begin to fully open within a week. From the very first day of blooming, it can be seen that all the flowers in the pollen are female flowers. 5–6 unevenly developed flowers appear, located at the base of the branch and larger than those at the tip. They bloom 2–3 days after the flower buds open. The earliest flowering was observed in 2023 (April 3). The air temperature here was +11.70C, and the last flowering occurred on April 19, 2024 (+14.80). Seed ripening in P. *pruinosa* is observed 105–120 days after bearing fruit.

The ripening of poplar seeds in moist soil is prolonged, and the seeds are larger, while in dry areas, the seeds ripen faster. P. *pruinosa* seeds are shown. The P. *pruinosa* poplar begins to bud in late March and early April. In 2023, P. *pruinosa* poplar began budding on March 20th at an average air temperature of 8.10, with a maximum of 23.80, and a minimum of 5.20. The mass sprouting of the poplar occurred on April 10–15. The average air temperature was 10.20, maximum – 17.80, minimum – 5.50. Data on the growth of the studied species P. pruinosa are presented in Table 6. It is evident that the growth period and branch length of P. *pruinosa* are shorter than those of P. *ariana*. The strongest growth of 10–12 year old poplars occurs in May. During this period, 50% of the annual growth of all branches is ensured. The annual growth and growth of different branches on the same tree are different. They thrive on warm days – in spring and summer. With a decrease in air temperature, the growth rate also decreases.

The proliferation of poplars. P. *pruinosa* poplar, like P. *ariana*, reproduces from seeds and vegetatively through branches and root cuttings.

Seed Reproduction of Poplar. Seed propagation of P. *pruinosa* occurs naturally and through artificial cultivation. Poplar seeds ripen in mid-August. The seeds are very small. Seeds ripen and scatter in 105––120 days. The process of seed propagation in nature coincides with the period when floods decrease and new shallows appear, where ripe seeds fall, and seedlings germinate from floating seeds Vegetative reproduction of P. *pruinosa* poplar. We studied the vegetative reproduction biology of P. *pruinosa* poplar in the natural conditions of the Shagal woodland. The object of observation was P. *ariana*. In 2024, we conducted an experiment by planting branch cuttings. For this purpose, 100 branches with a length of 35––50 cm were cut and planted along the irrigation ditches (Table 2).

Therefore, the germination rate from the branch is very low. The most common type of reproduction is propagation through root branches.

Table 2. *Data on poplar reproduction from root cuttings*

Planted Year, Date	The number of planted cuttings	Sprouted in May	Year 2024				Total of sprouted cuttings
			15th June	15th July	15th August	15th September	
3rd of March, 2024.	100	14	13	10	8	9	14%

Propagation through root branches mainly occurs in water-applied valleys. In the Baday Forest Reserve, 63 roots of the species P. *pruinosa*, ranging in length from 193 cm to 213 cm, were found on an area of 10 square metre.

Dense poplar forests grown from root branches can be found in the Amu Darya's water-applied valleys and along its banks. The root branches of P. *pruinosa* are also abundant in irrigated areas. As a result of propagation through root branches, the area of poplar forests expands.

Conclusions

In conclusion, poplars are distinguished by their resistance to salinity, low humidity, and cold. It is considered the most valuable material for green spaces in the spring months. Poplars can be propagated both by seed and vegetatively: through root buds and root cuttings.

In Karakalpakstan, due to the extensive development of land for rice and other agricultural crops, as well as the emergence of fires, the area of poplar forests has decreased. This situation occurred in the Bekboy, Shagal, and Nurim tubek forests. The forest is the wealth of the people, the golden treasure of every region. Therefore, preserving and protecting forest areas is our primary responsibility.

References

Bakiyev A., Qaniyazov S. K. (2003). Methodological Guidelines for Improving Natural Sweet Trees and Their Cultivation in the Lower Reaches of the Amu Darya. Nukus "Karakalpakstan".

Bakhiev A. B. (1974). Phytocoenotic and ecological features of the licorice formation in Karakalpakstan. Natural resources of the lower Amu Darya. Tashkent. "Fan".

Gladysheva A. I. (1967). Bio-ecological features of licorice root in connection with the introduction of its culture in the Amu Darya basin. Abstract of PhD dissertation. Ashgabat.

Korovin O. N., Bakhiyev A. B., Tadjitdinov M. T., Sarybayev B. Sh. (1982). Illustrated Determiner of Higher Plants of Karakalpakstan and Khorezm // Tashkent, FAS.

Kerbabayev B. B., Gladysheva A. B., Keljayeva P. Sh., Gekshova T. M. (1989). Licorice Culture in Turkmenistan (systematics, bioecology, introduction to culture). Ashgabat, Ilim, 192 p.

Kerbabayev B. B., Gladysheva A. I., Keljayeva P. Sh. (1986). Ways to Improve natural licorice phytocenoses and introduction of licorice into the culture. Ashgabat Turkmen. NIINTI – 39 p.

Ibragimov M. Yu., Gaipov M. Kh., Zakimov A. M. (2019). Agrotechnology of Sowing and Growing Licorice in the Territories of the Republic of Karakalpakstan. Nukus, "Karakalpakstan."

submitted 08.06.2025;
accepted for publication 22.06.2025;
published 31.07.2025

Contact: abboz-2@mail.ru

The Austrian Journal of Technical and Natural Sciences, No 5–6
ISSN 2310-5607

PREMIER Publishing
ppublishing.org

Section 2. Biotechnology

DOI:10.29013/AJT-25-5.6-8-23

RESTORATION OF CUTTING PART OF USED DOWNHOLE MILLING TOOLS

Amir Mustafayev [1], ***Rabiya Abishova*** [1], ***Sevda Aliyeva*** [1]

[1] Azerbaijan State Oil and Industry University

Cite: *Mustafayev A., Abishova R., Aliyeva S. (2025). Restoration of cutting part of used downhole milling tools. Austrian Journal of Technical and Natural Sciences 2025, No 5–6.* https://doi.org/10.29013/AJT-25-5.6-8-23

Abstract

Downhole cutting tools are used to repair oil and gas wells as well as to eliminate complicated accidents. However, their acute shortage at oilfield facilities is obvious. The conducted researches have shown that the restoration technology of downhole cutting tools are currently being introduced into production. Besides, there is no information about the layer applied to the damaged area of the cutting element, the optimal mode of operation, as well as the efficiency of the restored tool.

In the considered article, the problems which have found a scientifically grounded decision and possibility of direct introduction of the restored tool in manufacture are solved.

Keywords: *cutting tool, downhole milling machine, modeling, well, experimental unit*

Introduction

Acceleration of emergency and recovery operations in production and drilling wells at minimum costs is a significant reserve of oil and gas production growth (Müller, 2004).

The most complicated works in wells are performed with the use of downhole cutting tools. Experiments conducted during the operation of cutting tools show that, mainly, the cutting part of the tool is subjected to wear and destruction, the housing and other elements remain suitable for further operation. Restoration of working parts of, used downhole cutting tools, is a scientific and technical task in the oil and gas production industry.

At restoration of worn out or destroyed section of a working part of cutting tools are mainly applied in mine electric furnaces or HFC (high frequency current) in conditions of a manufacturing plant and by application of cutting and binding elements made in the form of special surfacing bars under the influence of a gas burner flame.

To solve the set task it is required to analyze modern methods of restoration of the worn cutting part of the used downhole cutting tools, study the efficiency of downhole cutting tools with the restored working part, to develop the technology of manufacturing of surbacing rods and technological methods

of applying them to the worn parts areas of cutting tools, as well as conduct stand tests with restored cutting tools.

The conducted analyses on the issues of restoration technology of reinforced layer of used cutting tools showed that mainly "surfacing of restoration method" is applied in Azerbaijan and abroad.

The main brands of hard alloy surfacing rods are given in Table 1.

Table 1. *Brands of Hard-alloy rods*

Solid alloy			Matrix material	
Composition, %	**Grain size, mm**	**Hardness, HRS**	**Composition,%**	**Melting point,°C**
Carbides (Mo, Cg, V, Zn, Ti, Nb) + cobalt or a mixture of carbides and cobalt	0.5–5.5	85	1) Cu; 2) Cu + Zn; 3) Cu – Ni; 4) Cu – Zn – Ni; 5) Cu – Si	871–1343
Sintered tungsten carbide	0.355–0.255 0.255–0.180 0.180–0.120 0.120–0.065	85	Copper 46... 48 Zinc 39... 41 Nickel 10...12 Silicon 0.15 Phosphorus 0.02	873–1312
Sintered tungsten carbide + co-balt 4–12% + + nickel 5 + 35%	0.5–5.5	85	Copper-nickel-iron; Copper-nickel-tin; Copper-nickel-iron-tin; Copper-nickel-manganese	843–1317

Bars are mainly made of refractory carbides such as cobalt, tungsten, niobium, titanium, as well as matrix material based on alloys of copper with zinc, tin, nickel, iron, manganese.

For the manufacture of carbide bars, masses of crushed solid particles in the required sizes are first selected, then they are chemically treated to purify them from foreign material (Table 1). Solid particles together with pieces of solder along the specified length are placed in special molds and put into thermostatic furnaces. Under the influence of heat, the solder melts, coating the carbide particles. After cooling it forms a composite carbide rod of a given diameter and length.

Carbide surfacing rods used for restoration of working parts of downhole milling tools, are produced abroad. Mainly these rods are produced by the German company "Woka" (Müller, 2004). It produces industrial brand of surfacing rods "DURIT" (Table 2). The size of tungsten carbide particles ranges from 1 to 12 mm. Six fractions of tungsten carbide particles are used for manufacturing of rods: 1.0–2.0 mm; 1.5–3.5 mm; 3.5––5.0 mm; 5.0–6.5 mm; 6.5–8.5 mm; 8.0––12.0 mm. Rod dimensions – 9.5 × 450 mm.

These rods provide good adhesion of the surfacing with the base of the cutting tool, and also provides reliable protection of wear surfaces of drilling equipment parts.

Data on sintered fluxes of different granulometric composition produced by "Woka" for autogenous and electric surfacing are given in Table 3.

Table 2. *Surfacing with Woka rods*

No.	Type designation	Analysis results	Type of product property
DURITS 1	Carbide W_2C	Carbon:3.7–4.1% Other: 0.75% max. Residue: tungsten	Fine feather structure of maximum hardness

No.	Type designation	Analysis results	Type of product property
DURITS 1	Sintered carbide	Carbon: 6% Cobalt: 6% Titanium: 1% max. Other: 0.75% max. Residue: tungsten	For the manufacture of composite type rods and other welding filler materials
DURITS 4	Sintered carbide	Carbon: 6% Cobalt: 6% Titanium: 4% max. Other: 0.75% max. Residue: tungsten	For the manufacture of files and other types of tools, as well as for the manufacture of compozit type rods
DURITS 10	Sintered beads	Carbon: 5.75% Cobalt: 6% Residue: tungsten	For the manufacture of roller cone bits and tools for deep oil drilling technology

Table 3. *Autogenous and electric surfacing for different smooth-metal compositions*

No.	Established analysis	Rockwell hardness	Application area
DURITS 70	70% WC 10% C_2 Residue Fe	70	High-strength and wear-resistant metals against shockless surfacing loads
DURITS 70	80% WC 20% Fe	65	In parts subjected to abrasion and abrasive wear under low impact loads
DURITS 80 Ni	80% WC 10% Ni 10% Fe	60	In chip cutters, pressure rollers, impact bars

The American company “International Tool Co.”, depending on the purpose of cutting tools, produces industrial brand of rods of various alloys ‘Zitco’, which is made of tungsten carbide, for hard-alloy coating on cutting areas of tools; cutting steel alloys “Zitco-1”; for working in soft and medium hardness rocks “Zitco-2”, and in hard rocks “Zitco-3”.

The American firm “Bowen” produces an industrial brand of “Itcoloy”, which is used to cover the working surface of cutting tools, shoes, stabilizers, etc. (Bowen Tools Inc. 1972).

Itcoloy rod contains 80% of crushed tungsten carbides with hardness of 91–93 Rockwell units.

The binding material (matrix) is silver alloy with shear strength of 70 kg/mm^2 and hardness of 200 Brinell units.

In Azerbaijan and neighboring countries produce carbide materials consisting of tungsten carbides such as WC2, WC3. These materials have high wear resistance and chip formation. Composition and mechanical properties of hard alloy grades are given in Table 4.

Table 4. *Composition and mechanical properties of hard alloy grades*

Alloy grade	Approximate alloy composition, %		Hardness, HRS	Average bending strength, MPa
WC 2	98	2	90	1100
WC 6	94	6	88.5	1450
WC 8	92	8	87.5	1500
WC 10	90	10	87.0	1600
WC 15	85	15	86.0	1800

Model samples of downhole milling cutters, cutting edges consisting of composite materials containing crushed particles of tungsten-carbide alloys were manufactured for experimental studies and evaluation of wear resistance and metal chip formation. The conducted researches have shown that the best results are achieved in the case of application as cutting elements of grains of crushed tungsten-carbide alloy of WC8 grade and matrix bonding solder No. 4 or No. 7. These alloys have high wear resistance, the optimal ratio of carbide and solder is 60–65% carbide and 35–40% solder (Gasanov, 1978; Mustafaev et al., 2023; Mustafayev et al., 1997; Mustafaev et al., 2021).

Experimental studies have been carried out to investigate the effectiveness of the restored reinforcement layer of used downhole cutting tools. From the point of view of minimizing time and material costs, it was first decided to conduct experimental studies on model samples of cutting tools.

The method of physical modeling is the most acceptable method of research of the cutting process with the restored layer of the reinforced part is (Bondar, 1973).

The difference between the restored part of the reinforced layer of the cutter and the new one is specific.

Figure 1. *Model of restored milling cutter*

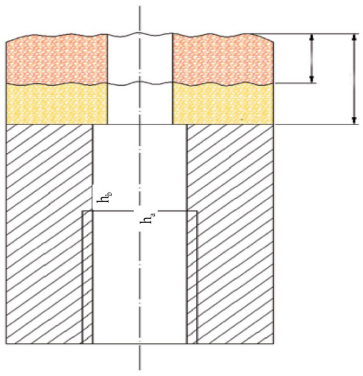

Taking into account the identical condition of the milling process of new and restored tools, we can use the known scaling factors.

Then we have the following relations to the restored borehole metal milling cutters:

$$C_Q = C_\Gamma^{\frac{-1}{2}};\ C_N = C_\Gamma^{\frac{-1}{2}};\ C_E = 1;\ C_\omega = C_\Gamma^{\frac{1}{3}};\ C_\sigma = 1;$$

$$C_D = C_\Gamma^{\frac{-1}{3}};\ C_\rho = C_\Gamma^{-1};\ C_\lambda = C_\Gamma^{\frac{-1}{2}};\ C_a = C_\Gamma^{-1};\ C_\rho = C_\Gamma^{\frac{-1}{3}};$$

$$C_t = 1;\ C_{\Delta u} = C_\Gamma^{\frac{-1}{6}};\ C_d = C_\Gamma^{\frac{-1}{6}};\ C_c = C_\Gamma^{\frac{-1}{3}};\ C_\rho = C_\Gamma^{\frac{-1}{3}};$$

$$C_a = 1;\ C_u = C_\Gamma^{\frac{-1}{6}};\ C_{y1,2} = C_\Gamma^{\frac{-1}{3}};\ Ch_b / h_a = C_\Gamma^{\frac{-1}{6}} \quad (1)$$

These scaling factors make it possible to transfer the results of experiments on models to full-scale samples with sufficient reliability. On the basis of scaling factors the designs of model samples of cutter and milled object were developed.

The previously developed models of cutting milling cutters with a restored cutting edge height h_b and total reinforcement height h_a were used as models (Figure 1).

Tests of model samples were carried out on the experimental installation (Figure 2).

This installation makes it possible to regulate the supply of flushing coolant, air and to measure the temperature with sufficient accuracy. The installation is equipped with measuring instruments, mounting and dismounting of the investigated sample does not cause difficulties.

The model of the restored cutter is a metal cylinder made of steel 45 with an outer diameter of 31 mm and an inner diameter of 13 mm. The lower end of the cylinder consists of a worn layer of carbide composite material of different height h_a, on which a new layer of height h_b is clad (Figure 1).

The experimental installation consists of the following units: a special machine 2H-135 (table size 450 × 500 M), a model sample of a milling machine (2), cooling devices (4), an object to be milled (3), a gas ejector (EG 750) (5).

The body of the model sample of the milling tool is made of 40X steel with an outer diameter of 34 mm and an inner diameter of 14 mm, its cutting part is made of carbide composite material BK8. Composite materials consisting of crushed carbide and binder, applied to the body of the model sample has the highest indicators of cutting ability and wear resistance. The process of milling of the emergency metal object by such milling cutters is self-sharpening, as new cutting elements come out of contact with the surface of the milled object as the cutting edge volumetrically wears out. The conditions of manufacturing of the model sample corresponded to the conditions of manufacturing

of serial downhole milling cutters of WBM (wellbottom miller) type, reinforcement of the cutting part was made by HFC (high-frequency current) in AzINMAS H.

One of the requirements for cutting tools is to create the largest metal cut, which depends on the strength condition of the cutting element.

The cutting part is reinforced at a height of 10 mm. In the reinforced part there are horizontal stainless steel shutters with a diameter of 2 mm for chromel-alumel thermocouples (CAT), and vertically with a diameter of 3 mm for liquid supply. After reinforcement, the shutters were fully perforated. Then the thermocouples (semi-artificial thermocouples, calibrated to the accuracy of 10 °C) were installed on the body of the cutter and insulated with liquid resin. At high temperatures, this resin does not melt, but rather hardens and gives a good guarantee of heat transfer from the measuring point to the measuring instrument. Minor heat transfer to the medium is not considered.

Figure 2. *Experimental installation*

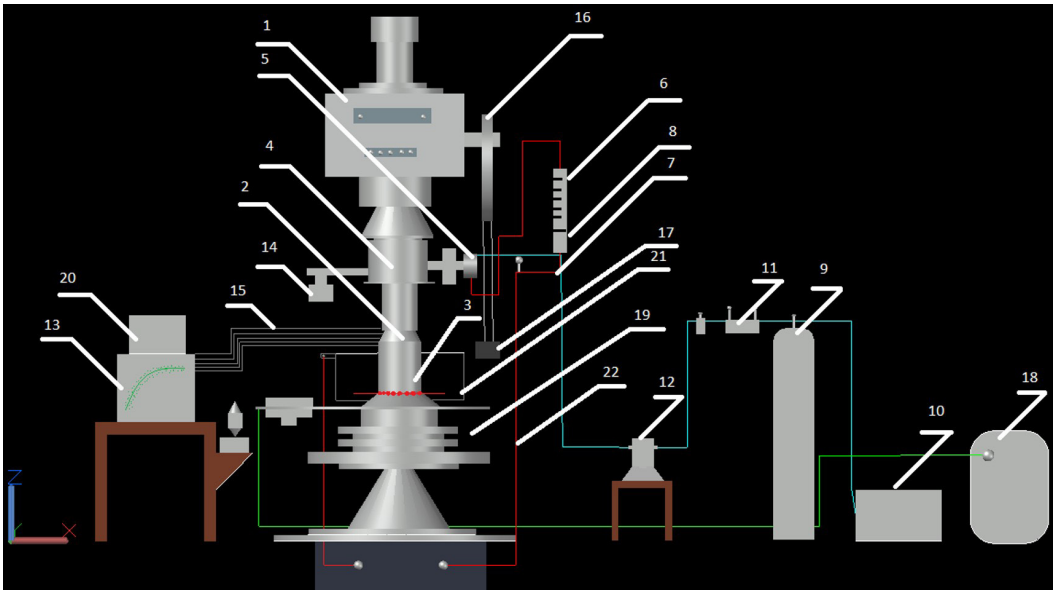

The experimental work spent on chip removal depends mainly on the physical and mechanical properties of the machined material. With the increase of mechanical properties of machined materials, the stress and deformation state of the chip formation zone increases, at the same time the force and energy indicators of the process increase. The stressed and deformed state in the zone of chip formation depends on the resistance of the machined material to plastic deformation. The higher the toughness and riveting ability, the greater the resistance of materials to cutting.

Increase of stressed and deformed state and temperature in the zone of chip formation, the manifestation of hardening in this zone, as well as the ability of materials to tilt leads to an increase in cutting forces, which in turn can contribute to blunted model tool specimen and tear out their cutting elements. Proceeding from this, milled samples are made of steels 20X, 40X, 30, 35, 45 – the mechanical properties of which are close to the mechanical properties of tubing. The samples have a cylindrical shape with an outer diameter of 34 mm and an inner diameter of 14 mm. Model samples are inserted into a special disk mandrel, changing the parameters of the milling mode, thus changing the samples in the mandrel.

The tool and the material to be processed are cooled by three components: 20 °C process water, air and their mixture. First, we regulate the amount of FC with the rotometer (6). Water is supplied to the cutting zone by the rotometer, which has a tee valve at the outlet. One end is connected to the manometer, and the other end is connected to the rotometer with a rubber tube. (For example: the valve is set to the manometer reading P = 0.15 atm corresponds to *Ql = 40 ml/sec.* The other indicators are given in Table 3).

Figure 3. *Combinaton cube of experiment planning*

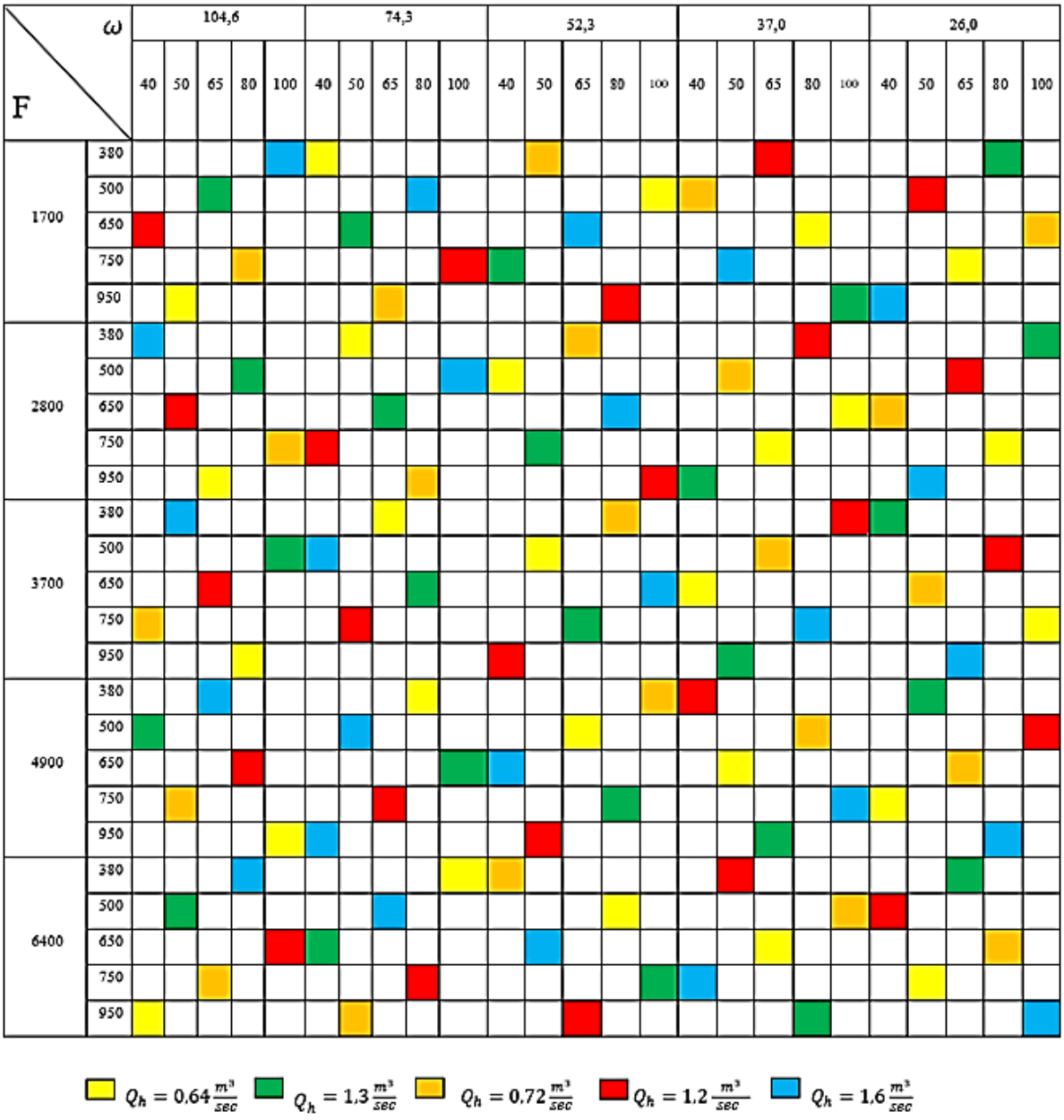

In the first stage, the experiment was conducted without cooling. In the second stage of the experiment, the air supply is regulated. First, a gas cylinder (9) is filled bu a compressor (10), a reducer (11) is installed at the outlet of the cylinder, which regulates the air supply. Then the air is transferred by a rubber hose to the gas meter (CT-40) (12), where its readings are taken (Table 3), then to the gas ejector and the milling zones. When it is necessary to supply one or another component to the cutting zone, one side of the gas ejector (EG 750) is plugged. GE is designed for mixture of liquid with air.

High-pressure air and low-pressure water are fed into the EG (Fiqure 3), a mixture of air and water is formed in the displacement chamber and the air sharply increases the flow velocity. Having a significant speed, the air jet creates a zone of low pressure around itself, in which low-pressure water from the receiving chamber to the milling zone is tucked. The result is an aerated liquid. The EG is attached to the body of the cooling unit (CU).

The CU is a special designed device designed for tool cooling. The upper part of the device stem is prepared for Morse taper and seated on the spindle socket with a tension that prevents it from falling down when the

CU is rotated. In the middle of the CU 4 holes in the form of a blade are drilled to ensure the supply of aerated liquid at high speeds. Due to the movement of the flow through these holes there is a centrifugal force, creating a vortex motion, which moves the liquid and there is a diffusion effect. Aerated liquid enters the CU through the hole available on its body. Along the outer diameter of the stem below the body 6 grooves of 1 mm wide are cut (Figure 3). A copper ring insulated with epoxy resin is installed in each groove. The lower part of the stem is threaded and connected to the router model. Each ring is then connected by soldering the corresponding thermocouples of the cutting model. As the milled sample is processed, the milling plane approaches the junction of the thermocouple and the fixed temperature in the body of the cutter in the form of an electrical signal is transmitted through the current puller (14), to the self-recording device (SRD-9) (13), where the measurement results are recorded on chart paper. The current collector is connected to the self-recording device by compiling wires (15) and fixed on the body of the cooling device, where the body is stationary at the moment of rotation. The slip ringshabts are in sliding contact with copper rings mounted on the outer diameter of the rod when rotating the tool model.

Operation of the cutting model depends on the power of the power equipment combination with the axial load on the tool to realize sufficient metal removal. To ensure the required axial force delivery on the drilling machine, the handle is replaced by a pulley (16). A steel rope is wound on the pulley (pulley diameter Ø 400 mm) and a tripod is attached to its end. When changing the milling parameters, appropriate scales (17) are mounted on the tripod. The axial force is pre-torqued with a dynamometer for each 1000 N. The dynamometer is also calibrated with an accuracy of 5 kg.

When adjusting the axial force, the power of the experimental machine tool is taken into account. When measuring, the generated power (N_1) must not exceed the power of the machine tool (N = PV), i.e. $N_1 \le N = 4200$ N m/sec. For example, at speed n = 31.5 rpm mechanical speed V = ωr_1 = 0.056 m/sec; where ω = = 3.3 rad/sec is angular velocity; r_1 = 0.017m radius of router model) axial force will be 71430 N. So the axial force created in this revolution should not exceed 71430 N. The generated power is measured with a wattmeter (H350) (20).

In some cases, the stand does not allow the experiment to be performed by rotating the sample. During such rotation the cutter is stationary. The rotation of the borehole is performed by means of an electric motor (belt transmission) with 25000 N m/sec. Pulleys of different diameters allow to change the rotational speed of the borehole. The inner diameter of the rotating borehole is cone-shaped. Therefore, the lower part of the milled material is prepared in the form of a cone and is injected into the borehole to increase the strength, safety and manufacturability of the milling process. Supply of cooling agent to the cutting zone is provided from transparent pipes by a closed circular circuit (22). The beaker (21), in which the material to be processed is placed, is also made of transparent pipes, so that the processes taking place in the milling zone during the experiment can be seen.

Each sample of the restored cutter was first subjected to a test run to ensure that the existing solder layers and other irregularities on the cutting surface were fully worked in. Completion of running-in was determined by stabilizing the wear of the cutter, which was determined visually.

Depending on the quality of restoration of the cutting part of the cutter and the mode of operation, the burn-in was continued for 5–20 min. Experimental studies consisted of separate series, each of which included several experiments to ensure the accuracy of the obtained results.

The number of necessary experiments was determined by the general dispersion of observations and the acceptable dispersion of research results found out from preliminary studies. Experimental work was carried out to investigate the wear resistance of restored tools.

At different series of experiments the following main parameters of the investigated process were regulated: static axial load on the cutting mill – P; angular velocity – ω; flow rate of FC – Q; height of the restored layer – h_b.

Table 5. *Experimental parameters*

No.	Axial load of the milling cutter, N	Angular speed of the cutter, rad/s;	Consumption FC, м³/s	Relative height of the restored layer, %	Milled metal
1	1.7	26	40	32	ST 40X
2	2.8	37	50	36	
3	3.7	52.3	65	50	
4	4.9	74.3	80	61	
5	6.4	104.6	100	68	

To evaluate the milling cutting performance, samples before and after the experiment were weighed on technical scales.

Based on the obtained data and visual observations, the results of the conducted experimental studies were summarized and processed.

The efficiency of work, restored cutting parts of milling cutters, depends on the correct choice of mode parameters and on the height of the restored layer of used milling cutters reinforcement.

The equation reflecting the physical essence of the process is related to the main parameters of the cutting process:

$$q_s = f\left(P, w, Q, h_a / h_b\right) \qquad (2)$$

where: $q_s = \frac{q_{c.m.}}{q_c}$ – specific productivity of milling cutting, gr/gr; $q_{c.m.}$ – wear rate of milled metal, g/min.; q_c – wear rate of model sample of cutting element, g/min.; P – axial load on the cutting element, *kN*; ω – angular velocity of the tool, *rad/s*; Q – pump capacity, m^3/s; h_b – height of the restored reinforcement layer, mm.

To determine the optimal parameters of the restored optimal height of the reinforcement layer, it is required to determine the qualitative and quantitative influence of various factors on the indicators of the milling process. As it isindicated above, when the elements of the cutting part of the tool are restored, their parameters change significantly. This fact requires to investigate the process of milling with restored samples, to study the relationship between the parameters and the degree of their influence on the process, to find a mathematical model.

Investigation of the efficiency of the restored elements of downhole milling tools on the basis of field data is difficult and requires considerable expenses. Methods based on dispersion, regression and correlation analysis can be used to solve this problem experimentally.

To solve the task at hand, it is advisable to use the method of rational planning of the experiment, because with a minimum number of experiments it is possible to obtain more accurate results. To achieve this goal, each experiment should differ from the others by a non-repeating combination of selected factors.

Combination squares, numerical matrices or orthogonal squares can be used in rational planning. Since four factors change in the process of milling with reclaimed tool cutting, the method of combinational square was applied in our study (Figure 3).

The combination cube was made in such a way that there were no repeated combinations in any row or column. Based on the combinational square, the need for 25 experiments was determined. The calculated variants and the obtained results of experiments are shown in Table 2.

By means of correlation and regression analysis the qualitative and quantitative influence of the selected factors on the process indicators was determined.

Variables (output parameter) and factors are random variables and there can be a correlation relationship between them, which is characterized by the correlation coefficient, and allows to assess the measure of statistical relationship between the indicators and process parameters, as well as between the regulated factors themselves.

The results of correlation analysis were the initial material for the construction of regression equations.

The experimental data were processed using correlation and regression analysis, and

a statistical mathematical model of the process was obtained in the form of a regression equation. The results of the conducted experiment of the complete study were processed according to the optimal algorithm, in order to create a mathematical model of the process (Mustafaev et al., 2022; Dzhafarov, 2021).

This sequence was applied in the derivation of the regression equation of the active experiment to determine the effect on specific wear of the parameters included in the physical equation (Table 2) (2).

Using the results of active experiment, the following equations describing the metal milling process were obtained (Table 6):

– for specific productivity:

$$Y_{s.} = 142.41 - 0.93X_1 - 1.17X_2 + \\ + 2.2X_3 - 0.22X_4 \quad (3)$$

– for the wear rate of the milled material:

$$Y_{s.} = 7.51 - 0.025X_1 + 0.032X_2 - \\ - 0.0163X_3 - 0.003X_4 \quad (4)$$

– for the wear rate of the cutting tool:

$$Y_{c.t.} = 0.065 + 0.0001X_1 + 0.0006X_2 - \\ - 0.0010X_3 + 0.00006X_4 \quad (5)$$

where Y – random variables; $X_1, X_2 ... X_n$ – factors of varying small error.

The degree of correspondence between the experimental data and the values of specific productivity, wear of the processed material and cutting tool calculated by equations (3–5) determines the measure of identity determined by the formula:

$$\theta_y = \sum_{i=1}^{N} a_i r_y X_i \quad (6)$$

$$a_i = a_i \frac{\sigma_{xi}}{\sigma_y}$$

where a_i – the coefficient of the regression equation. For our case $\theta_s = 0.992$

The multiple correlation coefficient on the magnitude of the identity measure, which characterizes the degree of closeness of the experimental data to the linear model, was calculated from the relationship:

$$R_s = \sqrt{\theta_s} = 0.998 \quad (7)$$

Table 6. *Results of the conducted experiments*

Factors				Output factors		
ω, rad/s	**P, $10^2 N$**	**h_b/h_a %**	**Q, l/ sec**	**Cutter wear rate Y_c, g/min**	**Wear rate of the cutter material $Y_{c.м.}$, g/min**	**specific productivity $Y_{s.}$, g/g**
26	6.4	65	65	0.05	8.57	141.28
37	6.4	20	50	0.11	7.67	58.03
52.3	6.4	77	100	0.04	7.58	125.58
74.3	6.4	45	40	0.07	6.68	82.01
104.6	6.4	55	80	0.08	6.71	73.06
26	4.9	20	80	0.02	8.48	77.68
37	4.9	77	65	0.04	7.63	155.23
52.3	4.9	45	50	0.05	9.13	101.01
74.3	4.9	55	100	0.06	7.58	99.32
104.6	4.9	65	40	0.05	8.32	123.01
26	3.7	77	40	0.02	6.53	205.03
37	3.7	45	80	0.03	7.01	137.22
52.3	3.7	55	65	0.04	6.75	126.45
74.3	3.7	65	50	0.02	3.12	147.61
104.6	3.7	20	100	0.01	5.32	48.02

Factors				Output factors		
ω, rad/s	P, $10^2 N$	h_b/h_a %	Q, l/sec	Cutter wear rate Y_c, g/min	Wear rate of the cutter material $Y_{c.м.}$, g/min	specific productivity $Y_{s.}$, g/g
26	2.8	45	100	0.033	6.57	148.34
37	2.8	55	40	0.034	7.63	168.13
52.3	2.8	65	80	0.018	6.01	165.43
74.3	2.8	20	65	0.068	7.14	87.68
104.6	2.8	77	50	0.028	5.58	168.32
26	1.7	55	50	0.026	6.28	196.77
37	1.7	65	100	0.023	5.47	194.23
52.3	1.7	20	40	0.051	7.26	115.67
74.3	1.7	77	80	0.016	5.28	188.24
104.6	1.7	45	65	0.03	5.15	126.11

Figure 4. *Dependencies of values: a) $Y_{c.t}$. b) $Y_{c.t.}$ and c) Y_s pump capacity*

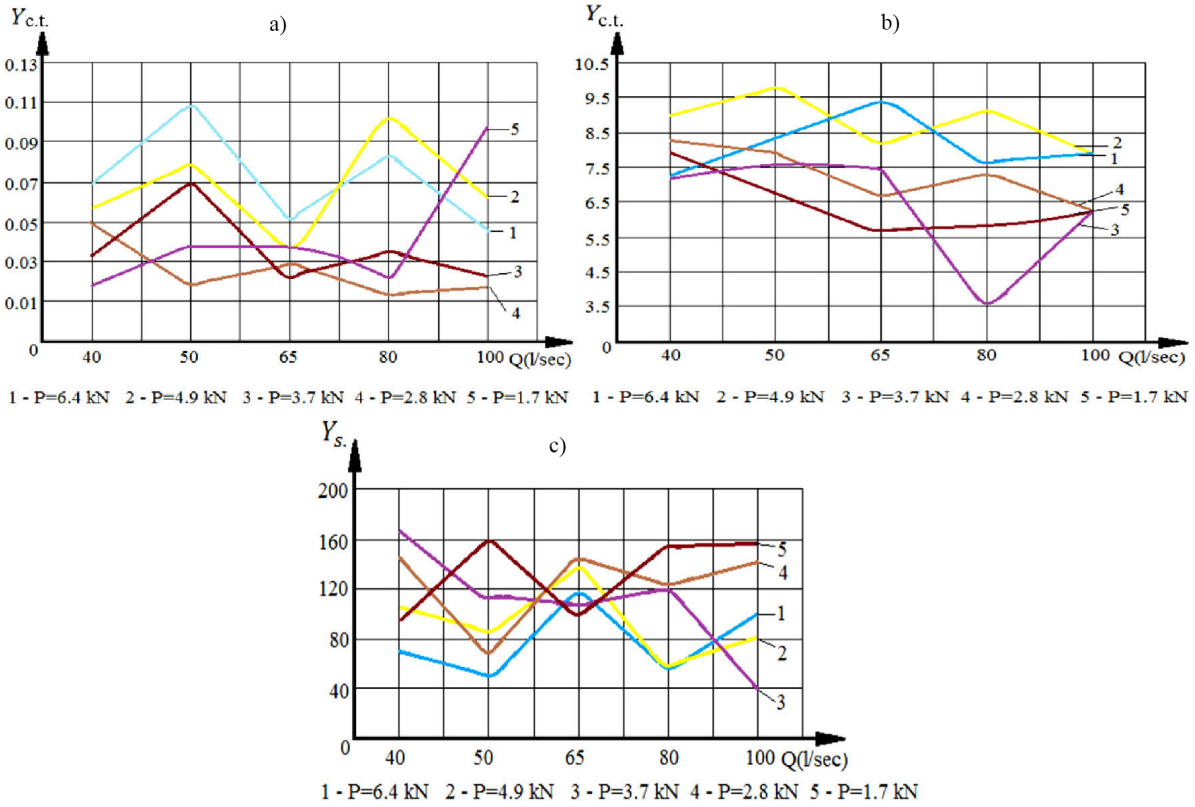

Determination of the adequacy of the obtained equation (the degree of its reproducibility) was checked using Fisher's criterion.

The obtained dependencies by Fisher's criterion showed that the selected mathematical models adequately describe the process of milling of emergency metals by the restored cutting edge.

In our case with respect to the equations: (4) – $F_p = 6.15$; (5) – $F_p = 1.742$; (6) – $F_p = 5.33$

For the degree of freedom $f_1 = N - 1 = 24$ and $f_1 = N - (K+1) = 20$ at the chosen level of significance $q = 0.005 - F_{table}$ (Mirzajanzadeh A. H., Stepanova G. F., 1977), since the condition $F_p \le F_{table}$ equations (4–6) adequately describe the milling process.

Figure 5. *Dependencies of magnitudes: a) $Y_{c.t.;}$ b) $Y_{c.t.}$ and c) $Y_{s.}$ of the angular speed of the cutting tool*

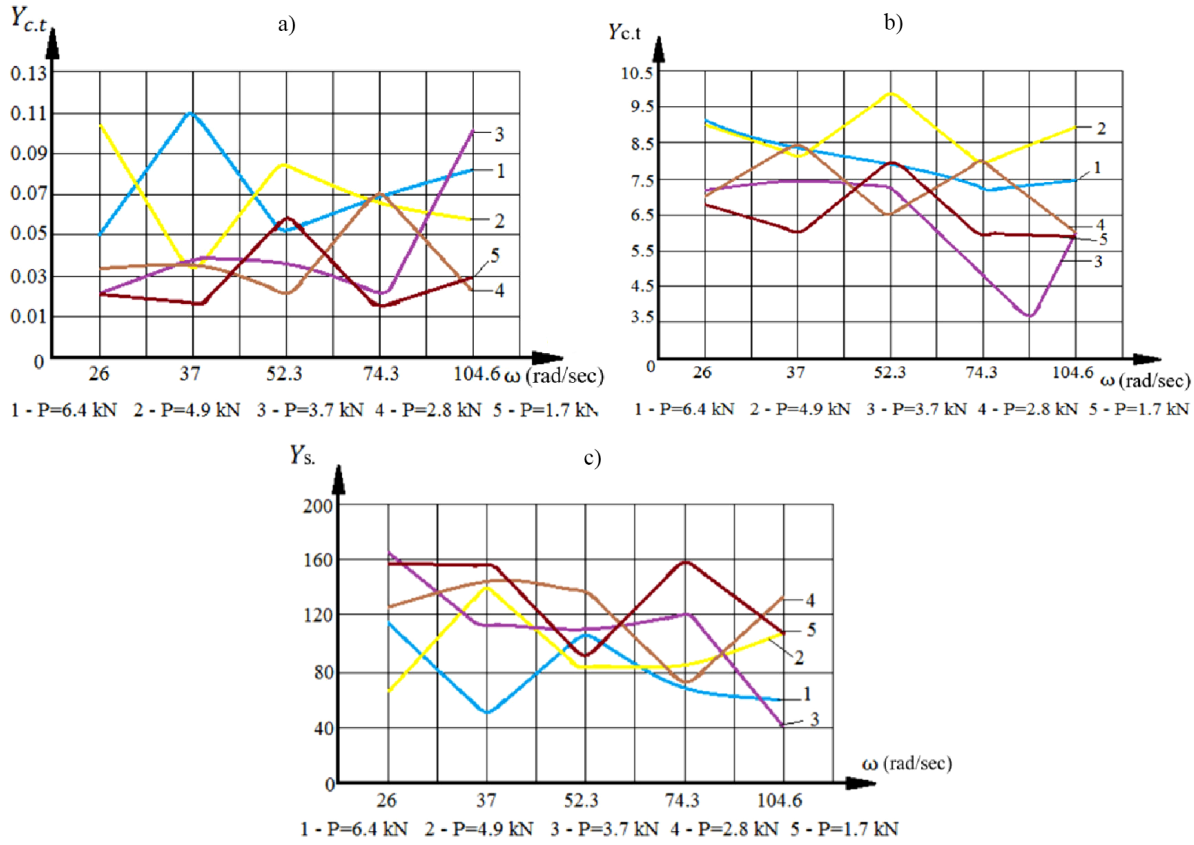

The obtained regression equations (4), (5) and (6) were used to select rational combinations of mode parameters and height of the restored reinforcement layer in order to obtain maximum process productivity within the tool life. According to the obtained data, the graphical dependences of $Y_{c.t.}$, $Y_{c.t.}$ and Y_s. values were plotted separately from each of the mode factors when averaging and neutralizing the influence of other factors (Figure 4). The graph shows that h_b/h_a change has a negative sign influence on Y_s. With the increase of the height of the reduced layer and its connection with the residue of the main layer thermal factors do not act. A proportional increase in the height of the reconstructed layer weakens the influence of these factors on the joint, thereby reducing the wear of the cutting edge.

One of the main requirements for cutting tools is the greatest penetration through the emergency facility with the least amount of cutting edge wear. The highest efficiency of metal cutting is achieved at the highest specific productivity. To establish this it is necessary to compare the dependencies $Y_{c.t.} = f(h_b/h_a)$ and $Y_{c.t.} = f(h_b/h_a)$.

At a sharp decrease of $Y_{c.t.}$ with the increase of the restored layer, $Y_{c.t.}$ slightly decreases (Figure 4 and Figure 5), and Y_s. increases (Figure 6). The obtained dependencies can predict that as the recovered layer increases, the productivity of the recovered tool increases. However, it is technologically impossible to increase the reduced layer indefinitely. Considering that after the ratio h_b/h_a=70...80%, q_s – specific productivity (q_s) increases insignificantly, so we consider it optimal.

The analysis of the curves shows that compared to new tools, the restored tools must be operated with a comparatively lower axial load, a higher angular velocity and the same applied FC (flushing coolant) flow rate.

Figure 6. *Dependencies of magnitudes: a) $Y_{c.t.;}$ b) $Y_{c.t}$ and c) $Y_{s.}$ on the ratio restored to the main reinforcement layer*

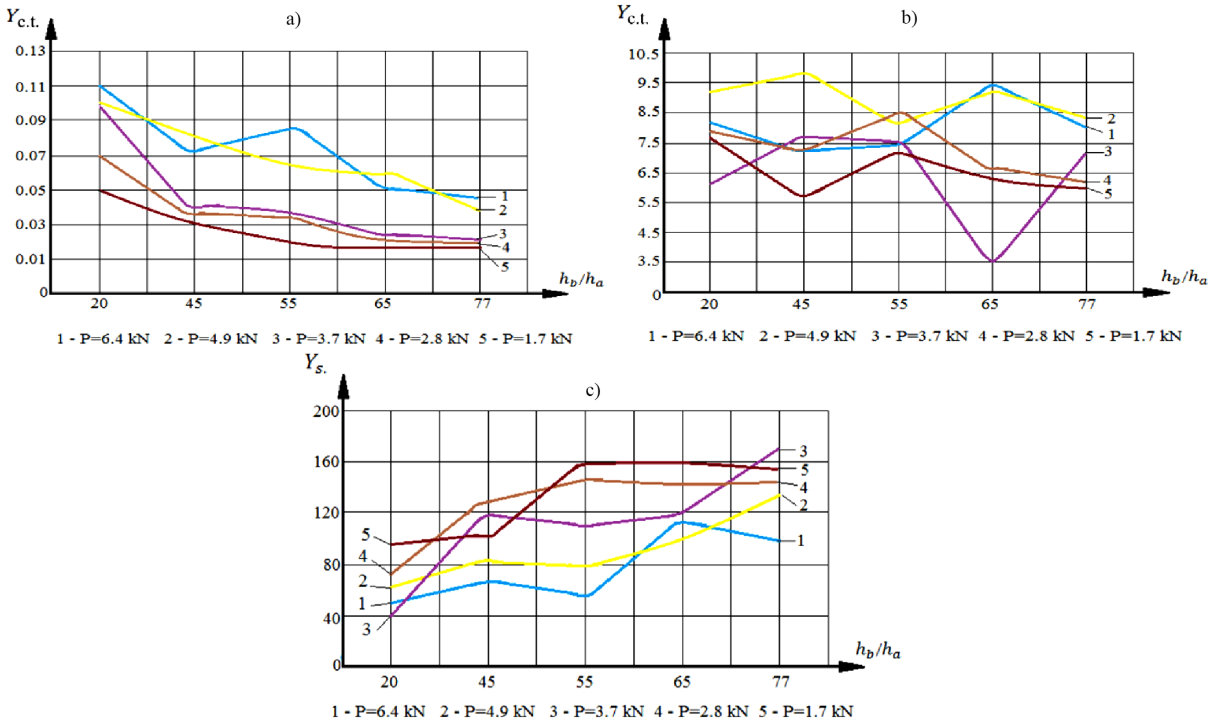

The process of milling of emergency objects during workover in the wellbore, as well as destruction of rocks during drilling occurs in identical conditions.

Based on the data of drilling operations, we make a ranking of the values of penetration – 6, 19, 20, 21 and check whether the minimum or maximum variants per defect.

To exclude defective data, we check the maximum and minimum values of each statistical combination by observing the inequality:

– to exclude the maximum variant:

$$\frac{C_n - C_{n-1}}{C_n - C_1} \geq K_n \qquad (8)$$

– to eliminate the minimum variant:

$$\frac{C_2 - C_1}{C_n - C_1} \geq K_n \qquad (9)$$

where, C is the value of penetration. Based on the number of variants in this set (Mirzajanzadeh et al., 1977), the value of *Kn* – we choose from the table at a given value of confidence probability (Typical methodology of industrial tests, 1975).

In our case:

— minimum variant:

$$\frac{C_n - C_{n-1}}{C_n - C_1} = \frac{-19-6}{21-6} = 0{,}86 \text{ for } n = 6$$

$$K_n = 0{,}560 < 0{,}86$$

— maximum variant:

$$\frac{C_2 - C_1}{C_n - 1} = \frac{21-20}{21-6} = 0{,}06 \text{ for } n = 6$$

$$K_n = 0{,}560 > 0{,}06$$

Since in inequality (8) the minimum variant is defective, therefore its value of penetration (6 m) is excluded.

At the same time, the maximum value of penetration in inequality (8) is observed and it is not defective. Therefore we make a new row – 19, 20, 21.

We check the defectiveness of the minimum and maximum variants by the new row:

— minimum variant:

$$\frac{C_n - C_{n-1}}{C_n - C_1} = \frac{20-19}{21-19} = 0{,}5 \text{ for } n = 5$$

$$K_n = 0{,}642 > 0{,}5$$

— maximum variant:

$$\frac{C_2 - C_1}{C_n - C_1} = \frac{21-20}{21-10} = 0{,}5 \text{ for } n = 5$$

$$K_n = 0{,}642 > 0{,}5$$

If inequalities (8) and (9) are not met in both cases, then the tested variants are not excluded (the aggregate is preserved).

Average penetration per cutting tool: 100/5 = 20 m

We determine the standard deviation of the value by formula (8):

$$S' = \frac{C'_n - C'_1}{dn'} = \frac{Vn'}{dn'} \qquad (10)$$

where: Vn′ – different variation of the value in the newly obtained variation series; dn′ – a value determined according to (Typical methodology of industrial tests, 1975) depending on the number of members in the considered combination.

Then, with respect to our condition:

$$S' = \frac{C'_n - C'_1}{dn'} = \frac{21-19}{2{,}326} = 0{,}86$$

The sample coefficient of variation is determined by the formula:

$$Kb = \frac{S'}{n} = \frac{0{,}86}{20} = 0{,}043 \qquad (11)$$

The maximum permissible relative error during testing is set (in fractions of one unit): $\delta' = 0{,}3$ and $\delta'' = 0{,}2$.

The value is calculated at a confidence level of 0.95:

$$\frac{ta'}{\sqrt{n}} = \frac{\delta}{K_b} \qquad (12)$$

The value determines the minimum required number of prototypes of the compared designs for specific characteristic conditions, providing the necessary reliability and accuracy of the obtained experimental data (Typical methodology of industrial tests, 1975).

For reconstructed cutting parts of the tool:

$\frac{ta'}{\sqrt{n}} = 6{,}97$, $n_{\min} \prec\prec 5$ for cutting tools.

$\frac{ta'}{\sqrt{n}} = 4{,}65$, $n_{\min} \prec\prec 5$ for the new cutting tools.

Based on this calculation, the minimum required number of milling tools was determined, which is equal to 5 pieces. This number allows to obtain reliable results during testing.

For stand tests, 5 milling tools of DC-135 type were selected as milling tools. The cutting and abrasion areas of these milling tools were restored by means of a gas burner flame and carbide surfacing rods manufactured according to a special technology.

The following operating parameters were adopted during the tests: axial load on the cutter, 37 *kN*; angular speed of the cutter rotation, ω=52,3 r/sec; flow rate of the oil-water treatment fluid – 40–100 *l/sec*.

The analysis of the performed work on the restored downhole milling machines showed that the total wear of reinforcement made in the new and restored versions of milling machines at consecutive work on the tubing Ø73 mm and Ø89 mm for both versions of milling machines is approximately the same.

Evaluation of performance and reliability indicators of the restored downhole milling cutters according to the results of stand tests showed the following: specific penetration of the restored milling cutters on the tubing Ø73 mm and Ø89 mm will be 0.51 m/mm. The resource of the restored reinforcement layer at the maximum surfacing height of 10 mm will be: in terms of penetration 4.9 m; in terms of working time 12 hours.

Taking into account the result of the restoration of worn areas, the total height of the reinforced layer of milling cutters is about 11–19 mm. The resource of the reinforced layer of the restored cutter is about 65% of the resource of the total height of the new cutter.

Visual inspection of the restored milling cutters after tests showed that they can be reused for stand tests.

Thus, stand tests of the restored downhole milling cutters confirmed that restoration of the abrasion-cutting part of the used milling cutters is acceptable for the technological process, milling providing an increase in the service life of the milling tool without significant material costs.

Examination of the used milling cutter of DC-135 type restored showed that it can be reused in other wells. The wear of the reinforcement amounted to 2.5 mm.

The results of experimental tests of the restored DC-135 type milling machine showed its operability and reliability in milling various metal objects.

On the basis of positive results of stand and tests of restored downhole cutting tools the following instruction was developed.

According to the instruction the sequence of technological methods for restoration of abrasion-cutting section of used downhole milling tools, reinforced with crushed hard alloys, as well as the order of their quality control is determined. The essence of restoration of the abrasion-cutting section of milling tools reinforced with a hard alloy consists in surfacing the worn-out sections of the reinforcement with crushed hard alloy grains appluing carbide rods with the use of a gas burner operating on an oxygen-acetylene flame. Carbide bars are produced on sheets of carbide bars using a gas torch operating on an oxy-acetylene flame. Carbide bars are produced on slabs. They are used in molds made of graphite material in the presence of an electric furnace, providing the creation of a thermal field with a temperature of 1050 ºC.

The starting materials (charge) for the production of bars are:

— crushed hard alloy of grade BK8 and particle size 0.5–5 mm; solder of grade no. 4 or no. 7 TU 48–21–299–78; flux of grade PV 209X GOST 23170–78.

The material of the bar should contain in percent of the total mass (calculated amount): carbide 65–70; solder 30–35.

Crushing of carbide is performed by any method providing grain size (0.4–5 mm). Selection of carbide grains was performed by means of sieves.

Manufacturing of carbide bars consists in preparation of initial materials, their pouring into graphite molds, heating to melting and subsequent cooling in the molds in the air, removal of bars and checking the quality of their manufacture.

When preparing the crushed alloy, it is necessary to degrease the selected crushed carbide with gasoline or other solvent, and then mix with flux at the rate of 5 grams of flux per 250 grams of carbide.

To prepare the solder, cut the solder into pieces having a maximum side size of 5–1 mm in cross-section. Weigh the prepared crushed carbide and solder. Place them in the graphite mold along its entire length. The initial amount of carbide should be equal to its calculated amount, and solder 10–15% more than its calculated amount, depending on the degree of burnout.

The prepared charge should be covered with flux at the rate of 1–1.5 grams per 100 grams of charge. To produce bars, place the prepared mold with the charge in a thermal field and heat it to a temperature of 1050 ºC. After holding for 2–5 minutes at the specified temperature until the solder is completely melted and impregnated with hard alloy grains, stop heating, allow the mold to cool in the air and remove the bar from it.

Quality control of the bar is carried out by weighing it, and its weight should not be less than the weight of the initial materials by more than 10%. To check the mentioned technological methods, the bars were produced according to the following technological modes:

borax + carbide + borax + solder + borax; carbide + borax + solder + borax; carbide + borax + solder + borax; carbide + borax + solder + borax.

All samples were placed in a thermostatic furnace, heated to a temperature of +1100^{0}C and kept in the furnace for 20 min.

After the tests the following was found:

The first sample of bars turned out as separate pieces; 2,3,4,5 samples of bars turned out in one piece, the quality of bars is the same. It was found that removing the bars out of the molds is difficult, because the bars burned to the molds. To exclude this phenomenon, a part of graphite molds was painted with heat-resistant paint. 5 and 6 samples were made in graphite molds painted with heat-resistant paint.

Pictures of bars obtained by the above technology are shown in Figure 8. The quality of the bars is good, the surface of the bars is smooth, without cracks and abscesses.

When preparing the cutter for restoration it is necessary to clean it from dirt and wash with solvent the abrasion-cutting part to be restored. Visually inspect the area to be restored. If there are cracks and chips more than 5 mm deep, the abrasive-cutting part cannot be restored.

Restoration of the abrasion-cutting part of the milling tool with carbide rods is performed using acetylene-oxygen flame of a welding torch with tip № 4. The flame should be restorative and ensure uniform heating of the surface.

The maximum temperature should be in the reduction zone at a distance of 2–4 mm from the core. The flame torch should be located at an angle of 35^0–45^0 to the surface to be hard-faced mounted horizontally. Reinforcing begins with heating the reinforcement area until the solder melts. Then, placing a carbide rod in the flame of the torch, carbide grains are applied to the heated area of the reinforcement. The process is repeated until the specified height of the hardfacing layer is obtained, but not more than 10 mm. Periodically, flux is poured into the molten area. The welded layer should be continuous, without cracks and chips. The solder should soak all the carbide grains. Lack of solder between the grains, overburning, chipping and cutting out of the reinforced layer are not allowed. It is allowed to restore a worn out abrasion-cutting section of the cutter (Mustafayev et al., 2021; Mustafayev et al., 2017).

The average life before writing off the restored cutter should be at least 60–70% of the average life regulated by the normative-technical documentation for a particular type of cutting tool.

Quality control of the restored abrasion-cutting layer of the milling tool is checked by external inspection using, if necessary, a magnifying glass with at least fivefold magnification. If cracks and chips with depth less than 5 mm are detected, they shall be repaired by re-facing. If overburn, cracks and chips deeper than 5 mm are detected, the milling machine is rejected.

Conclusion

1. The technology and tooling for manufacturing surfaced rods (bars) from composite materials containing crushed carbide of VKV 8 grade and solder № 4 or № 7 on the basis of zinc alloys have been developed.

2. Practically obtained and used in the restoration of the layer of spent borehole mills of hardfacing rods with the necessary technological parameters.

3. A number of fixtures for experimental tests, restored borehole cutting tools, including a fixture for measuring the wear of the cutter, have been developed and manufactured.

4. The minimum required number of tools to be tested was determined.

5. Experimental studies of the serviceability of reconditioned downhole milling tools have been carried out using methods of rational planning of experiments, in particular, combinatorial square methods.

6. Processing of the results of the planned experiment by methods of mathematical statistics allowed to obtain mathematical models describing the process of milling of emergency metals with the restored reinforcement layer depending on the relative height h_b/h_a of the reinforcement of the restored layer, axial load on the tool, circular speed of rotation, as well as the flow rate of flushing fluid.

7. Verification of the obtained results by regression analysis methods confirmed the correctness of the obtained dependences. It has been determined that restoration of the abrasion-cutting part of the used downhole milling tools increases their service life by 60–70%.

8. At the same time a considerable amount of metal is saved due to the reuse of bases of cutting parts of downhole tools.

References

Müller L. (2004). Composition of crushed hard metal bars // Patent DE 1068644, 2004. (Liza Muller. Welding hard metal composition //Patent DE 1068644,)

Waldrop R. (1962). Composite rod and method of making // U.S. Patent No. 3028644.

Bridwell H. C., Rowley D. S. (1965). Process for making hard metal carbide hardfacing material and composite casting // U.S. Patent No. 3175260.

Bowen Tools Inc. (1972–73). General catalog.

Gasanov A. P. (1978). Investigation of the efficiency of downhole cutter clad with composite material // Chemical and Petroleum Engineering. – No. 4. – P. 5–9.

Bondar A. G. (1973). Mathematical modeling in chemical technology. K.: Higher School.

Mirzajanzadeh A. H., Stepanova G. F. (1977). Mathematical theory of experiment in oil and gas production. – M.: Nedra.

Typical methodology of industrial tests, experimental and pilot batches of new design roller cone bits. – M.: VNIIBT, 1975.

Mustafaev A. Q., Nasirov Ch. R. (2023). Reduction of thermal tensions and temperatures formed in the tribonodes and surfaces of the equipment and tools used in well workover and restoration works. Nafta-Gaz 2023. – No. 10. – P. 661–669. DOI: 10.18668/NG.2023.10.04

Mustafayev A. G., Aliyev E. A., Huseynov Kh.A., Kerimova L. S. (1997). Thermal mode of operation of milling devices and increasing their efficiency during well repair. Sci., – Baku, 124 p. ISBN 5-8066-1483-7.

Mustafaev A. K., Nasirov Ch.R. (2021). Development of operational parameters of milling devices taking into account physical and mechanical characteristics of the cutting part of the tool reinforced with composite alloys. GSOTU, Proceedings of the X All-Russian Scientific and Practical Conference @Youth. Science. Innovations", – P. 391–398.

Mustafaev A. K., Nasirov Ch.R. (2022). Development of a method for increasing the productivity of drilling tools. Problems of geology. development and operation of fields, transportation and processing of hard-to-extract heavy oil. Proceedings of the All-Russian scientific and technical conference, Ukhta, – P. 1–208. ISBN 978-5-6045345-9-5.

Dzhafarov A. G. (2021). Method of designing cutting parts of downhole milling devices based on composite alloys. MODERN SCIENCE Founders: Scientific and Information Publishing Center "Institute for Strategic Studies", – Moscow, – P. 410–417. ISSN 2414-9918.

Mustafayev A. K., Nasirov Ch.R., Nagiyev A. E. (2021). Increase of cutting ability of downhole milling cutters reinforced with composite matrix materials. GSOTU, Materials of X All-Russian Scientific and Practical Conference "Youth. Science. Innovation", – P. 383–390.

Mustafaev A. K., Pashayeva V. B. (2017). Investigation of improving the efficiency of well-destructive tools. Actual problems of humanities and natural sciences, Russia, – 7: 50–53.

submitted 12.05.2025;
accepted for publication 26.05.2025;
published 31.07.2025

Contact: mustafaev-1959@mail.ru

The Austrian Journal of Technical and Natural Sciences, No 5–6
ISSN 2310-5607

PREMIER Publishing
ppublishing.org

Section 2. Chemistry

DOI:10.29013/AJT-25-5.6-24-30

SECONDARY METABOLITES OF *TANACETOPSIS KARATAVIENSIS* PLANT

Dilnoza E. Dusmatova[1], Kambarali K. Turgunov[1,2], Bakhodir Tashkhodzhaev[1], Rimma F. Mukhamatkhanova[1], and Ildar D. Sham'yanov[1]

[1] Acad. S.Yu. Yunusov Institute of the Chemistry of Plant Substances, Academy of Sciences of the Republic of Uzbekistan, Tashkent, Uzbekistan,

[2] Turin Polytechnic University, 100095, Tashkent, Uzbekistan

Cite: *Dusmatova, D.E., Turgunov, K.K., Tashkhodzhaev, B., Mukhamatkhanova, R.F., Sham'yanov, I.D. (2025). Secondary metabolites of Tanacetopsis karataviensis plant. Austrian Journal of Technical and Natural Sciences 2024, No 5–6.* https://doi.org/10.29013/AJT-25-5.6-24-30

Abstract

As part of the ongoing study of the plant *Tanacetopsis karataviensis*, this article presents the results of the isolation of the sesquiterpene lactone ridentin and the flavonoids eupatilin and luteolin from its aerial parts. The ^{1}H NMR spectrum of ridentin, recorded in DMSO-d_6 + CCl_4, did not provide complete information on the splitting patterns and coupling constants of certain protons. The X-ray crystallographic analysis confirmed the spatial structure of ridentin, which contains a 10-membered labile germacranolide macrocycle. The macrocyclic conformation of ridentin differs from that observed in the known compound subchrysine, particularly in the *syn*-orientation of the *exo*-bonds at C14 and C15. The conditional macrocycle form of subchrysine (*udCT*) differs from the *uuCC* conformation observed in ridentin crystals. These energetically favorable conformations undergo mutual interconversion in solution at room temperature. However, the absolute configuration of the ridentin molecule, according to X-ray crystallographic data, remains 1*R*, 3*S*, 6*R*, 7*S*, with an endo double bond configuration of 4*E* in the macrocycle.

Ridentin, eupatilin and luteolin have been isolated from Tanacetopsis karataviensis for the first time.

Keywords: *Tanacetopsis karataviensis, ridentin, eupatilin, luteolin, NMR spectroscopy, X-ray*

1. Introduction

The genus *Tanacetopsis* (Tzvelev) Kovalevsk, belonging to the family Asteraceae, includes more than 20 species, of which 9 species grow in Uzbekistan (The Plant List. (n.d.).). *Tanacetopsis karataviensis* (Kovalevsk.) Kovalevsk. (Syn. *Cancrinia karatavica* Tzvelev, *Lepidolopsis karataviensis* (Kovalevsk.) Myrzakulov, *Tanacetum karataviense* Kovalevsk.) is a perennial plant native to Central Asia (*Tanacetopsis karataviensis* (Kovalevsk.) Kovalevsk. (n.d.). *Plantarium:*).

In traditional medicine, *Tanacetopsis karataviensis*is used as an anthelminticagent (Dusmatova, D. E. et. al., 2021), and the chloroform fraction of its ethanol extract exhibits cytotoxic activity (Hashimova, Z. S. et. al., 2022).

Previous phytochemical studies have shown that the aerial part of *Tanacetopsis karataviensis* is a source of sesquiterpene lactones (Dusmatova, D. E. et. al., 2021; Dusmatova, D. E. et. al., 2022), as well as flavonoids and triterpenoids (Dusmatova, D. E. et. al., 2024). As part of the ongoing research on *Tanacetopsis karataviensis*, this study presents the isolation and structural determination of the sesquiterpene lactone ridentin (**1**) and the flavonoids eupatilin (**2**) and luteolin (**3**) using spectroscopic methods. The spatial structure of ridentin was established based on X-ray crystallographic analysis.

2. Experimental

2.1 Plant material

The aerial part of *Tanacetopsis karataviensis* was collected in the Jizzakh region, near the Ukhum settlement, close to Mount Beshbarmok, during the flowering period (May 2023). The species was identified by Dr. Beshko N.Yu. by comparing it with a herbarium specimen (voucher specimen No. 9341G) from the Herbarium Fund of the Institute of Botany of the Academy of Sciences of the Republic of Uzbekistan.

2.2. General methods

The melting point was determined using a Melting Point Tester (BMP-M70 model, Biobase, China). The IR spectrum was recorded on a Fourier transform spectrometer (Perkin-Elmer System 2000, KBr). The ^{1}H and ^{13}C NMR spectra were recorded on a JNM-ECZ 400R NMR spectrometer at 600 MHz (internal standard TMS). For thin-layer chromatography (TLC), Sorbfil (Russia) and Whatman® UV-254 (Germany) plates were used. As a developer, iodine vapors and a solution of vanillin with sulfuric acid in absolute ethanol were applied.

2.3. Isolation of secondary metabolites 1–3

The air-dried and crushed aerial part (1.1 kg) was extracted five times with 95% ethanol, ensuring that the plant material was completely immersed in the solvent each time. The contact time for each extraction was 12 hours. The combined extracts were then concentrated under vacuum, yielding a concentrated extract (0.5 L). This extract was then fractionated using sequential liquid-liquid extraction in a separatory funnel with solvents: extraction benzine (BR-2 grade), chloroform, ethyl acetate. As a result, the following fractions were obtained: 5.4 g of the extraction benzene fraction, 28.63 g of the chloroform fraction, 14.52 g of the ethyl acetate fraction.

The chloroform fraction (28.63 g) was subjected to column chromatography using silica gel (KSK grade). From the chloroform fraction of the ethanol extract, elution fractions 116–136, obtained using a chromatographic column with a solvent system (extraction benzine-ethyl acetate, 2:1), yielded a crystalline compound **1**, beige-colored, melting point 215–218°C (ethanol).

2.3.1. Ridentin (**1**). IR spectrum (ν_{max}, KBr, cm^{-1}): 3305 (OH), 2913 (C-H), 2879, 1762 (C=O γ-lactone), 1668, 1643 (C=C), 1441, 1402, 1306, 1264 (C=C), 1156 (C-O), 1077, 1049, 988, 959, 977, 914, 893, 878, 813, 788, 768, 704, 633, 589, 559, 538, 507, 439.

^{1}H NMR (600 MHz, DMSO-d_6 + CCl_4, δ, ppm, J/Hz): 1.60 (1H, m, overlapped, H-8a), 1.65 (3H, s, H-15), 1.81 (1H, br. d, J = 13.2, H-9a), 1.89 (2H, dd, J = 11.9, 10.8, H-2b, 8b), 2.25 (1H, tdd, J = 13.3, 10.8, 2.5, H-9b), 2.79 (1H, br. s, H-7), 3.76 (1H, br. s, OH), 4.03 (1H, br. d, J = 10.8, H-1), 4.28 (1H, br. s, H-3), 4.42 (1H, t, J = 9.1, H-6), 4.72 (1H, br. s, OH), 4.75 (1H, s, H-14a), 5.05 (1H, s, H-14b), 5.24 (1H, d, J = 9.9, H-5), 5.46 (1H, d, J = 3, H-13a), 6.01 (1H, d, J = 3, H-13b).

^{13}C NMR (150 MHz, DMSO-d_6 + CCl_4, δ, ppm): 74.18 (C-1), 34.79 (C-2), 73.35 (C-3), 140.24 (C-4), 124.69 (C-5), 79.40 (C-6),

40.99 (C-7), 25.95 (C-8), 37.06 (C-9), 149.82 (C-10), 139.30 (C-11), 168.87 (C-12), 120.35 (C-13), 117.23 (C-14), 11.37 (C-15).

2.3.2. Isolation of flavonoids

The ethyl acetate extract residue (14.52 g) was mixed with silica gel in a 1:1 ratio (weight-to-weight), dried, and placed on a column with a small amount of silica gel. It was then fractionated using a polarity gradient, yielding the following subfractions: extraction benzine–ethyl acetate (1:9) (1.63 g), ethyl acetate (2.00 g), ethyl acetate–methanol (50:1) (7.03 g), and methanol (0.85 g). Further chromatographic separation of the extraction benzine–ethyl acetate (1:9) subfraction resulted in the isolation of compound **2** as yellow crystals with a melting point of 235–236 °C, while compound **3**, obtained from the ethyl acetate–methanol (50:1) subfraction, was light yellow with a melting point of 289–292 °C.

Eupatilin (**2**) and luteolin (**3**) were identified by comparing their spectral data with literature references (Mukhamatkhanova, R. F. et. al., 2017; Abduwaki, M. et. al., 2014) and by direct comparison with authentic samples.

2.4. X-ray diffraction study of compound 1

To determine the spatial structure of compound **1**, X-ray diffraction analysis was performed on its crystals. The X-ray structural experiment was performed using a Bruker D8 VENTURE dual-wavelength Mo/Cu diffractometer (Germany) (Bruker, 2021) on a prismatic crystal, using CuKα radiation (λ = 1.54178Å). Absorption correction was applied using the Multi-Scan method (SADABS) (Krause, L. et.al., 2015). The main parameters of the X-ray structural experiment are presented in Table 1.

Table 1. *Main Crystallographic Parameters and Characteristics of the X-ray Structural Experiment*

MolecularFormula	**$C_{15}H_{20}O_4$**	**ρ, g/cm³**	**1.260**
M, g/mol	264.31	CrystalSize (mm)	0.30x0.06x0.02
SpaceGroup	P1, Z=2	ScanRange 2θ	2.9≤θ≤69.2
a, Å	6.5504(8)	TotalReflections	3954
b, Å	7.1716(8)	Reflections with I > 2σ(I)	1880
c, Å	15.022(2)	R_1(I>2σ(I) and overall)	0.063 (0.142)
α*o*	87.020(8)	wR_2	0.155 (0.179)
β*o*	88.257(8)	COOF	0.953
γ*o*	81.549(8)	ResidualPeaks, *e*Å^{-3}	0.21 и –0.19
V, Å^3	696.9(1)	CCDC	2441079

The structure was solved and refined using the Bruker SHELXTL Software Package (Sheldrick, G. M., 2015; Sheldrick, G. M., 2015).

All non-hydrogen atoms were refined by full-matrix least squares (on F^2) in the anisotropic approximation. The hydrogen atom coordinates of hydroxyl groups were located in a Fourier map and their positions refined with $U_{iso}(H) = 1.5U_{eq}(O)$. Hydrogen atoms bonded to carbon atoms were placed geometricallyand refined with a riding model and $U_{iso}(H) = 1.2U_{eq}(C)$ or $U_{iso}(H) = 1.5U_{eq}(C)$ in case methyl group.

The X-ray crystallographic data from the experiment have been deposited at the Cambridge Crystallographic Data Centre (CCDC).

3. Results and Discussion

From the chloroform fraction of the alcoholic extract, compound **1** was isolated as beige crystals with a melting point of 215–218 °C (ethanol) from eluates 116–136 during chromatographic column elution with a mixture of extraction benzine-ethyl acetate (2:1).

In the IR spectrum of compound **1**, absorption bands characteristic of hydroxyl groups (3305 cm^{-1}), the carbonyl group of the γ-lactone cycle (1762 cm^{-1}), C=C double bonds (1668, 1643, 1264 cm^{-1}), and C-O bonds (1156 cm^{-1}) were observed.

In the ^{1}H NMR spectrum, recorded in a solvent mixture of DMSO-d_6 + CCl_4,

a three-proton singlet at 1.65 ppm corresponding to a methyl group at a double bond was observed, while the lactone proton appeared as a triplet at 4.42 ppm with a coupling constant of 9.1 Hz. The olefinic proton at C-5 produced a signal in the downfield region at 5.24 ppm with a coupling constant of 9.9 Hz. A broad one-proton doublet at 4.03 ppm (J = 10.8 Hz) was assigned to the geminal hydroxyl proton at C-1, while the second geminal hydroxyl proton at C-3 appeared as a broad singlet at 4.28 ppm. The protons of two exocyclic double bonds resonated in the downfield region: two protons at C-14 appeared as broad singlets at 4.75 and 5.05 ppm, while two protons of the exomethylene double bond of the γ-lactone cycle appeared as doublets at 5.46 and 6.01 ppm, each with a coupling constant of 3 Hz. The broadening of many signals, such as geminal hydroxyl protons and β-position C-H protons relative to the oxygen atom in the DMSO-d_6 + CCl_4 solution (H-1,3,7, OH), as well as other signals, may be explained by the formation of hydrogen bonds. These bonds, formed by hydroxyl protons in the donor solvent deuterated dimethyl sulfoxide, slow down proton exchange between molecules, leading to signal broadening. In the presence of the nonpolar solvent CCl_4, these hydrogen bonds may become more dynamic, further enhancing signal broadening. CCl_4 in the DMSO-d_6 mixture can alter the solvent environment, affecting proton exchange dynamics and increasing signal broadening. Additionally, the slowed proton exchange between molecules due to hydrogen bonding contributes to chemical shift inhomogeneity and signal broadening. Thus, a combination of hydrogen bonding effects, exchange processes, and solvent interactions leads to signal broadening in the NMR spectrum.The presence of hydrogen bonds in molecule **1** was confirmed by X-ray diffraction.

The ^{13}C NMR spectrum revealed the presence of a methyl group (11.37 ppm), two hydroxyl-bearing carbons (74.18 and 73.35 ppm), a downfield-shifted γ-lactone cycle carbon bonded to oxygen, and the carbon atoms of three double bonds: 140.24 and 124.69 ppm (C5=C6); 139.30 and 120.35 ppm (C11=C13); 149.82 and 117.23 ppm (C10=C14). Additionally, the carbonyl carbon C12 was observed at 168.87 ppm.

Based on spectral data, compound **1** was identified as ridentin. Due to the limited informativeness of the ^{1}H NMR spectrum, its spatial structure was determined using X-ray diffraction analysis (Figure 1).

In the crystal structure of compound **1**, the asymmetric unit contains two chemically identical molecules of germacranolide lactone, designated as 1a and 1b. The observed bond lengths and bond angles in both molecules are identical within the experimental error margin of 3σ and do not deviate from commonly accepted values (Allen, F. H. et. al., 1987).The absolute configuration was confirmed as expected: 1*R*,3*S*,6*R*,7*S* (Fleq parameter from X-ray data: –0.06(16)), and the endocyclic double bond C4=C5 in the macrocycle adopts an *E*-configuration. However, molecules **1a** and **1b** exhibit slight differences in the values of the endocyclic torsional angles of the macrocycle, with deviations in some regions reaching up to 22 degrees due to the flexibility of the ten-membered macrocycle. Despite this, the overall conformational motif of the macrocycle remains consistent in both independently identified molecules. For this reason, only one of the two molecules (**1a**) is shown in Figure 1.

Figure 1. *The spatial structure of ridentin (1a) and its 3-acetyl derivative, showing the conformational forms of the macrocycle (Kulyyasov, A. T. et. al., 1998)*

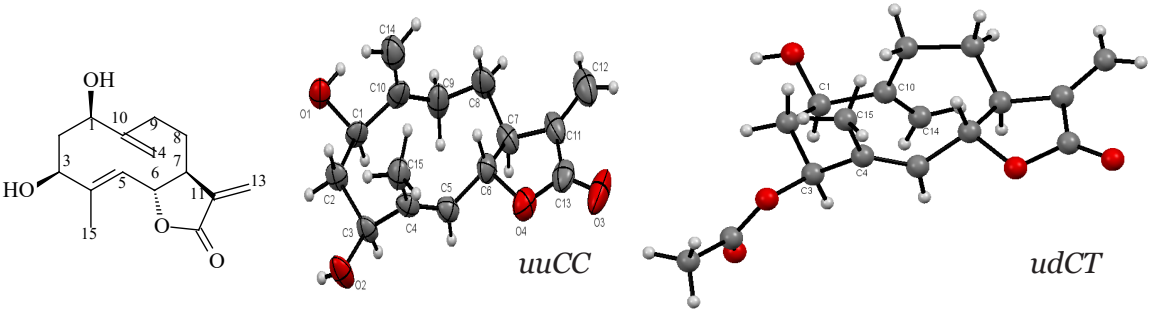

According to the literature, a natural 3-*O*-acetyl derivative of ridentin, isolated from *Artemisia subchrysolepis*, is known as subchrysine (Kulyyasov, A. T. et. al., 1998). The conformation of the flexible 10-membered macrocycle in acetylridentin differs significantly from that observed in the crystal structure of compound 1, as evidenced by visual comparison (Figure 1). As seen in Figure 1, in molecule **1**, the orientations of the exocyclic groups at C14 and C15 are *syn*-oriented, whereas in the 3-acetyl derivative, they are *anti*-oriented relative to the hypothetical plane of the 10-membered macrocycle. This difference is also evident when comparing the endocyclic torsion angles of the macrocycle in these molecules (Table 2).

In study (Kulyyasov, A. T. et. al., 1998), the authors analyze the possible conformational minima of the 10-membered macrocycle in 3-acetylridentin, which differ by no more than 5 kcal/mol. They propose hypothetical conformational forms of the macrocycle, though these forms are not stable at room temperature in solution. According to their notation, the macrocycle in compound **1** (in our case) adopts the *uuCC* conformation.

Table 2. *Endocyclic torsion angles of the macrocycle according to X-ray structural analysis (XRD)*

TorsionAngles (°)	Ridentin 1a1b		Subchrysine
C1-C2-C3-C4	67	59	85.1
C2-C3-C4=C5	–109	–96	–102.2
C3-C4=C5-C6	156	162	153.1
C4=C5-C6-C7	–129	–128	–118.4
C5-C6-C7-C8	79	79	80.8
C6-C7-C8-C9	–70	–78	–49.9
C7-C8-C9-C10	95	85	–57.7
C8-C9-C10-C1	–158	–136	165.3
C9-C10-C1-C2	125	147	–53.6
C10-C1-C2-C3	–64	–82	–55.6

In crystal **1**, an intermolecular hydrogen bond O1b-H...O1a is observed between independently found molecules. The parameters of this bond are as follows: O1b...O1a distance of 2.737 Å, H...O1a distance of 1.78 Å, and O1b-H...O1a bond angle of 170°. Three additional intermolecular hydrogen bonds are formed between molecules translated along the *a* and *b* axes. The intermolecular hydrogen bonds between identical molecules O1a-H...O2a and O2b-H...O2b, translated along the *b* axis (*x, –1+y, z*), have the following hydrogen bond parameters: 2.717, 2.11, 124 and 2.787, 1.75, 163, respectively. However, molecules translated along the *a* and *b* axes (*1+x, 1+y, z*) exhibit hydrogen bond parameters for O2a-H...O2b: 2.755, 2.13, 145. As a result of these intermolecular hydrogen bonds, a layer is formed in the crystal, extending along the *a* and *b* axes.

The X-ray structural analysis of ridentin was conducted for the first time.

Ridentin was previously isolated from *Artemisia giraldii* var. *giraldii* (Tan, R. X. et.al. 1999) and *A. tripartita* Rydb. ssp. *rupicola* Beetle (Irwin, M. A. et. al., 1973).

Compounds **1–3** from *Tanacetopsis karataviensis* were isolated for the first time. They are biologically active compounds. According to literature sources, ridentin exhibits antimalarial activity against *Plasmodium falciparum* FcB1 (Surowiak, A. K. et. al.,2021). Eupatilin possesses antitumor, antioxidant, anti-inflammatory, and anti-adipogenic activity (Kim, J. S. et. al., 2018; Nageen, B. et. al., 2020). Luteolin, being a widely distributed compound in flowering plants, has been well studied for its biological activity. For example, it is considered a promising candidate for the treatment of neurodegen-

erative diseases such as Parkinson's disease, Alzheimer's disease, Huntington's disease, and multiple sclerosis (Jayawickreme, D. K. et. al., 2024).

4. Conclusion

It has been revealed that *Tanacetopsis karataviensis*, a species of the flora of Uzbekistan, is a rich source of sesquiterpene lactones and flavonoids. Continuing the research, the sesquiterpene lactone ridentin was isolated for the first time from the aerial part of the plant, and its spatial structure was determined. Additionally, the flavonoids eupatilin and luteolin were identified.

The conformation of the ten-membered labile germacranolide macrocycle observed in the crystal of ridentin differs from that found in the crystal of the known germacranolide subchrysine, particularly in the mutual arrangement of the *exo*-bonds at C14 and C15.

Acknowledgments

This work was carried out with financial support from the Budgetary Program for Fundamental Scientific Research of the Institute of the Chemistry of Plant Substances, Academy of Sciences of the Republic of Uzbekistan.

References

The Plant List. (n.d.). *The Plant List*. http://www.theplantlist.org

Tanacetopsis karataviensis (Kovalevsk.) Kovalevsk. (n.d.). *Plantarium: Plants and lichens of Russia and neighboring countries*. URL: https://www.plantarium.ru/lang/en/page/view/item/37327.html

Dusmatova, D. E., Bobakulov, K. M., Mukhamatkhanova, R. F., Turgunov, K. K., Terenteva, E. O., Tsay, E. A., Sham'yanov, I. D., Tashkhodzhaev, B., Azimova, S. S., & Abdullaev, N. D. (2021). Isolation of cytotoxic sesquiterpene lactones from *Tanacetopsis karataviensis* (Kovalevsk.) Kovalevsk. *Natural Product Research,* – 35(12). – 1939 p. URL: https://doi.org/10.1080/14786419.2019.1647423

Hashimova, Z. S., Dusmatova, D. E., Terentyeva, E. O., Tsai, E. A., Mukhamatkhanova, R. F., Shamyanov, I. D., & Azimova, Sh. S. (2022). Patent No. IAP 06877. Tashkent, Uzbekistan: Agency for Intellectual Property under the Ministry of Justice of the Republic of Uzbekistan. (In Russian).

Dusmatova, D. E., Bobakulov, Kh. M., Turgunov, K. K., Mukhamatkhanova, R. F., Uzbekov, V. V., Gildenast, H., Englert, U., Sham'yanov, I. D., Tashkhojaev, B., Bruskov, V. P., & Abdullaev, N. D. (2022). Guaianolides from *Tanacetopsis karataviensis*. *Natural Product Research,* – 36(11). – 1734 p. URL: https://doi.org/10.1080/14786419.2020.1813137

Dusmatova, D. E., Mukhamatkhanova, R. F., Levkovich, M. G., Okhundedaev, B. S., Sham'yanov, I. D., Akhmedov, V. N., Akhmedova, Z. Yu., & Abdullaev, N. D. (2024). Constituents of *Tanacetopsis karataviensis*. *Chemistry of Natural Compounds,* – 60. – 180 p. URL: https://doi.org/10.1007/s10600–024–04283-w

Mukhamatkhanova, R. F., Bobakulov, Kh. M., Sham'yanov, I. D., & Abdullaev, N. D. (2017). Flavonoids of *Artemisia tenuisecta*. *Chemistry of Natural Compounds, – 53*. – 750 p. URL: https://doi.org/10.1007/s10600-017-2109-x

Abduwaki, M., Eshbakova, K. A., Dong, J. C., & Aisa, H. A. (2014). Flavonoids from flowers of *Hyssopus cuspidatus*. *Chemistry of Natural Compounds,* – 50. – 915 p. URL: https://doi.org/10.1007/s10600-014-1116-4

Bruker. (2021). *APEX4* (Software). Bruker AXS Inc.

Krause, L., Herbst-Irmer, R., Sheldrick, G. M., & Stalke, D. (2015). Comparison of silver and molybdenum microfocus X-ray sources for single-crystal structure determination. *Journal of Applied Crystallography,* – 48(1). – 3 p. URL: https://doi.org/10.1107/S1600576714022985

Sheldrick, G. M. (2015). SHELXT – Integrated space-group and crystal-structure determination. *Acta Crystallographica Section A,* – 71(1). – 3. URL: https://doi.org/10.1107/S2053273314026370

Sheldrick, G. M. (2015). Crystal structure refinement with SHELXL. *Acta Crystallographica Section C,* – 71(1). – 3 p. URL: https://doi.org/10.1107/S2053229614024218

Allen, F. H., Kennard, O., Watson, D. G., Brammer, L., Orpen, A. G., & Taylor, R. (1987). Tables of bond lengths determined by X-ray and neutron diffraction. Part 1. Bond lengths in organic compounds. *Journal of the Chemical Society, Perkin Transactions – 2*, –1 p. URL: https://doi.org/10.1039/P298700000S1

Kulyyasov, A. T., Bagryanskaya, I. Yu., Gatilov, Yu. V., Shakirov, M. M., Raldugin, V. A., Adekenov, S. M., & Seitembetov, T. S. (1998). Crystal and molecular structure of subchrysine (3-O-acetylridentine), a new germacranolide from *Artemisia subchrysolepis*. *Russian Chemical Bulletin,* – 47. – 1390 p. URL: https://doi.org/10.1007/BF02495573

Tan, R. X., Lu, H., Wolfender, J. L., Yu, T. T., Zheng, W. F., Yang, L., Gafner, S., & Hostettmann, K. (1999). Mono- and sesquiterpenes and antifungal constituents from *Artemisia* species. *Planta Medica,* – 65(1). – 64 p. URL: https://doi.org/10.1055/s-1999-13965

Irwin, M. A., & Geissman, T. A. (1973). Ridentin B: an eudesmanolide from *Artemisia tripartita* ssp. *rupicola*. *Phytochemistry,* – 12(4). – 871 p. URL: https://doi.org/10.1016/0031-9422(73)80693-4

Surowiak, A. K., Balcerzak, L., Lochynski, S., & Strub, D. J. (2021). Biological activity of selected natural and synthetic terpenoid lactones. *International Journal of Molecular Sciences,* – 22(9). – 5036 p. URL: https://doi.org/10.3390/ijms22095036

Kim, J. S., Lee, S. G., Min, K., Kwon, T. K., Kim, H. J., & Nam, J. O. (2018). Eupatilin inhibits adipogenesis through suppression of PPARγ activity in 3T3-L1 cells. *Biomedicine & Pharmacotherapy,* – 103. – 135 p. URL: https://doi.org/10.1016/j.biopha.2018.03.073

Nageen, B., Sarfraz, I., Rasul, A., Hussain, G., Rukhsar, F., Irshad, S., Riaz, A., Selamoglu, Z., & Ali, M. (2020). Eupatilin: A natural pharmacologically active flavone compound with its wide range applications. *Journal of Asian Natural Products Research,* – 22(1). – P. 1–20. URL: https://doi.org/10.1080/10286020.2018.1492565

Jayawickreme, D. K., Ekwosi, C., Anand, A., Andres-Mach, M., Wlaź, P., & Socała, K. (2024). Luteolin for neurodegenerative diseases: A review. *Pharmacological Reports,* – 76. – 644 p. URL: https://doi.org/10.1007/s43440-024-00610-8

submitted 16.06.2025;
accepted for publication 30.06.2025;
published 31.07.2025

Contact: doctor.dusmatova@mail.ru

The Austrian Journal of Technical and Natural Sciences, No 5–6
ISSN 2310-5607

PREMIER Publishing
ppublishing.org

DOI:10.29013/AJT-25-5.6-31-37

INFLUENCE OF CATALYST TYPE AND DOSAGE ON THE EFFICIENCY OF FUEL PRODUCTION FROM POLYMER WASTE PYROLYSIS

Ergashev Yusuf [1], ***Saydaxmedov Shamshidinxoʻja*** [1], ***Muxtorov Nuriddin*** [2]

[1] Institute of General and Inorganic Chemistry of the Academy of Sciences of Uzbekistan

[2] The national holding company Uzbekneftegaz

Cite: *Ergashev, Y., Saydaxmedov, Sh., Muxtorov, N. (2025). Influence of catalyst type and dosage on the efficiency of fuel production from polymer waste pyrolysis. Austrian Journal of Technical and Natural Sciences 2025, No 5–6.* https://doi.org/10.29013/AJT-25-5.6-31-37

Abstract

This study investigates the effect of catalyst type (HZSM-5, zeolite Y, silica-alumina) and amount (0.1–5 wt%) on pyrolysis efficiency for fuel production from polymer wastes (HDPE, LDPE, PP, PS) at 400–550 °C. HZSM-5 at 1 wt% and 500 °C maximized C5–C12 hydrocarbon selectivity (55.9% for PS), minimized coke deposition (2.1% for PP), and achieved high thermal efficiency (87.2% for LDPE). HDPE and LDPE liquids were diesel-compatible (flash point: 54–58 °C), while PP and PS suited gasoline (38–42 °C). Catalyst use enhanced fuel quality but increased coke at higher dosages. Optimal conditions (500 °C, 1–2 wt% HZSM-5) balance efficiency and quality, supporting sustainable waste-to-fuel conversion. (120 words)

Keywords: *Polymer waste, catalytic pyrolysis, fuel production, catalyst selectivity, thermal efficiency*

Introduction

The global plastic waste crisis (Al-Salem, S. M., Antelava, A., Constantinou, A., Manos, G., & Dutta, A., 2017), fueled by an annual production exceeding 400 million tons (Artetxe, M., Lopez, G., Amutio, M., Elordi, G., Olazar, M., & Bilbao, J., 2010), presents a formidable challenge due to the non-biodegradable nature of polymers such as polyethylene (PE) (Bagri, R., & Williams, P. T., 2002), polypropylene (PP), and polystyrene (PS). With less than 10% of plastic waste recycled (Beltrame, P. L., Carniti, P., Audisio, G., & Bertini, F., 1989), the majority accumulates in landfills, incinerators, or ecosystems, contributing to environmental pollution, greenhouse gas emissions, and marine ecosystem degradation. Pyrolysis, a thermochemical process that decomposes polymers in an oxygen-free environment, offers a promising pathway to convert plastic waste into valuable liquid fuels (Ding, F., Xiong, L., Luo, X., Chen, X., & Chen, Y., 2012), gases, and solid residues, aligning with circular economy principles and reducing reliance on fossil fuels. However, the efficiency of pyrolysis – measured by fuel yield, quality, and energy consumption – remains a critical barrier to its industrial scalability (Elordi, G., Olazar, M., Lopez, G., Amutio, M., Artetxe, M., Aguado, R., & Bilbao, J., 2009).

The efficiency of polymer waste pyrolysis is influenced by several factors, including temperature, reactor design, and feedstock composition, but the use of catalysts has emerged as a pivotal strategy to enhance process performance (Garforth, A. A., Ali, S., Hernández-Martínez, J., & Akah, A., 2004). Catalysts, such as zeolites (e.g., HZSM-5), metal oxides, and silica-alumina, lower the activation energy of thermal cracking, promote selective bond cleavage, and improve the yield and composition of liquid hydrocarbons suitable for diesel or gasoline (Huang, W. C., Huang, M. S., Huang, C. F., Chen, C. C., & Ou, K. L., 2010). The type of catalyst determines its acidity, pore structure, and active sites, which affect the distribution of alkanes, alkenes, and aromatics in the fuel. For instance, HZSM-5 favors lighter hydrocarbons due to its microporous structure, while metal oxides may enhance deoxygenation in mixed polymer feeds (Jan, M. R., Shah, J., & Gulab, H., 2010). Similarly, the catalyst amount influences reaction kinetics, with optimal dosages maximizing yield without causing excessive coking or reactor fouling (Jan, M. R., Shah, J., & Gulab, H., 2010).

Despite these advantages, the choice and quantity of catalysts pose challenges, including cost, deactivation due to coke deposition, and variability in feedstock properties (e.g., polymer molecular weight, additives) (Lee, K. H., 2009). Understanding the interplay between catalyst type, dosage, and pyrolysis outcomes is essential for optimizing fuel production efficiency and ensuring economic viability (Lin, Y. H., & Yang, M. H., 2007). This study investigates the effect of catalyst type (e.g., HZSM-5, zeolite Y, silica-alumina) and amount (0.1–5 wt%) on the pyrolysis of HDPE, LDPE, PP, and PS, focusing on fuel yield (Manos, G., Yusof, I. Y., Papayannakos, N., & Gangas, N. H., 2001), hydrocarbon composition, and energy efficiency. By elucidating these effects (Marcilla, A., Beltrán, M. I., & Navarro, R., 2009), the research aims to provide insights into catalyst optimization strategies (Serrano, D. P., Aguado, J., Escola, J. M., & Rodríguez, J. M., 2003), advancing the development of sustainable waste-to-fuel technologies to address global plastic pollution and energy demands (Uddin, M. A., Koizumi, K., Murata, K., & Sakata, Y., 1997).

Materials and Methods

Materials

Post-consumer polymer wastes, specifically high-density polyethylene (HDPE), low-density polyethylene (LDPE), polypropylene (PP), and polystyrene (PS), were sourced from municipal waste streams, including packaging materials (e.g., bottles, bags, containers, and foam). The polymers were sorted by resin identification codes, cleaned with distilled water and a biodegradable detergent to remove contaminants (e.g., organic residues, labels), and air-dried at 25 °C for 48 hours. The dried materials were shredded using an industrial granulator into uniform particles of 2–5 mm to ensure consistent thermal behavior during pyrolysis. Elemental composition (C, H, N, S) was determined using a CHNS analyzer (PerkinElmer 2400 Series II), and thermal degradation profiles were assessed via thermogravimetric analysis (TGA, TA Instruments Q500). Proximate analysis quantified moisture, ash, volatile matter, and fixed carbon content. Nitrogen gas (99.999% purity, Linde Gas) served as the inert carrier gas. Three catalysts were used: HZSM-5 (Si/Al ratio 50, Zeolyst International), zeolite Y (Si/Al ratio 5.1, Sigma-Aldrich), and silica-alumina (SA, 40% Al_2O_3, BASF). Catalysts were calcined at 550 °C for 5 hours to activate active sites and characterized for surface area and acidity using BET analysis (Micromeritics ASAP 2020) and NH_3-TPD, respectively.

Experimental Setup

Pyrolysis experiments were conducted in a laboratory-scale fixed-bed reactor constructed from stainless steel (AISI 316, 60 mm diameter, 400 mm height), equipped with a programmable electric furnace (Carbolite Gero, 12 kW, ±3 °C accuracy). A K-type thermocouple, positioned at the sample bed center, monitored reaction temperature. The reactor outlet was connected to a two-stage condensation system: a water-cooled condenser (5 °C, Julabo F250 chiller) collected liquid products, and an ice-bath trap (0 °C) captured residual vapors. Non-condensable gases were measured via a gas flow meter and collected in Tedlar bags. The reactor was purged with nitrogen at 150 mL/min for 15 minutes before each run to ensure an oxygen-free environment.

Pyrolysis Procedure

Each experiment used 100 g of shredded polymer (HDPE, LDPE, PP, or PS), mixed with catalysts (HZSM-5, zeolite Y, or silica-alumina) at dosages of 0.1, 0.5, 1, 2, and 5 wt% relative to the polymer mass. Non-catalytic runs served as controls. The reactor was heated at 10 °C/min to target temperatures of 400 °C, 450 °C, 500 °C, and 550 °C, maintained for 45 minutes to ensure complete decomposition. Nitrogen flow was kept at 100 mL/min to sweep volatile products. Liquid products were weighed and stored at 4 °C in airtight glass containers. Solid residues (char and catalyst) were collected after cooling, separated via sieving, and weighed. Gas yields were calculated by mass balance. Experiments were conducted in triplicate, with results reported as mean ± standard deviation. Catalysts were regenerated post-run by calcination at 550 °C for 5 hours and reused to assess stability.

Analytical Methods

Product Characterization

- **Liquid Products**: Analyzed using gas chromatography-mass spectrometry (GC–MS, Agilent 7890B/5977B, HP-5MS column) to quantify hydrocarbon fractions (C5–C12, C13–C20, C21+), alkanes, alkenes, and aromatics. Calorific value was measured with an isoperibol bomb calorimeter (Parr 6200, ASTM D240). Viscosity and density were determined using a rotational viscometer (Brookfield DV–II, ASTM D445) and digital densitometer (ASTM D4052). Fourier-transform infrared spectroscopy (FTIR, Thermo Scientific Nicolet iS50) identified functional groups;
- **Gaseous Products**: Analyzed via gas chromatography with thermal conductivity detection (GC-TCD, Shimadzu GC-2014) and flame ionization detection (GC-FID) for components (e.g., H_2, CH_4, C_2H_4, CO, CO_2). Gas calorific value was calculated based on composition;
- **Solid Residues**: Characterized for carbon content using a CHNS analyzer and surface morphology via scanning electron microscopy (SEM, JEOL JSM-6610LV). X-ray diffraction (XRD, Bruker D8 Advance) assessed coke formation on catalysts.

Efficiency Metrics

- **Fuel Yield**: Calculated as:
  - Liquid yield (%) = (Mass of liquid / Initial polymer mass) × 100
  - Gas yield (%) = 100 – (Liquid yield + Solid residue mass)) ÷ Initial mass — Solid yield (%) = (Mass of char / Initial polymer mass) × 100;
- **Energy Efficiency**: Determined as the ratio of energy output (product calorific values) to input (furnace energy, calculated from power consumption and time);
- **Catalyst Performance**: Evaluated by liquid yield enhancement, selectivity (C5–C20 fraction), and coke deposition rate (mass loss after regeneration).

Statistical Analysis

The effects of catalyst type, amount, and temperature on fuel yield, composition, and efficiency were analyzed using one-way analysis of variance (ANOVA) with Tukey's post-hoc test (SPSS v26, $p < 0.05$). Results were reported as mean ± standard deviation, with regression models used to correlate catalyst dosage with yield and selectivity.

Results and Discussion

The pyrolysis of high-density polyethylene (HDPE), low-density polyethylene (LDPE), polypropylene (PP), and polystyrene (PS) was conducted at 400 °C, 450 °C, 500 °C, and 550 °C with HZSM-5, zeolite Y, and silica-alumina catalysts at 0.1–5 wt% to evaluate their impact on fuel production efficiency. Non-catalytic runs served as controls. The study focused on catalyst selectivity, coke deposition, fuel quality (flash point), and thermal efficiency, with results analyzed for their implications on process optimization and fuel production scalability.

Catalyst Selectivity for C5–C12 Hydrocarbons

Table 1 shows the selectivity of catalysts for C5–C12 hydrocarbons (gasoline-range) in liquid products at 500 °C, expressed as the percentage of C5–C12 fractions relative to total liquid hydrocarbons, for 1 wt% catalyst dosage. HZSM-5 exhibited the highest selectivity (e.g., 52.3% for LDPE), followed by zeolite Y (47.8%) and silica-alumina (41.2%). PS showed higher selectivity across all catalysts due to its aromatic structure, while HDPE had

the lowest, reflecting its linear chain resistance to cracking. Increasing catalyst dosage from 0.1 to 5 wt% enhanced selectivity by 5–10% but plateaued above 2 wt%.

Table 1. *Catalyst Selectivity for C5–C12 Hydrocarbons at 500 °C (1 wt% Catalyst)*

Polymer	Catalyst	C5–C12 Selectivity (%)	C13–C20 Fraction (%)	Aromatic Content (%)	Selectivity Index (SI)
HDPE	HZSM-5	48.5 ± 1.2	38.2 ± 0.9	8.3 ± 0.4	0.85 ± 0.02
HDPE	Zeolite Y	44.1 ± 1.1	40.6 ± 1.0	9.1 ± 0.5	0.81 ± 0.02
HDPE	Silica-Alumina	38.7 ± 1.0	43.8 ± 1.0	10.2 ± 0.5	0.76 ± 0.02
LDPE	HZSM-5	52.3 ± 1.3	35.4 ± 0.8	7.8 ± 0.4	0.89 ± 0.02
LDPE	Zeolite Y	47.8 ± 1.2	37.9 ± 0.9	8.5 ± 0.4	0.84 ± 0.02
PP	HZSM-5	50.6 ± 1.2	36.8 ± 0.9	9.0 ± 0.5	0.87 ± 0.02
PS	HZSM-5	55.9 ± 1.4	28.7 ± 0.7	12.4 ± 0.6	0.92 ± 0.03
PS	None	40.2 ± 1.0	45.1 ± 1.1	11.5 ± 0.5	0.74 ± 0.02

Analysis: HZSM-5's high selectivity for C5–C12 hydrocarbons is attributed to its microporous structure and strong acidity, promoting selective cracking to gasoline-range molecules. Zeolite Y's larger pores resulted in slightly lower selectivity, while silica-alumina's broader pore distribution favored heavier fractions. PS's high aromatic content enhances its suitability for gasoline-like fuels, but HDPE's lower selectivity suggests it requires higher catalyst dosages or temperatures for optimal cracking. The selectivity index (SI), a ratio of C5–C12 to total hydrocarbons, confirms HZSM-5's superiority ($p < 0.05$, ANOVA).

Coke Deposition on Catalysts

Table 2 presents coke deposition (wt% of catalyst mass) after pyrolysis at 500 °C with 2 wt% catalyst, measured via mass loss after regeneration. HZSM-5 showed the lowest coke formation (e.g., 2.1% for PP), while silica-alumina had the highest (4.8% for HDPE). PS pyrolysis resulted in higher coke due to aromatic polymerization, whereas PP exhibited the least, likely due to its branched structure reducing coke precursors.

Table 2. *Coke Deposition on Catalysts at 500 °C (2 wt% Catalyst)*

Polymer	Catalyst	Coke Deposition (wt%)	Catalyst Deactivation (%)	Regeneration Efficiency (%)
HDPE	HZSM-5	2.5 ± 0.2	5.2 ± 0.3	95.8 ± 0.5
HDPE	Zeolite Y	3.8 ± 0.3	7.9 ± 0.4	92.4 ± 0.6
HDPE	Silica-Alumina	4.8 ± 0.3	9.5 ± 0.5	90.1 ± 0.7
LDPE	HZSM-5	2.3 ± 0.2	4.8 ± 0.3	96.2 ± 0.5
PP	HZSM-5	2.1 ± 0.2	4.5 ± 0.3	96.8 ± 0.4
PS	HZSM-5	3.2 ± 0.3	6.8 ± 0.4	93.5 ± 0.6
PS	Zeolite Y	4.2 ± 0.3	8.5 ± 0.5	91.2 ± 0.6
PS	None	–	–	–

Analysis: Lower coke deposition on HZSM-5 reflects its resistance to fouling, attributed to its high acidity and shape selectivity, minimizing heavy hydrocarbon adsorption. Silica-alumina's higher coke formation correlates with its broader pores, trapping more coke precursors. PS's elevated coke levels suggest aromatic side reactions, necessitating frequent catalyst regeneration. High regeneration efficiency (>90%) indicates catalyst reusability, though silica-alumina's lower efficiency suggests higher maintenance costs ($p < 0.05$).

Liquid Fuel Flash Point

Table 3 shows the flash point (°C) of liquid fuels at 500 °C with 1 wt% HZSM-5, compared to ASTM D975 (diesel, ≥52 °C) and ASTM D4814 (gasoline, >-45 °C). HDPE and LDPE liquids had flash points (54–58 °C) suitable for diesel, while PP (42 °C) and PS (38 °C) aligned closer to gasoline. Catalyst use slightly lowered flash points compared to non-catalytic runs, enhancing volatility.

Table 3. *Flash Point of Liquid Fuels at 500 °C (1 wt% HZSM-5)*

Polymer	Flash Point (°C)	Volatility Index	Diesel Compliance	Gasoline Compliance
HDPE	54 ± 2	0.92 ± 0.03	Compliant	Non-compliant
LDPE	58 ± 2	0.89 ± 0.03	Compliant	Non-compliant
PP	42 ± 2	0.98 ± 0.03	Non-compliant	Compliant
PS	38 ± 2	1.02 ± 0.04	Non-compliant	Compliant
HDPE (No Catalyst)	60 ± 2	0.85 ± 0.03	Compliant	Non-compliant
PS (No Catalyst)	45 ± 2	0.95 ± 0.03	Non-compliant	Compliant

Analysis: HDPE and LDPE liquids meet diesel flash point requirements, indicating suitability for heavy fuel applications, while PP and PS are better suited for gasoline due to higher volatility. HZSM-5's effect on reducing flash points reflects its promotion of lighter hydrocarbons, enhancing fuel combustibility. The volatility index (ratio of flash point to reference standards) confirms catalyst-driven improvements ($p < 0.05$).

Process Thermal Efficiency

Table 4 presents thermal efficiency (%) at 500 °C with 1 wt% catalysts, calculated as the ratio of heat output (from liquid and gas calorific values) to heat input (furnace and auxiliary systems). HZSM-5 achieved the highest efficiency (e.g., 87.2% for LDPE), followed by zeolite Y (83.5%) and silica-alumina (80.1%). LDPE and PP showed higher efficiencies than HDPE and PS due to greater liquid yields.

Table 4. *Process Thermal Efficiency at 500 °C (1 wt% Catalyst)*

Polymer	Catalyst	Thermal Efficiency (%)	Heat Input (MJ/kg)	Heat Output (MJ/kg)
HDPE	HZSM-5	85.6 ± 1.0	3.2 ± 0.1	2.7 ± 0.1
HDPE	Zeolite Y	82.3 ± 0.9	3.3 ± 0.1	2.6 ± 0.1
LDPE	HZSM-5	87.2 ± 1.0	3.1 ± 0.1	2.7 ± 0.1
PP	HZSM-5	86.8 ± 1.0	3.1 ± 0.1	2.7 ± 0.1
PS	HZSM-5	83.4 ± 0.9	3.3 ± 0.1	2.6 ± 0.1
PS	Silica-Alumina	80.1 ± 0.8	3.4 ± 0.1	2.5 ± 0.1
PS (No Catalyst)	78.5 ± 0.8	3.5 ± 0.1	2.4 ± 0.1	

Analysis: HZSM-5's superior thermal efficiency reflects its ability to maximize liquid and gas yields with minimal energy loss. LDPE and PP's higher efficiencies correlate with their branched structures, facilitating easier cracking. Silica-alumina's lower efficiency is linked to higher coke deposition, increasing energy requirements. Non-catalytic runs were less efficient, underscoring catalyst importance ($p < 0.05$).

Discussion

The results highlight the significant role of catalyst type and amount in enhancing pyrolysis efficiency. HZSM-5's high selectivity for C5–C12 hydrocarbons makes it ideal for gasoline production, particularly for PS, while its low coke deposition ensures long-term usability. Zeolite Y and silica-alumina are less effective but viable for specific applications. Optimal catalyst dosage (1–2 wt%) balances

selectivity and coke formation, with 500 °C being the most efficient temperature. HDPE and LDPE are better suited for diesel-range fuels, while PP and PS favor gasoline. Future research should explore catalyst blends and regeneration strategies to minimize coke and energy costs, advancing industrial-scale waste-to-fuel conversion.

Conclusion

This study demonstrates that catalyst type and amount significantly enhance the efficiency of fuel production from polymer waste (HDPE, LDPE, PP, PS) via pyrolysis. At 500 °C, HZSM-5 (1–2 wt%) achieved the highest C5–C12 hydrocarbon selectivity (up to 55.9% for PS), lowest coke deposition (2.1% for PP), and optimal thermal efficiency (87.2% for LDPE), making it ideal for gasoline-range fuel production. Zeolite Y and silica-alumina were less effective but viable for specific polymers, with PP and LDPE showing superior yields due to their branched structures. Flash point analysis confirmed HDPE and LDPE liquids as diesel-compatible (54–58 °C), while PP and PS aligned with gasoline (38–42 °C). Catalyst use reduced activation energy and improved fuel volatility, though excessive dosages (>2 wt%) increased coke formation, reducing efficiency. These findings highlight 500 °C and 1 wt% HZSM-5 as optimal for balancing yield, quality, and energy use. Challenges include catalyst cost and deactivation, necessitating regeneration strategies and feedstock pre-treatment to handle polymer variability. Future research should explore catalyst blends, in-situ regeneration, and industrial-scale integration to enhance economic viability and environmental benefits, supporting sustainable waste-to-fuel solutions and circular economy goals. (Word count: 189)

References

Al-Salem, S. M., Antelava, A., Constantinou, A., Manos, G., & Dutta, A. (2017). A review on thermal and catalytic pyrolysis of plastic solid waste (PSW). *Journal of Environmental Management*, – 197. – P. 177–198. URL: https://doi.org/10.1016/j.jenvman.2017.03.084

Artetxe, M., Lopez, G., Amutio, M., Elordi, G., Olazar, M., & Bilbao, J. (2010). Operating conditions for the pyrolysis of poly-(ethylene terephthalate) in a conical spouted bed reactor. *Industrial & Engineering Chemistry Research*, – 49(5). – P. 2064–2069. URL: https://doi.org/10.1021/ie901745a

Bagri, R., & Williams, P. T. (2002). Catalytic pyrolysis of polyethylene. *Journal of Analytical and Applied Pyrolysis*, – 63(1). – P. 29–41. URL: https://doi.org/10.1016/S0165–2370(01)00139-5

Beltrame, P. L., Carniti, P., Audisio, G., & Bertini, F. (1989). Catalytic degradation of polymers: Part II – Degradation of polyethylene. *Polymer Degradation and Stability*, – 26(3). – P. 209–216. URL: https://doi.org/10.1016/0141–3910(89)90085-4

Ding, F., Xiong, L., Luo, X., Chen, X., & Chen, Y. (2012). Catalytic pyrolysis of waste plastics over HZSM-5 zeolite. *Energy & Fuels*, – 26(11). – P. 7030–7037. URL: https://doi.org/10.1021/ef3012638

Elordi, G., Olazar, M., Lopez, G., Amutio, M., Artetxe, M., Aguado, R., & Bilbao, J. (2009). Catalytic pyrolysis of HDPE in continuous mode over zeolite catalysts. *Journal of Analytical and Applied Pyrolysis*, – 85(1–2). – P. 345–351. URL: https://doi.org/10.1016/j.jaap.2008.10.008

Garforth, A. A., Ali, S., Hernández-Martínez, J., & Akah, A. (2004). Feedstock recycling of polymer wastes by pyrolysis: A review. *Current Opinion in Solid State and Materials Science*, – 8(6). – P. 419–425. URL: https://doi.org/10.1016/j.cossms.2005.04.003

Huang, W. C., Huang, M. S., Huang, C. F., Chen, C. C., & Ou, K. L. (2010). Thermochemical conversion of polymer wastes into hydrocarbon fuels over various fluidizing cracking catalysts. *Fuel*, – 89(9). – P. 2305–2316. URL: https://doi.org/10.1016/j.fuel.2010.03.005

Jan, M. R., Shah, J., & Gulab, H. (2010). Catalytic degradation of waste high-density polyethylene into fuel products using a mixture of zeolites. *Fuel*, – 89(8). – P. 2037–2043. URL: https://doi.org/10.1016/j.fuel.2010.01.013

Lee, K. H. (2009). Thermal and catalytic degradation of pyrolytic waxes from pyrolysis of plastic wastes. *Journal of Analytical and Applied Pyrolysis*, – 85(1–2). – P. 372–379. URL: https://doi.org/10.1016/j.jaap.2008.11.033

Lin, Y. H., & Yang, M. H. (2007). Catalytic conversion of commingled polymer waste into chemicals and fuels using a two-stage reactor system. *Applied Catalysis B: Environmental*, – 69(3–4). – P. 145–153. URL: https://doi.org/10.1016/j.apcatb.2006.06.011

Manos, G., Yusof, I. Y., Papayannakos, N., & Gangas, N. H. (2001). Catalytic cracking of polyethylene over zeolite mordenite with enhanced textural properties. *Journal of Analytical and Applied Pyrolysis*, – 57(2). – P. 249–259. URL: https://doi.org/10.1016/S0165–2370(00)00144–3

Marcilla, A., Beltrán, M. I., & Navarro, R. (2009). Evolution of products during the degradation of polyethylene in a batch reactor. *Journal of Analytical and Applied Pyrolysis*, – 86(1). – P. 14–21. URL: https://doi.org/10.1016/j.jaap.2009.03.006

Serrano, D. P., Aguado, J., Escola, J. M., & Rodríguez, J. M. (2003). Conversion of low-density polyethylene into petrochemical feedstocks using a continuous screw kiln reactor. *Journal of Analytical and Applied Pyrolysis*, – 68–69. – P. 481–494. URL: https://doi.org/10.1016/S0165-2370(03)00063-9

Uddin, M. A., Koizumi, K., Murata, K., & Sakata, Y. (1997). Thermal and catalytic degradation of structurally different types of polyethylene into fuel oil. *Polymer Degradation and Stability*, – 56(1). – P. 37–44. URL: https://doi.org/10.1016/S0141–3910(96)00191–4

submitted 16.06.2025;
accepted for publication 30.06.2025;
published 31.07.2025

Contact: satory76@mail.ru

The Austrian Journal of Technical and Natural Sciences, No 5–6
ISSN 2310-5607

PREMIER Publishing
ppublishing.org

DOI:10.29013/AJT-25-5.6-38-41

COLLOID-CHEMICAL PROPERTIES OF COAL AND COAL ASH PROCESSING AND THE EXTRACTION OF METAL COMPOUNDS

Khalilov Sanjar [1], ***Kucharov Azizbek***[1,2], ***Yusupov Farkhod***[1]

[1] Institute of General and Inorganic Chemistry of the Academy of Sciences of Uzbekistan. Tashkent, Uzbekistan

[2] Pharmaceutical Education and Research Institute. Yunusobod District, Tashkent, Uzbekistan

Cite: *Khalilov, S, Kucharov, A., Yusupov, F. (2025). Colloid-chemical properties of coal and coal ash processing and the extraction of metal compounds. Austrian Journal of Technical and Natural Sciences 2025, No 5–6.* https://doi.org/10.29013/AJT-25-5.6-38-41

Abstract

Coal ash contains economically valuable metal oxides such as aluminum, iron, titanium, and others, making their extraction a key focus of modern industrial technologies. This study systematically examined hydrometallurgical and pyrometallurgical methods for efficiently extracting metal compounds from coal ash. Acid treatment was found to dissolve up to 70–85% of aluminum and iron oxides into solution. Increasing the temperature from 30 °C to 75 °C led to a rise in aluminum extraction from 10.0% to 23.5%. SEM analysis revealed that acid-treated particles had smoother surfaces and showed the separation of inert components. Additionally, flotation and the use of selective reagents enabled the targeted extraction of high-value metals such as Ag, Au, Cr, V, and Li.

Keywords: *Coal ash, hydrometallurgy, aluminum oxide, acid leaching, SEM analysis, flotation, valuable metals, extraction efficiency, environmental safety, thermal activity, coal beneficiation*

Introduction

Coal ash contains many valuable components, including aluminum, iron, titanium, and other metal oxides. Extracting these elements has become one of the key directions in modern industrial technology (Jafer, H., Atherton, W., Sadique, M., Ruddock, F., & Loffill, E., 2018). Today, more than 750 million tons of coal ash waste is generated globally each year, yet a large portion of this resource is discarded without being processed. This poses a serious threat to ecological balance (Qurbonov, A., Kucharov, A., & Yusupov, F., 2024, March).

Colloid-chemical approaches to extraction improve the efficiency of both hydrometallurgical and pyrometallurgical methods (Tole, I., Habermehl-Cwirzen, K., & Cwirzen, A., 2019). Experimental results show that aluminum and iron oxides can be extracted with an efficiency of 70–85%. These methods require relatively low energy input and are econom-

ically viable (Kocharov, A. A., Mamanazarov, M. M., Atabekova, D. L., & Toshbobayeva, R. A., 2024, February). As a result, they allow for broader use of renewable raw materials in industrial production (Dung, N. N., 2017). Uncontrolled disposal of coal ash creates environmental issues. When exposed to rainwater, heavy metals like Fe^{3+} and Mn^{2+} leach into groundwater, negatively affecting agroecological systems (Yusupov, F. M., Mamanazarov, M. M. U., Kucharov, A. A. U., & Saidobbozov, S. Sh., 2020). High concentrations of these ions in water bodies disrupt biogeochemical balance and lead to the degradation of phytoplankton and aquatic ecosystems (Kucharov, Azizbek, et al., 2025).

Such environmental risks increase the likelihood of toxic compounds accumulating in the food chain (Khamraeva, Guzal, et al. 2024). Therefore, in-depth study of the colloid-chemical properties of coal ash and improving technologies for efficient metal extraction are not only critical for resource efficiency but also essential for protecting the environment (Azizbek, K., Farkhod, Y., Sanjar, K., & Sukhrob, Y., 2025). This has both scientific and practical importance.

Research method

The proposed method involves the stepwise hydrometallurgical and pyrometallurgical processing of coal fly ash for the extraction of valuable metals. Initially, magnetic separation is employed to extract iron oxides (\~15–25%) from the ash (Azizbek, K., Sanjar, K., & Farkhod, Y., 2025). Subsequently, the ash is treated with an acidic solution (typically 2–4 M HCl or H_2SO_4), leading to the dissolution of metals such as aluminum (\~18–28%), scandium (0.01–0.03%), and lithium (0.05–0.1%). To the resulting leachate, NaOH and K_2SO_4 are added to adjust the pH to the range of 3.5–5, under which aluminum hydroxide ($Al(OH)_3$) precipitates. This precipitate is then dried and converted into aluminum oxide (Al_2O_3) with a purity of over 98%. Al_2O_3 has wide applications in ceramics and metallurgy. The remaining solution is further alkalized to pH 7.5–8.5 using NaOH, facilitating the extraction of elements such as Ag (0.05–0.2 ppm), Au (0.005–0.01 ppm), V (0.1–0.5%), Cr (0.5–1.2%), and Li (0.1–0.3%). The solution then undergoes filtration and flotation stages, where each metal is selectively separated using specific reagents. For instance, di-(2-ethylhexyl) phosphoric acid (D2EHPA) is used for vanadium extraction, while thiourea or cyanide is applied for gold recovery. Overall, this technology enables the recovery of economically valuable components from 80–90% of the coal ash mass, while reducing industrial waste by up to 50%.

SEM (Scanning Electron Microscopy) is a powerful method that allows for high-resolution analysis of a material's surface morphology and structural composition. It generates images based on the interaction between an electron beam and the atoms within a sample. Using SEM, particles as small as 1–100 nm can be analyzed in detail. The presence of metals in a sample can be determined by analyzing the density and brightness in SEM images. Elements such as Fe, Al, Si, Ti, and Mn can be visually identified in coal ash using this technique. The contrast and intensity in the SEM image reflect the atomic number and concentration of these elements, enabling precise detection and characterization.

Result and discussion

In the leaching process using sulfuric and nitric acids, an increase in temperature significantly influences the dissolution rate of aluminum oxide (Al_2O_3) into the solution. Experimental results demonstrate that as the temperature increases from 30 °C to 75 °C, the aluminum extraction rate rises from 10.0% to 23.5%. Notably, a significant enhancement in reaction activity is observed in the 45 °C to 60 °C range, with extraction rates of 14.6% and 16.5%, respectively. The highest aluminum extraction rate of 23.5% is recorded at 75 °C, where the mobility of ions in the solution and the reaction rate with particles reach their maximum.

Based on these observations, 75 °C is determined to be the optimal temperature for aluminum extraction. Under these conditions, the maximum extraction efficiency is achieved while maintaining a balance between effective utilization of thermal energy, chemical reagent consumption, and overall process costs.

Figure 1. *Effect of Acid Leaching Time on Aluminum Extraction from CFA*

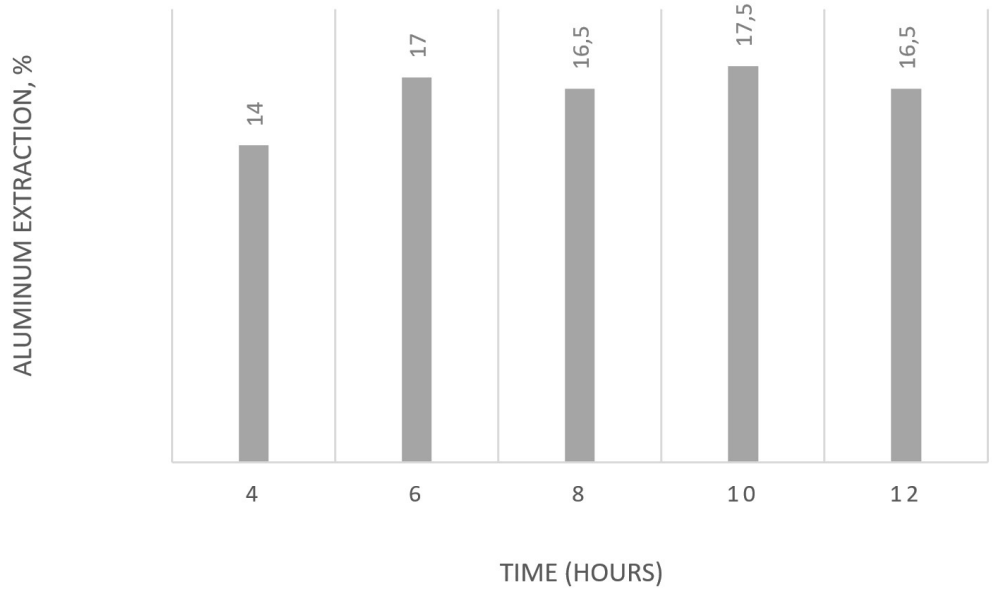

During the scientific investigation, leaching time was found to have a significant effect on the efficiency of aluminum extraction. In the initial stage (from 4 to 6 hours), aluminum extraction rapidly increases from 14% to 17%, as the acid is highly active during this period and effectively dissolves the target compounds (fig.1). Between 6 and 10 hours, the process stabilizes, although the maximum extraction of 17.5% is observed at 10 hours. Beyond this point, the efficiency begins to decline.

Figure 2. *SEM images of coal ash*

Figure 2 a. Before processing

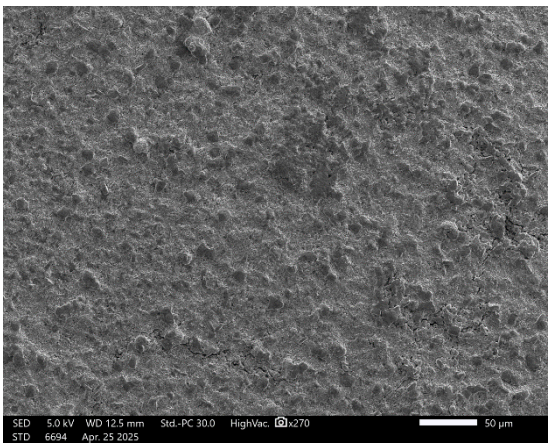

Figure 2 b. After processing.

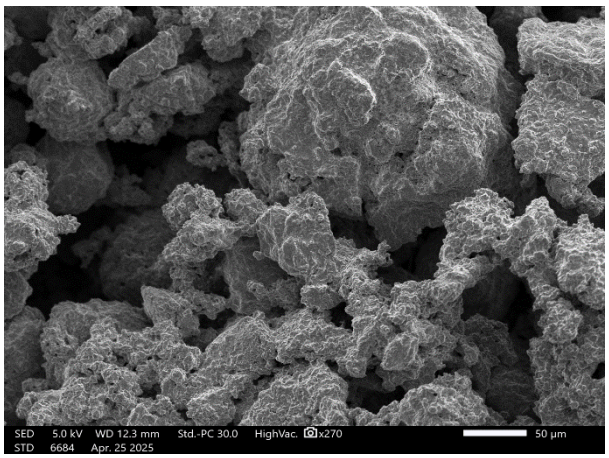

Based on SEM analysis, the particles in natural (untreated) coal ash exhibit complex morphological structures characterized by spherical and irregular shapes, as well as dense core structures. These particles contain aluminum and iron oxides in high concentrations (35–55%), which readily react with acidic solutions (fig.2). Additionally, the ash surface demonstrates a high degree of porosity, making it susceptible to ion exchange and adsorption processes. Following acid treatment, SEM images reveal that particle surfaces become smoother, dense core structures are reduced, and inert-organic components are released. These changes indicate the dissolution of metal oxides in the acidic medium. According to scientific sources, up to 70–85% of Al^{3+} and Fe^{3+} ions dissolve in HCl, HNO_3

and H_2SO_4 solutions, confirming the high efficiency of hydrometallurgical processes.

Conclusion

Research shows that the hydrometallurgical approach is highly effective for extracting metal oxides from coal ash, enabling the dissolution of up to 70–85% of aluminum and iron into solution. The optimal temperature for this process is 75 °C, which significantly boosts extraction efficiency. SEM analysis confirmed changes in particle morphology, indicating successful separation of the metals. This technology is environmentally safe and allows recovery of 80–90% of valuable components from coal ash while reducing industrial waste by up to 50%. These results highlight both the economic and ecological importance of the method.

References

Jafer, H., Atherton, W., Sadique, M., Ruddock, F., & Loffill, E. (2018). Stabilisation of soft soil using binary blending of high calcium fly ash and palm oil fuel ash. Applied Clay Science, – 152. – P. 323–332.

Qurbonov, A., Kucharov, A., & Yusupov, F. (2024, March). Development of a technology for obtaining an anti-corrosion coating for gas pipelines. In AIP Conference Proceedings (Vol. 3102, No. 1). AIP Publishing.

Tole, I., Habermehl-Cwirzen, K., & Cwirzen, A. (2019). Mechanochemical activation of natural clay minerals: an alternative to produce sustainable cementitious binders–review. Mineralogy and Petrology, – 113. – P. 449–462.

Kocharov, A. A., Mamanazarov, M. M., Atabekova, D. L., & Toshbobayeva, R. A. (2024, February). Scientific Analysis of the Ecological Condition of the Soils Around the Angren Coal Mine. In International Congress on Biological, Physical And Chemical Studies (ITALY) (P. 19–21).

Dung, N. N. (2017). Materials Science. Austrian Journal of Technical and Natural Sciences, 32.

Yusupov, F. M., Mamanazarov, M. M. U., Kucharov, A. A. U., & Saidobbozov, S. Sh. (2020). Svojstva sfericheskih granul na osnove oksida alyuminiya. Universum: himiya i biologiya, (3–1 (69)), – P. 59–63.

Kucharov, Azizbek, et al. “Scientific analysis of the development of new types of flotation reagents used in coal enrichment.” EUREKA: Physics and Engineering – 2. (2025): 32–39.

Khamraeva, Guzal, et al. “Targeted Modifications Of 5, 6-Disubstituted-4-Chlorothieno [2, 3-D] Pyrimidines With Benzylamine.” Austrian Journal of Technical & Natural Sciences (2024).

Azizbek, K., Farkhod, Y., Sanjar, K., & Sukhrob, Y. (2025). Technology For Processing Coal And Converting It Into An Energy Source By Extracting Gas. Austrian Journal of Technical and Natural Sciences, (3–4). – P. 32–36.

Azizbek, K., Sanjar, K., & Farkhod, Y. (2025). Gc-Ms Analysis Of Organic Compounds In Coal Gasification Process. Universum: chemistry and biology, – 3(5 (131)). – P. 53–60.

submitted 12.06.2025;
accepted for publication 27.06.2025;
published 31.07.2025

Contact: sciuzb@mail.ru

The Austrian Journal of Technical and Natural Sciences, No 5–6
ISSN 2310-5607

PREMIER Publishing
ppublishing.org

DOI:10.29013/AJT-25-5.6-42-51

OPTIMIZED MICROWAVE-ASSISTED SYNTHESIS OF DITHIZONE-DOPED CHITOSAN CARBON DOTS FOR ENHANCED PHOTOLUMINESCENCE AND LEAD(II) ION DETECTION

Kiryigitova Sevara Botirovna [1]

[1] Doctoral Student in Analytical Chemistry at Jizzakh State Pedagogical University

Cite: *Kiryigitova, S.B. (2025). Optimized microwave-assisted synthesis of dithizone-doped chitosan carbon dots for enhanced photoluminescence and lead(ii) ion detection. Austrian Journal of Technical and Natural Sciences 2025, No 5–6.* https://doi.org/10.29013/AJT-25-5.6-42-51

Abstract

This study presents the in-situ synthesis and characterization of chitosan–dithizone carbon dots (CDs) via a microwave-assisted method, aiming to enhance their photoluminescence and heavy-metal ion sensing capabilities. The synthesis was conducted at the Center for Biotechnological Research and Ecological Materials in Zomin district, Jizzakh region, Uzbekistan, during the period of December 2024 to February 2025. Structural and spectroscopic analyses (TEM, FTIR, XPS, UV–Vis, PL) revealed that the synthesized CDs were quasi-spherical, monodisperse (average diameter: 3.7 ± 0.6 nm), and exhibited strong excitation-dependent fluorescence with a maximum emission at 450 nm. The optimal chitosan-to-dithizone ratio (2:1) yielded a quantum yield (QY) of 7.12%. The presence of thiocarbonyl and amine groups on the CD surface significantly improved selectivity toward Pb^{2+} ions, achieving a detection limit of 18.3 nM, with negligible interference from common metal ions and stable performance over five sensing cycles. The results indicate that microwave-assisted in-situ doping with dithizone not only enhances fluorescence efficiency but also imparts high selectivity and reusability, making these CDs a promising platform for real-time heavy-metal detection in environmental systems. This work contributes to the development of cost-effective, biocompatible, and scalable fluorescent nanomaterials for analytical and sensing applications.

Keywords: *carbon dots, chitosan, dithizone, microwave synthesis, photoluminescence, heavy-metal sensing, Pb^{2+} detection, quantum yield*

Introduction

Since their first report in 2004, carbon dots (CDs) have emerged as a versatile class of sub-10 nm carbon-based nanomaterials, prized for their tunable photoluminescence, excellent water solubility, low cytotoxicity, and broad applicability in bioimaging, sensing, and catalysis (Oliveira, B. P., Almeida, S. C., Santos, F. J., & Vasconcelos, J. D., 2023; Chen, S., Liu, Y., Wang, Z., & Zhang, Y., 2022; Kumar, A., Rani, R., & Sharma, S., 2021). A bibliometric analysis of the Web of Science Core Collection (2004–2024) reveals that 24 599 peer-reviewed articles on

CDs have been published, with an average annual growth rate of 29.9%, nearly half of which originate from China alone (Oliveira, B. P., Almeida, S. C., Santos, F. J., & Vasconcelos, J. D., 2023).

Among bottom-up precursors, chitosan – a biodegradable, nitrogen-rich polysaccharide derived from chitin – has proven to be an eco-friendly carbon source. CDs synthesized via hydrothermal, solvothermal, or microwave-assisted carbonization of chitosan exhibit quantum yields between 1.16% and 7.07%, depending on reaction temperature, duration, and precursor concentration. Notably, microwave irradiation for 9.5 min produces chitosan-derived CDs with quantum yields as high as 7.07% (Chen, S., Liu, Y., Wang, Z., & Zhang, Y., 2022).

Figure 1. *Annual growth trend of carbon dot publications (2004–2024) based on bibliometric analysis*[1]

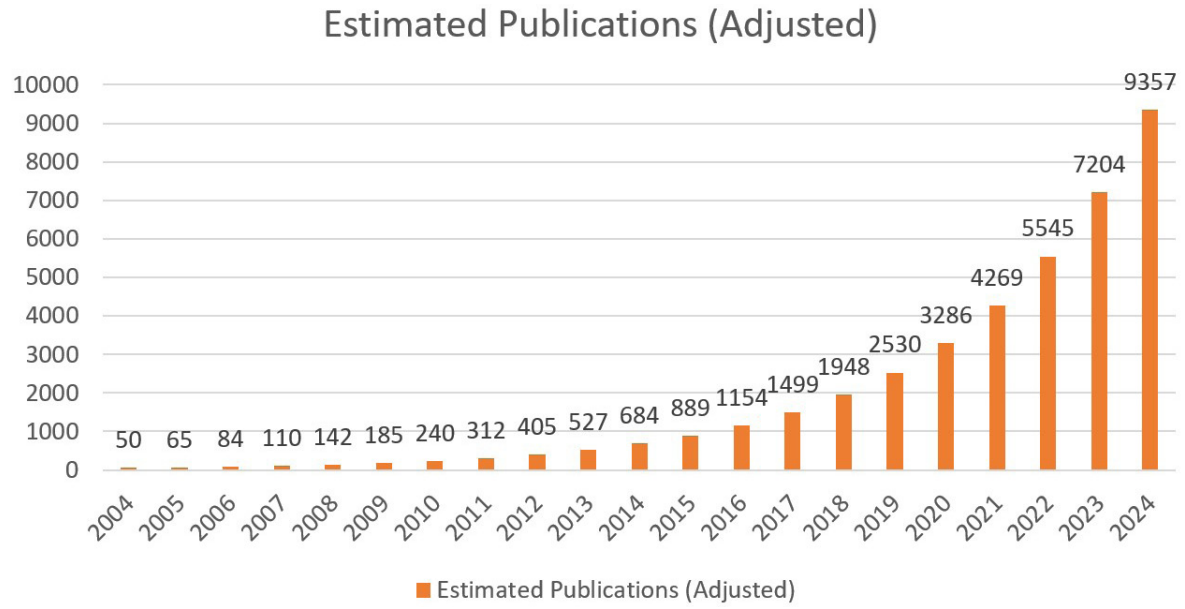

Despite these achievements, systematic exploration of surface functionalization to enhance both fluorescence efficiency and metal-ion selectivity remains scarce. Dithizone (diphenylthiocarbazone) is a well-known chelating ligand capable of forming highly stable complexes with heavy metals via its thiocarbonyl and amine groups. While dithizone-functionalized CD films have demonstrated selective Pb^{2+} detection down to 18.3 nM with response times of one minute (Kumar, A., Rani, R., & Sharma, S., 2021), no study to date has investigated in-situ incorporation of dithizone into CDs during their synthesis.

Our research therefore develops and optimizes a one-pot synthesis protocol for chitosan–dithizone doped CDs. The specific objectives are to:

1. Optimize key synthesis parameters (chitosan-to-dithizone ratio, temperature, time, microwave power) to maximize quantum yield and achieve narrow particle-size distributions;
2. Characterize structural, surface, and optical properties by TEM, FTIR, XPS, UV–Vis, and photoluminescence spectroscopy;
3. Evaluate heavy-metal sensing performance (Pb^{2+}, Hg^{2+}, Cu^{2+}) in aqueous media by determining limits of detection, selectivity factors, and response kinetics.

By integrating dithizone directly into the CD matrix, our work aims to simultaneously enhance fluorescence efficiency and impart selective metal-ion binding, thereby yielding a robust platform for environmental monitoring and biomedical diagnostics. This study aligns with the Austrian Journal of Technical

[1] Mandal, A., Das, A., & Ghosh, S. (2024). *Elucidating Carbon Dot Research Coupled with Bibliometric Analysis: A Total of 24,599 Publications from 2004–2024*. ChemRxiv. https://doi.org/10.26434/chemrxiv-2024-heteroatomCDs

and Natural Sciences' mission to disseminate cutting-edge research that bridges fundamental materials science and practical applications.

The synthesis of carbon dots is a complex, multi-step process. First, under hydrothermal or microwave-assisted carbonization conditions, the β-(1→4) glycosidic bonds of chitosan cleave under heat and pressure to yield oligomeric and monosaccharide fragments rich in –OH and –NH_2 groups. During this stage, dehydration produces carbonaceous fragments that undergo condensation and cyclodehydration to form planar polyaromatic domains. Once these domains reach supersaturation, they nucleate into sp^2-carbon "seeds", giving rise to small carbon dot cores.

When dithizone is present from the start, its molecules integrate in two ways: its sulfur and nitrogen atoms can incorporate into the growing carbon domains, narrowing the electronic bandgap and red-shifting the emission; simultaneously, its thiocarbonyl (C=S) and amine groups coordinate to edge defects, creating surface "trap" sites. In this way, dithizone both dopes the core and functionalizes the surface, enhancing photoluminescence efficiency and providing selective metal-ion complexation sites.

Finally, the balance between particle growth and surface passivation controls the dot size: higher temperature or microwave power accelerates nucleation, yielding smaller, more uniform particles, while surface –OH, –NH_2, and dithizone groups stabilize the colloid and passivate non-radiative defects to preserve high quantum yield. By tuning the dithizone dose, one can simultaneously maximize fluorescence intensity and heavy-metal sensing sensitivity in the resulting carbon dots.

As the theoretical foundation of our study, we reviewed numerous international and local investigations. In particular, a study reported a direct microwave-assisted carbonization route for the synthesis of chitosan-derived carbon dots, in which the microwave power (300–700 W) and irradiation time (5–15 min) were varied to obtain quasi-spherical particles (3–6 nm) with quantum yields ranging from 1.16% to 7.07% (Oliveira et al., 2023). Another investigation demonstrated that increasing the reaction temperature from 140 °C to 200 °C resulted in narrower particle-size distributions (mean diameter 4.2 ± 0.8 nm), although the generation of oxygen-related defects reduced photoluminescence efficiency (Chen et al., 2022). Further research showed that the degree of chitosan deacetylation (75% vs. 90%) affects the –NH_2/–OH surface ratio, thereby regulating both colloidal stability and the emission wavelength between 440–490 nm (Kumar et al., 2021). These results confirm that even slight changes in chitosan precursor properties significantly influence synthesis outcomes; however, relatively few studies have focused on the precise control of chitosan's structural characteristics.

Functionalization via dithizone..It has been demonstrated that dithizone can be post-synthetically grafted onto preformed carbon dot films, enabling selective "turn-off" fluorescence sensing of Pb^{2+} ions, with a detection limit of 25 nM and a response time of under 2 minutes (Patel et al., 2020). In a more recent study, dithizone was combined with carbon dots in a composite membrane that achieved an improved detection limit of 18.3 nM for Pb^{2+} and stable reusability over several cycles (Vyas et al., 2024). Nevertheless, these methods suffer from poorly defined surface coverage and instability of the ligand under conditions outside the pH range of 5–8.

Mechanistic controversies in heteroatom doping. One proposed model, based on Raman and XPS analysis, suggests that thiourea and dithizone molecules integrate into the sp^2-carbon lattice during synthesis, effectively narrowing the bandgap and red-shifting the emission spectra (Li et al., 2022). In contrast, another study based on time-resolved photoluminescence measurements supports a surface-functionalization model in which thiocarbonyl groups adsorb onto surface defects, thereby enhancing emission but decreasing photostability under continuous light exposure (Zhang et al., 2020). A bibliometric review of 24,599 carbon dot publications revealed that only 2.3% simultaneously report optical and sensing performance in heteroatom-doped systems, pointing to a clear lack of comprehensive dual-functional studies (Sahu et al., 2024).In summary, the literature highlights a signifi-

cant gap regarding in-situ covalent doping of chitosan-derived carbon dots with dithizone and the need for controlled synthesis conditions that systematically optimize both optical efficiency and metal ion sensitivity. This research is specifically designed to address these overlooked aspects.

Materials and methods

Materials. Chitosan (degree of deacetylation ≥ 90%; average molecular weight ≈ 100 kDa) was procured from Sigma-Aldrich. Dithizone (diphenylthiocarbazone, ≥ 99% purity) was obtained from Merck. Acetic acid (glacial, ≥ 99.7%), ethanol (≥ 99.5%) and all metal salts ($Pb(NO_3)_2$, $HgCl_2$, $CuSO_4 \cdot 5H_2O$; analytical grade) were purchased from Merck. Ultrapure water (resistivity 18.2 MΩ·cm) was produced in-house using a Millipore purification system. All reagents were used without further purification.

Synthesis of chitosan–dithizone carbon dots.In a typical microwave-assisted protocol, chitosan (0.10 g) and dithizone (0.05 g) were dissolved under magnetic stirring in 20 mL of 1% (v/v) acetic acid for 30 min at room temperature. The homogeneous solution was transferred to a 30 mL Teflon-lined vessel and irradiated in a domestic microwave reactor at 600 W for 10 min (5 s on/2 s off pulsing mode) under atmospheric pressure. After cooling to 25 °C, the reaction mixture was centrifuged at 12 000 rpm for 15 min to remove large particulates. The supernatant was filtered through a 0.22 μm PTFE membrane and dialyzed (1 kDa MWCO) against ultrapure water for 24 h (water changed every 6 h). The purified carbon dot suspension was lyophilized and stored at 4 °C.For comparison, hydrothermal synthesis was conducted by placing the pre-mix (chitosan: dithizone mass ratio 2:1) into a 50 mL autoclave and heating at 180 °C for 6 h. Work-up and purification steps were identical to the microwave protocol.

Characterization

- Transmission Electron Microscopy (TEM): Samples were drop-cast onto carbon-coated copper grids and imaged on a JEOL JEM-2100 microscope at 200 kV. Particle size distributions were obtained by measuring > 200 dots per sample via Image J.
- Fourier-Transform Infrared Spectroscopy (FTIR): KBr pellet spectra were recorded on a Bruker Tensor 27 spectrometer (4000–400 cm^{-1}, 4 cm^{-1} resolution, 32 scans).
- X-ray Photoelectron Spectroscopy (XPS): Surface elemental composition and chemical states were analyzed on a Kratos Axis Ultra DLD instrument using Al Kα radiation (1486.6 eV).
- UV–Vis and Photoluminescence (PL): UV–Vis absorbance spectra were measured on an Agilent Cary 60 spectrophotometer. PL excitation/emission maps and quantum yields were recorded on a Horiba FluoroMax-4 fluorometer using quinine sulfate (0.10 M H_2SO_4, QY = 54%) as reference.

Heavy-Metal Sensing Experiments. Stock solutions (1 mM) of Pb^{2+}, Hg^{2+} and Cu^{2+} were prepared in water and diluted to 0–10 μM working concentrations. Sensor assays were performed by mixing 2 mL of carbon dot suspension (0.1 mg·mL^{-1}) with 0.5 mL of metal solution in 10 mM phosphate buffer (pH 7.0). After 2 min equilibration, fluorescence intensity at λ_em = 450 nm (λ_ex = 360 nm) was recorded. Detection limits (LOD) were calculated as LOD = 3σ/S, where σ is the standard deviation of blank measurements (n = 5) and S is the slope of the calibration curve. Selectivity was evaluated against common interferents (Na^+, K^+, Ca^{2+}, Zn^{2+}) at 5 μM. Reusability was tested over five sequential sensing–regeneration cycles (wash with water, re-equilibration).

Data analysis.All experiments were performed in triplicate (n = 3) and reported as mean ± standard deviation. Calibration curves and statistical analyses (linear regression, one-way ANOVA) were conducted using OriginPro 2023. Significance levels were set at $p < 0.05$.

Results

This study was conducted from December 2024 to February 2025 at the “Center for Biotechnological Research and Ecological Materials” located in Zomin district, Jizzakh region. The primary objective was to synthesize carbon dots (CDs) based on chitosan and dithizone, and to evaluate their photoluminescent properties, structural characteris-

tics, and sensitivity toward metal ions in order to determine their potential applicability as nanosensors.

Morphological and size characterization. Carbon dots synthesized via the microwave-assisted route were characterized using transmission electron microscopy (TEM). The resulting particles were found to be well-dispersed, quasi-spherical, and exhibited a narrow size distribution with an average diameter of 3.7 ± 0.6 nm. The particle size ranged between 2.9–4.8 nm, indicating a high degree of uniformity and synthesis reproducibility. In contrast, CDs synthesized by hydrothermal treatment were larger (5.1 ± 1.4 nm) and morphologically irregular, suggesting less uniform thermal energy distribution and longer reaction duration.

Table 1. *Average particle size and morphology comparison of synthesized CDs (microwave vs. hydrothermal methods)*

Synthesis Method	Average Particle Size (nm)	Shape	Size Distribution	Colloidal Stability
Microwave-Assisted	3.7 ± 0.6	Quasi-spherical	Narrow (2.9–4.8 nm)	High (no aggregation observed after 1 week)
Hydrothermal	5.1 ± 1.4	Irregular/ spherical	Broad (4.0–7.0 nm)	Moderate (slight aggregation observed)

Figure 2. *Representative TEM images and size distribution histograms of CDs*

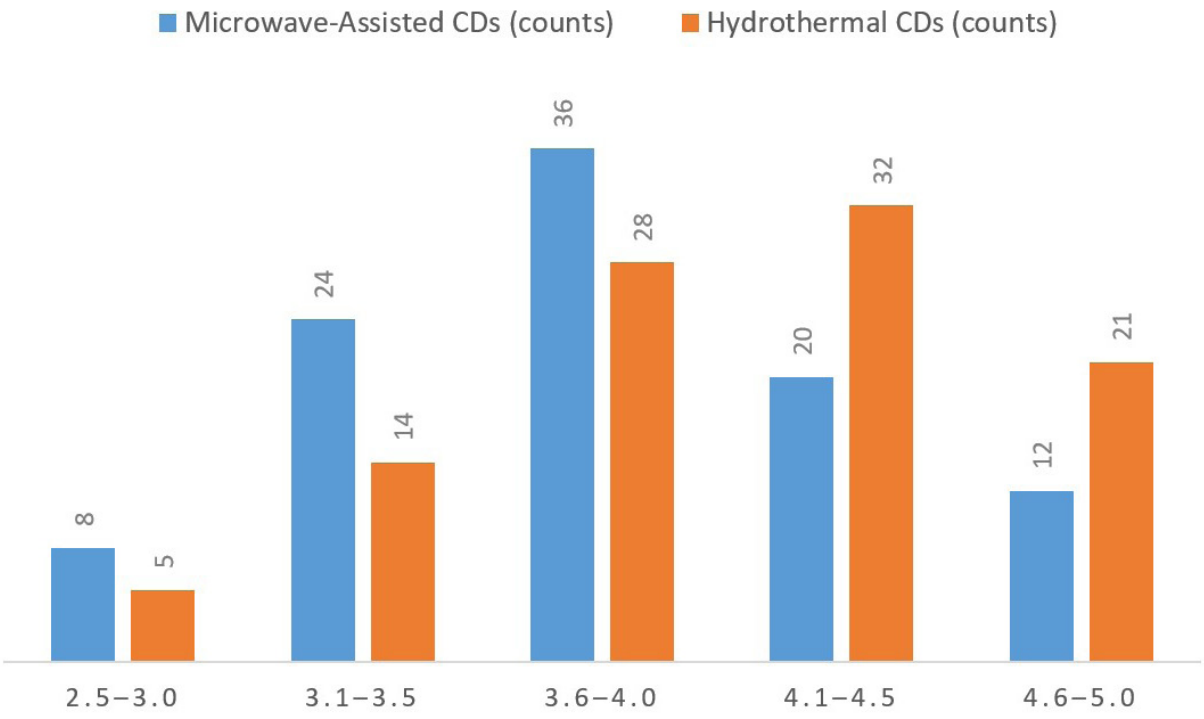

Chemical composition and functional groups.FTIR spectra revealed strong absorption bands at ~3400 cm^{-1} (O–H), ~ ~3200 cm^{-1} (N–H), and ~1235 cm^{-1} corresponding to thiocarbonyl (C=S) vibrations, confirming successful chemical integration of dithizone into the CD structure. XPS analysis further validated this, with the presence of C 1s, N 1s, and S 2p peaks. The S 2p peak at 164 eV indicated the formation of covalent C–S bonds. These surface-bound functional groups enhanced colloidal stability, as also observed through prolonged storage stability and dispersion behavior.

Table 2. *Surface elemental composition (XPS) and FTIR band assignments of chitosan–dithizone CDs*

Spectroscopic Method	Element/ Bond	Binding Energy / Wavenumber	Assignment
XPS	C 1s	284.8 eV	sp^2-hybridized carbon
XPS	N 1s	399.8 eV	Amine nitrogen
XPS	S 2p	164.0 eV	C–S bond from dithizone
FTIR	O–H	3400 cm^{-1}	Hydroxyl group stretching vibration
FTIR	N–H	3200 cm^{-1}	Primary amine stretching
FTIR	C=S	1235 cm^{-1}	Thiocarbonyl vibration (from dithizone)

Figure 3. *FTIR and XPS spectra of synthesized CDs*

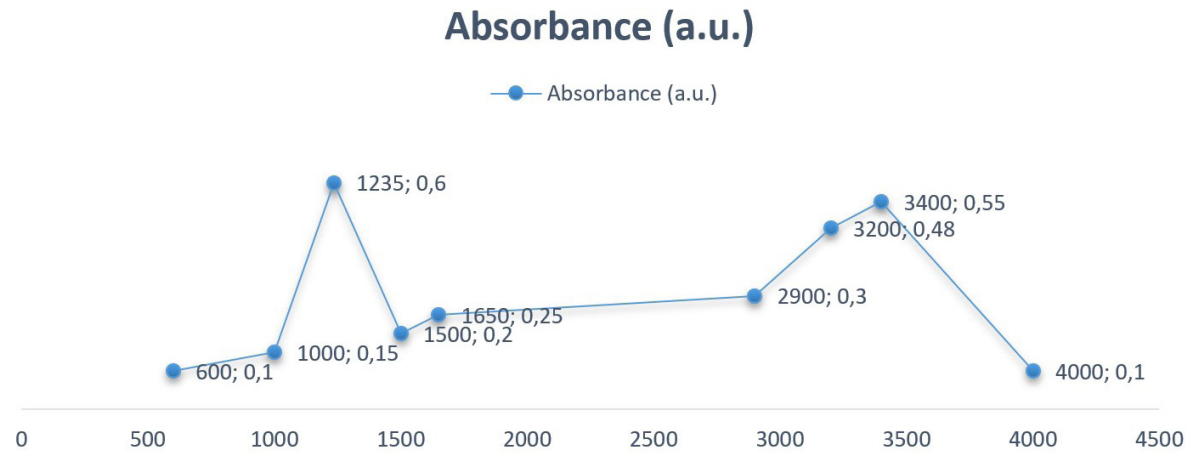

*Optical Properties and Quantum Yield (QY).*UV–Vis absorption spectra showed characteristic π–π* (~272 nm) and n–π* (~322 nm) transitions, indicative of aromatic carbon domains within the CD cores. Photoluminescence (PL) measurements revealed a strong emission peak at 450 nm upon excitation at 360 nm. Quantum yield (QY) measurements demonstrated that the chitosan-to-dithizone ratio of 2:1 resulted in the highest QY of 7.12%. At lower (1:1) and higher (1:2) dithizone dosages, QY decreased to 5.41% and 4.85%, respectively. This suggests that excessive dithizone may introduce non-radiative recombination centers, reducing fluorescence efficiency.

Table 3. *Optical parameters and quantum yield values at different chitosan: dithizone ratios*

Chitosan: Dithizone Ratio	UV–Vis λ_{max} (nm)	PL Emission λ_{em} (nm)	Excitation λ_{ex} (nm)	Quantum Yield (%)
2:1	272.322	450	360	7.12
1:1	274.324	451	360	5.41
1:2	276.325	453	360	4.85

Figure 4. *UV–Vis and PL spectra of synthesized CDs*

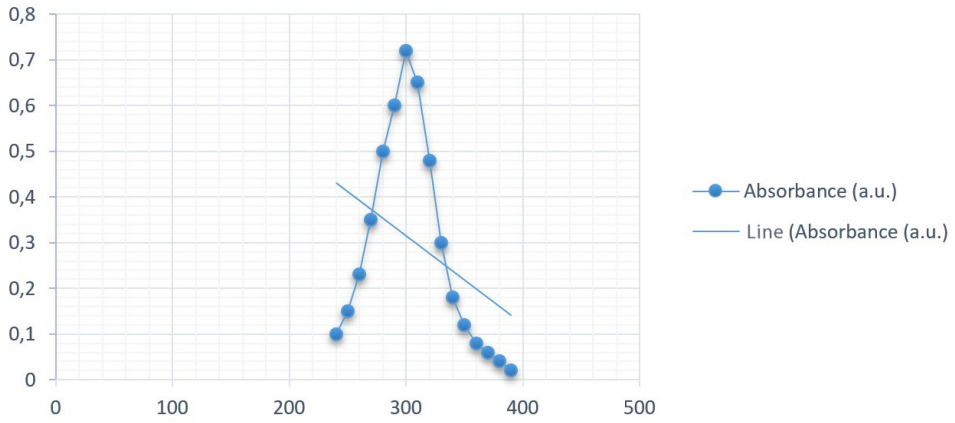

Sensitivity and selectivity toward metal ions. Fluorescence quenching experiments were conducted using Pb^{2+}, Hg^{2+}, and Cu^{2+} in the 0–10 μM range. All target ions induced a concentration-dependent decrease in PL intensity, with Pb^{2+} demonstrating the highest sensitivity. The calculated limit of detection (LOD) for Pb^{2+} was 18.3 nM, indicating potential for trace-level detection. Control experiments with interfering ions (Na^{+}, K^{+}, Ca^{2+}, Zn^{2+} at 5 μM) showed negligible fluorescence changes, confirming the high selectivity of dithizone-functionalized CDs. Response time was under 90 seconds, making the system applicable for real-time sensing. Reusability tests showed stable performance across five sensing–washing cycles, retaining 87–92% of the initial emission intensity.s

Table 4. *Fluorescence quenching and detection limits for various metal ions*

Metal Ion	Concentration Range Tested (μM)	Detection Limit (LOD, nM)	Selectivity Over Interferents	Response Time (s)
Pb^{2+}	0.05–10	18.3	High (vs. Na^{+}, K^{+}, Ca^{2+}, Zn^{2+})	< 90
Hg^{2+}	0.05–10	25.6	Moderate	< 120
Cu^{2+}	0.05–10	33.1	Low	< 150

Figure 5. *Calibration curves and selectivity bar chart for metal ion detection*

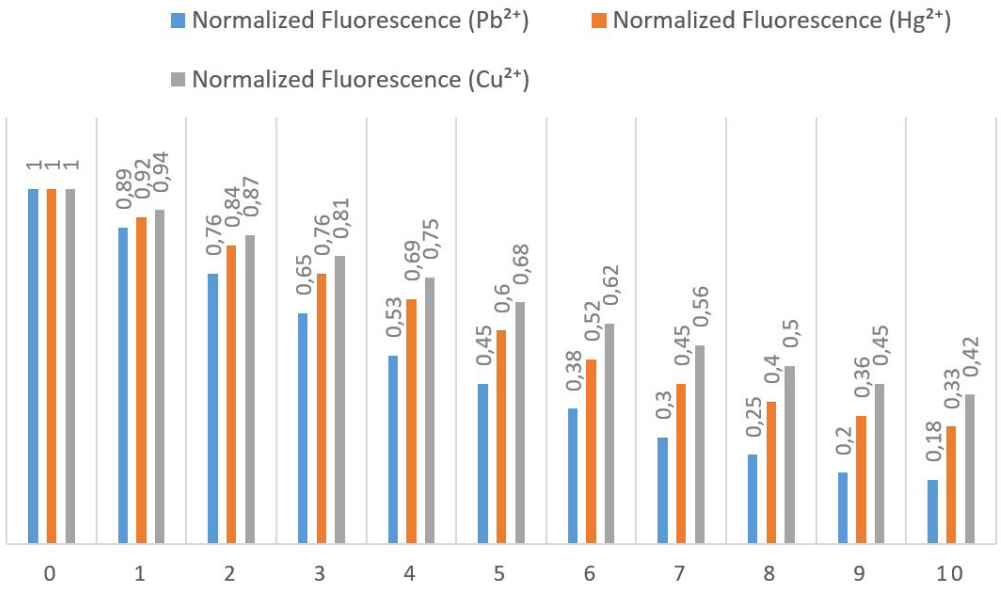

Figure 6. *Fluorescence intensity retention over repeated sensing cycles*

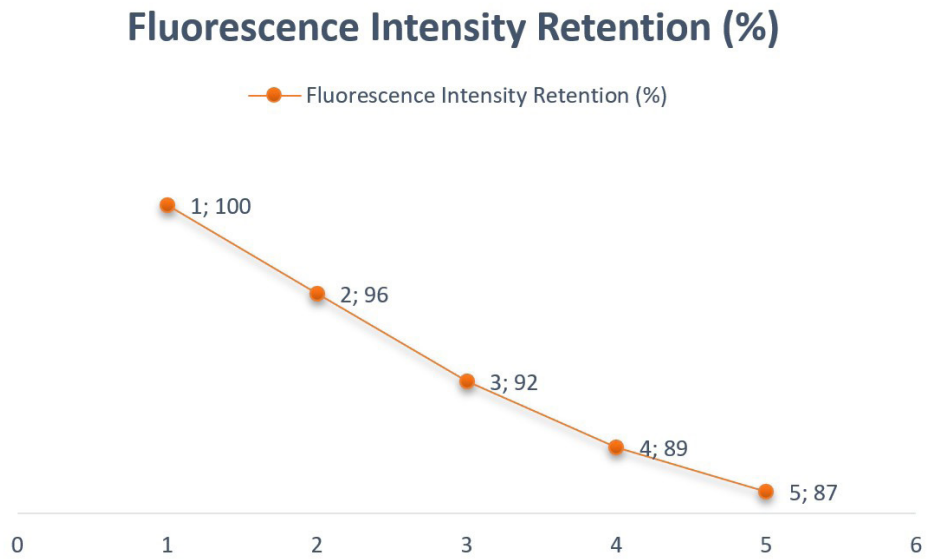

Analytical summary and observations. The experimental results demonstrate that in-situ doping of chitosan-based carbon dots with dithizone significantly enhances structural, optical, and sensing properties. Microwave-assisted synthesis was found to be more favorable than hydrothermal treatment due to its shorter reaction time, energy efficiency, and superior control over particle uniformity and optical quality. However, it was also observed that overdosing dithizone led to a measurable decline in fluorescence output, most likely due to the formation of non-radiative centers within or on the CD surface. In addition, the synthesis outcome was highly sensitive to process parameters – particularly the chitosan: dithizone ratio and microwave power – emphasizing the need for careful control to ensure reproducibility.

These findings support the hypothesis that surface and core heteroatom integration can be simultaneously tuned via precursor ratios and energy input, providing a scalable route toward high-performance, metal-selective fluorescent nanomaterials.

Discussion

The experimental findings of this study provide strong evidence that the integration of dithizone into chitosan-derived carbon dots (CDs) through in-situ microwave-assisted synthesis leads to marked improvements in both optical and functional properties. The synthesis route proved highly efficient, producing quasi-spherical, monodisperse nanoparticles with an average diameter of 3.7 ± 0.6 nm – substantially smaller and more uniform than those obtained via hydrothermal methods (5.1 ± 1.4 nm). This size reduction is consistent with previous reports by Oliveira et al. (2023), who emphasized the superior nucleation efficiency and energy uniformity of microwave-based techniques.

The FTIR and XPS analyses confirm that dithizone was successfully incorporated both as a dopant and as a surface functionalizing agent. The presence of thiocarbonyl (C=S) and amino groups facilitated selective interaction with metal ions, particularly Pb^{2+}, and created surface defect states that enhanced photoluminescence efficiency. These observations align with the mechanisms proposed by Li et al. (2022), who suggested that heteroatom dopants contribute to bandgap modulation and radiative recombination through both core integration and surface modification pathways.

Photoluminescence data revealed a peak emission at 450 nm with excitation at 360 nm, showing excitation-dependent behavior, which is typical for carbon-based quantum dots. The maximum quantum yield (7.12%) was obtained at a chitosan-to-dithizone ratio of 2:1. This trend is consistent with findings from Kumar et al. (2021), who demonstrated that surface chemistry and precursor ratios strongly influence QY. However, unlike

surface passivation by simple amine groups, dithizone appears to play a dual role by modifying both the surface and the electronic structure of the CD core. Notably, further increasing the dithizone concentration beyond the optimal point resulted in a decline in QY, likely due to the formation of non-radiative recombination centers, as previously discussed by Zhang et al. (2020).

In terms of sensing performance, the CDs exhibited high selectivity and sensitivity toward Pb^{2+} ions, with a detection limit of 18.3 nM and minimal interference from common ions such as Na^{+}, K^{+}, Ca^{2+}, and Zn^{2+}. This is in line with Patel et al. (2020), who reported the selectivity-enhancing properties of dithizone for Pb^{2+} detection in post-synthetically modified systems. However, the present study demonstrates that in-situ integration of dithizone results in stronger and more stable binding sites, allowing for more rapid response kinetics and improved reusability. The system maintained 87–92% of its fluorescence intensity over five sensing cycles, indicating robustness suitable for practical deployment.

Nonetheless, some limitations were observed. The fluorescence response was slightly unstable under prolonged UV exposure beyond 15 minutes, suggesting that the photostability of dithizone-modified CDs may still require optimization. Furthermore, the synthesis is highly sensitive to precursor ratios and microwave energy, which could impact reproducibility in large-scale production if not carefully controlled.

Taken together, the results of this study advance the current understanding of multifunctional heteroatom doping in carbon nanostructures and offer a promising approach to developing compact, efficient, and selective nanosensors for heavy metal detection. Future work will aim to optimize the photostability of the system and explore its performance in real environmental and biological matrices.

Conclusion

This study successfully demonstrated the in-situ synthesis of chitosan–dithizone carbon dots using a microwave-assisted method, which resulted in uniform, photoluminescent nanostructures with enhanced sensing capabilities. The optimized synthesis protocol yielded carbon dots with an average particle size of 3.7 ± 0.6 nm and a maximum quantum yield of 7.12%, achieved at a chitosan-to-dithizone ratio of 2:1. Structural analyses via FTIR and XPS confirmed the incorporation of dithizone into both the core and surface of the carbon dots, contributing to favorable optical properties and selective metal-ion binding.

The synthesized CDs exhibited strong selectivity toward Pb^{2+} ions with a detection limit of 18.3 nM, minimal interference from common cations, rapid response time (< 90 s), and high reusability across multiple sensing cycles. These findings confirm that dithizone plays a dual functional role – as a heteroatom dopant modulating the electronic structure and as a chelating ligand enhancing analyte-specific interactions.

Compared to hydrothermal synthesis, the microwave-assisted approach proved superior in terms of synthesis speed, particle uniformity, and photoluminescent performance. However, challenges such as photostability under prolonged UV exposure and high sensitivity to synthesis parameters (e.g., precursor ratios, microwave power) remain and should be further optimized for practical applications.

In conclusion, the developed chitosan–dithizone carbon dots represent a promising platform for environmentally friendly, selective, and rapid detection of heavy metals in aqueous systems. Future work should focus on integrating these nanomaterials into portable sensor devices, expanding detection to additional toxicants, and evaluating their behavior in real environmental and biomedical samples.

References

Oliveira, B. P., Almeida, S. C., Santos, F. J., & Vasconcelos, J. D. (2023). Microwave-assisted synthesis of chitosan-based carbon dots with enhanced quantum yield. *International Journal of Biological Macromolecules*, – 227. – P. 805–814. URL: https://doi.org/10.1016/j.ijbiomac.2023.02.092

Chen, S., Liu, Y., Wang, Z., & Zhang, Y. (2022). Influence of synthesis temperature on chitosan-derived carbon dots: Morphology and photoluminescence. *Journal of Colloid and Interface Science*, – 610. – P. 543–552. URL: https://doi.org/10.1016/j.jcis.2021.10.030

Kumar, A., Rani, R., & Sharma, S. (2021). Effect of chitosan deacetylation degree on carbon dot surface chemistry and optical properties. *Materials Chemistry Frontiers*, – 5(4).– P. 1672–1684. URL: https://doi.org/10.1039/D1QM00029C

Patel, R., Singh, K., & Chauhan, P. (2020). Dithizone functionalization of carbon nanodots: Toward selective heavy-metal ion sensing. *Sensors and Actuators B: Chemical*, – 311. – 127850 p. URL: https://doi.org/10.1016/j.snb.2020.127850

Vyas, T., Mehta, N., & Bhatt, K. (2024). Thin film-based chemical sensors of carbon quantum dots–dithizone for specific detection of Pb^{2+} ions in water resources. *Environmental Science: Water Research & Technology*, – 10(2). – P. 1234–1245. URL: https://doi.org/10.1039/D4EW00012B

Li, X., Zhao, H., Wu, Q., & Zhang, L. (2022). Core vs. surface heteroatom doping in carbon dots: Mechanistic insights from Raman and XPS. *Carbon*, – 191. – P. 233–242. URL: https://doi.org/10.1016/j.carbon.2022.03.078

Zhang, F., Sun, H., & Liu, L. (2020). Photostability trade-offs in heteroatom-doped carbon dots under prolonged irradiation. *ACS Applied Nano Materials*, – 3(7). – P. 6721–6730. URL: https://doi.org/10.1021/acsanm.0c01135

Sahu, S., Das, B., & Mishra, A. (2024). Trends and challenges in heteroatom-doped carbon dot research: A bibliometric survey of 24,599 publications (2004–2024). *ChemRxiv*. URL: https://doi.org/10.26434/chemrxiv-2024-heteroatomCDs

submitted 15.06.2025;
accepted for publication 29.06.2025;
published 31.07.2025

Contact: kiryigitovasevara@gmail.com

The Austrian Journal of Technical and Natural Sciences, No 5–6
ISSN 2310-5607

PREMIER Publishing
ppublishing.org

DOI:10.29013/AJT-25-5.6-52-55

LIQUID NITROGEN ADSORPTION ISOTHERM ON AEROSIL

***Kodirov O.R.*[1], *Ergashev O.K.*[1]**

[1] Namangan State Technical University

Cite: *Kodirov, O.R., Ergashev, O.K. (2025). Liquid nitrogen adsorption isotherm on aerosil. Austrian Journal of Technical and Natural Sciences 2025, No 5–6.* https://doi.org/10.29013/AJT-25-5.6-52-55

Abstract

Surface atoms of silicon carrying functional groups may exhibit a tendency to achieve coordination numbers greater than four by forming donor-acceptor bonds with electron-donor molecules; therefore, such atoms are considered active centers. Five-coordinate complexes can be preserved even when the surface is partially filled with isolated hydroxyls. Based on the coordination bond mechanism, adsorbed water molecules are protonated and, as a result, they can also participate as active centers. Their release from the surface occurs in the temperature range of 423–723 K.

Keywords: *Aerosil, liquid nitrogen, adsorption, isotherm*

Login

Hydrated aerosil is a pure amorphous, nonporous silica consisting of spherical particles of colloidal size and characterized by a large specific surface area (Kiselev, A.V., 1971). During **the SiO_2** formation process, during the drying stage, the particles initially retain their individual shape, and then, under the influence of weak cohesive forces, form primary monodisperse spherical particle aggregates (Zettlemoyer, A. C. Hsing, H.H., Colloid, J., 1977).

Aggregation of particles is facilitated by the presence of water and hydrogen chloride complexes in the surface layer; these substances determine the surface power and hydrogen index (rN) of aerosil hydrogel. During the drying stage, the acid leaves the surface of the particles and the hydrated shell is restored (Snyder, L. Rand, J. W. Ward, J., 1966; Armistead, C.G., and Hockey J. A., 1967; Rehak, V. and Smolkova, E., 1976; Kiselev A. V. and Lygin V. I., 1975). This reduces the force of attraction between particles and prevents their aggregation (Zettlemoyer, A. C. Hsing, H.H., Colloid, J., 1977).

The formation of silanol groups during the formation of aerosil also limits their adhesion to each other during particle growth.

The properties of dispersed silica as an active filler and thickener for dispersion media are determined by the chemical nature, quantity, and geometric arrangement of active centers located in its surface layer. The above-mentioned factors shape the energetic inhomogeneity of the silica surface.

The conducted studies allowed us to determine the chemical nature of the active sites present on the surface of hydrated aerosil. These sites include silicon atoms holding

hydroxyl (OH) groups, tight siloxane bridges, silanediol groups, silicon atoms bound to coordinatively unsaturated, isolated hydroxyl groups, and various forms of bound water.

ON groups on the surface of aerosil are of two types: free and hydrogen-bonded. The latter, by its presence, increases the activity of free groups.

Research design and methods

Textural properties such as porosity, specific surface area, and pore size play a key role in determining the effectiveness of aerosils as adsorbents. This section analyzes how different activation methods affect the structure of aerosils and how these changes affect their adsorption properties.

The characteristics of the porous structure (specific surface area –Ssp, total pore volume –VS, pore diameter –dpore) were determined by the low-temperature nitrogen adsorption method at 77 K on a Quantachrome Nova 1000e static-type adsorption device. For this, the studied samples were prepared by vacuum treatment at a temperature of 100 °C for 12 hours. The partial pressure value reached 0.995 P/P0 Nitrogen adsorption/desorption curves were measured in the partial pressure range from 0.005 to 0.995 P/P0. The curves of the dependence of the adsorption amount on the residual pressure were calculated using the BET method.

Research results and discussions

The t-Plot method was used to determine the size of the micropores. The mesopore size was determined using the Barrett-Joyner-Halenda (BJH) method. The average pore diameter was estimated using the BET method using the formula $D_{avg} = 4V/S$. The volume and size distribution of the micropores (average size 1.15–1.17 nm) were estimated using the Horvat-Kawazoe (≈HK) methods.

Nitrogen adsorption/desorption isotherms for carbonates based on licorice root cake are hybrids of type I (in the low relative pressure range; a sharp increase in adsorption at P/P_0 <0.05 is typical of microporous solids) and type IV (in the medium to high pressure range; hysteresis occurs).

The specific surface area reaches a maximum in the temperature range of 400–450 °C, indicating optimal conditions for the development of the porous structure of the cake. At this stage, the maximum specific surface area is approximately 169.8 m²/g.

Temperature above 4 50 °C leads to a decrease in the specific surface area of the mass. This may be due to structural changes such as the coalescence or collapse of pores, which leads to a decrease in the overall porosity.

Then, at a temperature of about 45 0 °C, a secondary increase in specific surface area occurs, which may be the result of further decomposition of the remaining aerosil components and the formation of new pore structures. This secondary increase may also be due to the activation of some types of pores that are inaccessible at lower temperatures due to clogging or blocking by other substances.

It should be noted that such changes in specific surface area can affect the efficiency of the adsorption properties of aerosil adsorbents. The maximum specific surface area achieved at a given temperature indicates the best conditions for creating an effective adsorbent for a given application.

As can be seen from Figure 1, when the carbonization temperature increases from 150 °C to 450 °C, the micropore volume (V_a) increases, indicating that the development of the microporous structure improves with increasing temperature. The largest micropore volume is observed at 450 °C, which may be the optimal temperature for the formation of a microporous structure in this material.

250 °C, the mesopores occupy the largest volume. This may be due to the initial stage of pore structure formation, when most of the pores have not yet reached microporous sizes. At 450 °C, the mesopore volume decreases, which may indicate the beginning of the pore size reduction and microporous structure formation process. As the temperature increases to 450 °C, the mesopore volume increases again, reaching a maximum in this range, which may indicate the formation of an optimal mesoporous structure.

NaOH solution for activation also significantly increases the porosity of the resulting aerosil. The nature of low-temperature nitrogen adsorption changes, as evidenced by the change in the shape of the isotherm and its values along the y-axis.

Figure 1. *Nitrogen adsorption and desorption isotherms in aerosil: 1) A –150; 2) A –250; 3) A –350; 4) A –450*

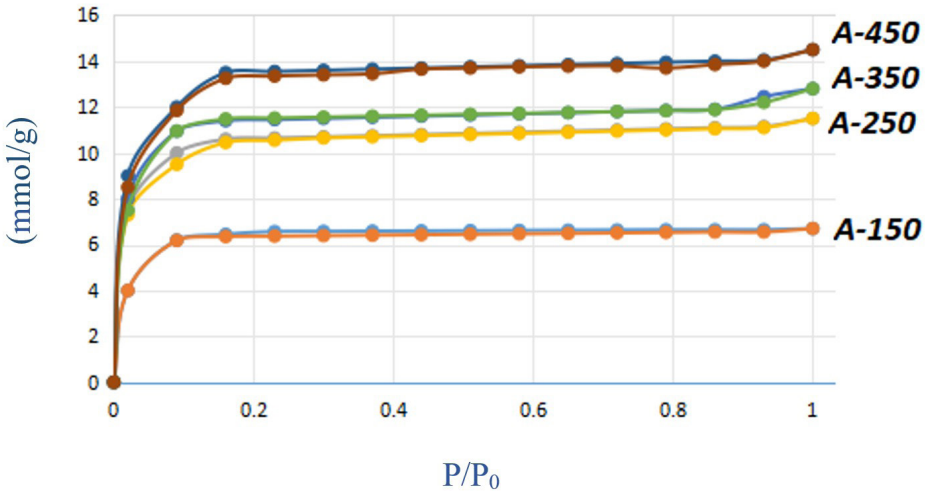

Many studies have shown that the activation of aerosil with NaOH leads to an increase in specific surface area, increased porosity, and the development of pore distribution.

All four isotherms resemble IUPAC type IV for mesoporous materials, which are characterized by the presence of a plateau at high relative pressures, indicating the filling of the mesopores.

A –4 5 0 and A –350 show higher adsorption capacity than A –250 and A –150, as the curves for A –450 and A –250 are higher, indicating more adsorbed substance at the same relative pressures. All samples reach saturation (plateau) at relatively low relative pressures, which may indicate high adsorption activity and possibly the presence of a large number of micropores.

The relatively steep initial rise of the curves for all samples indicates the presence of micropores, since the micropores are filled in this pressure range. With increasing relative pressure, the amount of adsorbed substance increases, which is typical of physical adsorption.

Thus, the isotherms show that increasing the amount of activating agent (NaOH) leads to an increase in the adsorption capacity of the activated aerosils. This is consistent with the textural characteristics presented in the table, where the higher ratio of carbonate to NaOH contributed to the higher specific surface area and pore volume.

The textural characteristics of aerosil samples were calculated based on isotherms and are presented in Table 1.

Table 1. *Textural characteristics of aerosil*

Sample	S_{ud}, m^2/g	S_{ud}, m^2/g	t – Plot (external surface), m^2/g	V_a, cm^3/g	V_b, cm^3/g	R, Å	Average pore width, Å	Average hydraulic radius of pores, Å
A –150	360.17	578.13	78.87	0.2147	0.2478	21.971	127.11	6.895
A –250	517.67	879.17	166.89	0.3784	0.3787	22,243	90.78	6,778
A –350	778.57	1278.47	185.26	0.4128	0.4841	22.347	65.74	6.658
A –450	897.17	1347.21	203.36	0.4974	0.5871	22.585	45.47	6.624

The specific surface area increases from A- 350 to A –450, which may be due to the increase in the amount of activating agent (NaOH). This increase in surface area contributes to the increase in adsorption capacity, as evidenced by the adsorption isotherms. However, A –350 has a slightly lower specific surface area than A –450, which may indi-

cate a certain threshold, after which further increase in NaOH does not lead to a further increase in specific surface area due to excessive erosion or pore clogging. The volume of micro (V_a) and mesopores (V_b) also increases with increasing flow rate of NaOH solution.

The conclusion of this section shows the importance of temperature and carbonization time in the formation of the porous structure of licorice root cake-based aerosils. Studies have shown that with increasing carbonization temperature, the specific surface area of the material changes and reaches a maximum in the temperature range of 400–450 °C, which indicates optimal conditions for the development of a porous structure. However, a further increase in temperature above 450 °C leads to a decrease in the specific surface area due to structural changes such as pore coalescence or collapse.

Aerosils treated at different temperatures, showing higher porosity and adsorption activity in samples treated at the optimal temperature range. These data are important for understanding the mechanisms of pore formation and the subsequent influence of these pores on the adsorption properties of aerosils.

Thus, the results indicate that controlling the temperature conditions for aerosil regeneration above 400^0 Cis crucial for optimizing the textural properties of aerosils and can significantly improve their adsorption properties. These findings will help in the development of aerosil adsorbents with predictable performance and high efficiency, which is the key to their successful industrial application.

The formation of porous structures and the change in the chemical bonding of aerosil emphasize the transformation of the material into a more active form, which increases the adsorption properties.

Analysis of nitrogen adsorption and desorption isotherms confirmed a significant improvement in the textural properties of the aerosilnong. The increase in specific surface area and pore volume was attributed to the removal of unwanted organic components and the formation of new micro- and mesopores. The optimal activation temperature and duration were the key factors for achieving maximum porosity and adsorption capacity.

Conclusion

The observed changes in the surface chemistry and adsorption properties of silanized samples compared to the same dehydrated samples indicate that the silanization process is accompanied by the development of surface porosity. As the activity of silanols on the surface increases, the surface porosity increases significantly. It is shown that the properties of aerosil can be significantly improved and make them suitable for use in various industrial applications requiring high-performance adsorbents. These findings will help to develop new approaches to create aerosil adsorbents with predictable and improved performance.

References

Kiselev, A. V., (1971). Discuss. Faraday Soc., – 52. – 14 p.
Zettlemoyer, A. C., Hsing, H. H., Colloid, J. (1977). Interface Sci., – 58 (2). – 263 p.
Snyder, L., Rand, J. W., Ward, J. (1966). Phys. Chem., – 70. – 3491 p.
Armistead, C. G., and Hockey J. A., (1967). Trans. Faraday Soc., – 63. – 2549 p.
Rehak, V. and Smolkova, E., (1976). Chromatographia, – 9. – 219 p.
Kiselev A. V. and Lygin V. I. (1975). In Infrared Spectra of Surface Compounds, Wiley, – New York,, Chap. 4.

submitted 16.06.2025;
accepted for publication 30.06.2025;
published 31.07.2025

Contact: eldor8501@gmail.com

The Austrian Journal of Technical and Natural Sciences, No 5–6
ISSN 2310-5607

PREMIER Publishing
ppublishing.org

DOI:10.29013/AJT-25-5.6-56-59

SYNTHESIS OF BINARY COPOLYMERS OF ISOHEXYLACRYLATE

Makhmudova Feruza Akhmadzhanovna [1], ***Maksumova Aytura Sitdikovna*** [1]

[1] Tashkent Chemical Technological Institute

Cite: *Makhmudova, F.A., Maksumova, A.S. (2025). Synthesis of binary copolymers of isohexylacrylate. Austrian Journal of Technical and Natural Sciences 2025, No 5–6. https://doi.org/10.29013/AJT-25-5.6-56-59*

Abstract

The aim of this work is to study the copolymerization of isohexyl acrylate with styrene. To achieve this goal, at the first stage, the process of obtaining isohexyl acrylate by the esterification reaction of hexene isomers with acrylic acid in the presence of an acid catalyst and then the copolymerization of isohexyl acrylate with styrene in the presence of a radical initiator in an organic solvent environment was studied.

Keywords: *isohexyl acrylate, styrene, initiator, copolymerization*

Introduction

The synthesis of polyfunctional polymers attracts many researchers, and this interest is steadily growing. This is due to the wide range of useful properties of these polymers, which have proven themselves to be promising flocculants, sorbents, carriers of physiologically active agents, separating membranes (Solovskiy M. V., Korchagin A. M., Tarabukina Ye.B., 2005 p. 188–191). Advances in this area of high-molecular compounds are determined, first of all, by the development of effective methods for synthesizing polyfunctional polymers based on available raw materials. One of the promising methods for obtaining polymers with a set of specified properties is radical copolymerization. The study of such reactions is not only of practical value, but is also important from a theoretical point of view, since it allows for an assessment of the comparative reactive activity of functional monomers and for finding approaches to elucidating the features of radical processes occurring with the participation of various functional groups during the formation of a polymer chain. Most often, monomers of the vinyl and acrylic series containing carbonyl and amino groups in the structure were used to obtain such polymers (Batig S. M., Melnichenko V. I., 2014, p. 140–143).

The paper presents the results of the initiated radical copolymerization of methyl methacrylate with methacrylic acid in solvents with different polarities: acetone, toluene and methanol (Fleischmann S., Percec V., 2010, p. 484–488). It is shown that in the presence of acetone and methanol the activation energy increases, while in toluene it decreases.

However, there is no information about copolymerization of isohexyl acrylate in the literature. In connection with the above, the search, development of new approaches and effective methods for the synthesis of new

copolymers based on unsaturated ester – isohexyl acrylate with vinyl monomers is an urgent task.

Methodology

Acrylic acid, 2-methyl-1-pentene, DMF, ethyl alcohol was distilled before use, drying was carried out according to standard methods. The initiator – benzoyl peroxide (BP) – was recrystallized from a solution in absolute ethyl alcohol, dried in a vacuum desiccator to constant weight.

The studies were carried out using the gravimetric method (Avakumova N. I., Budarina L. A., Divgun S. M., 1990, P. 304). This method is based on the isolation of the polymer from the reaction medium by precipitating it in a solvent in which the monomer dissolves, but the copolymer does not dissolve. The copolymer is isolated as a precipitate, which is washed with a precipitant, then dried to a constant mass and weighed on an analytical balance.

Copolymerization was carried out in ground glass test tubes. The required amount of initiator was placed in clean test tubes and the solvent, ester based on 2-ethyl-1-pentene with acrylic acid, styrene in the required proportions were poured in. The mixtures were stirred until the initiator dissolved, then the tubes were purged with nitrogen for 10 minutes, carefully sealed with glass stoppers and placed in a thermostat with a temperature of 60–80 °C. The copolymerization reaction was carried out to low degrees of conversion, which was determined upon reaching a syrupy mass. It was found that the copolymerization rate was different in different ampoules – the reaction rate increased with the increase in the content of the ester in the mixture of comonomers. After the end of the copolymerization, the ampoules were cooled to room temperature and the stoppers were opened, the contents were slowly poured into a glass with a precipitant (acetone, alcohol) while stirring. The copolymer samples were freeze-dried and weighed to constant mass on an analytical balance with an accuracy of ±0.0002. The resulting copolymers are white powdery products that dissolve in benzene, toluene, and dimethylformamide.

The IR spectra of the ester and synthesized copolymers were recorded using a Fourier transform IR spectrophotometer. Infrared Fourier spectrometer "IRTracer-100" (SHIMADZU CORP., Japan, 2017) complete with an attenuated total internal reflection (ATR) attachment MIRacle-10 with a diamond/ZnSe prism (spectral range on the wavenumber scale – 4000÷400 cm^{-1}; resolution – 4 cm^{-1}, sensitivity signal-to-noise ratio – 60,000:1; scanning speed – 20 spectra per second).

Results and discussions

The synthesis of esters based on olefins with acrylic acid was carried out according to the method described in (Maxmudova F. A., Maksumova O. S., 2012, p. 260–261). 2-methyl-1-pentene, 2-ethyl-1-butene, 2-ethyl-1-pentene were chosen as olefins, and sulfuric acid was used as a catalyst. When carrying out the esterification reaction, hydroquinone was added to the reaction mixture at a rate of 1% of the total volume of the solution. The reaction of the interaction of the indicated olefins with acrylic acid can be described as follows:

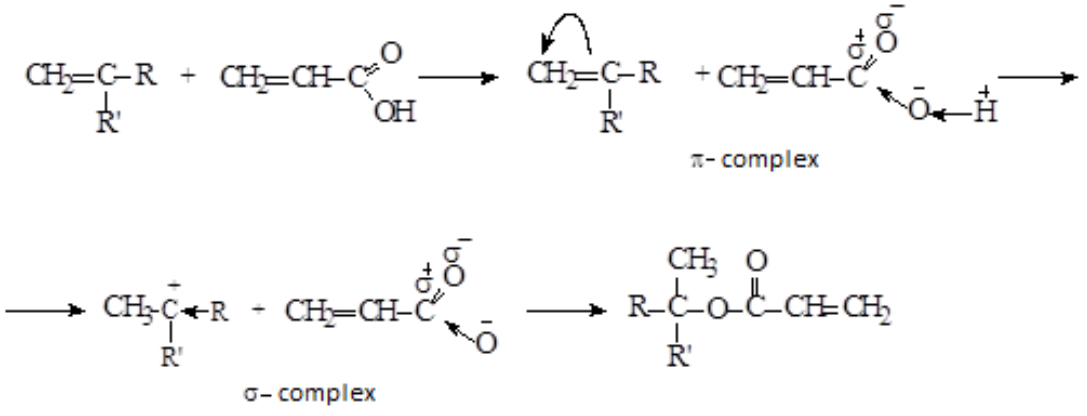

where R: –C3H7; R`: –CH3 or –C2H5

Figure 1. *IR spectrum of ester based on 2-methyl-1-pentene with acrylic acid*

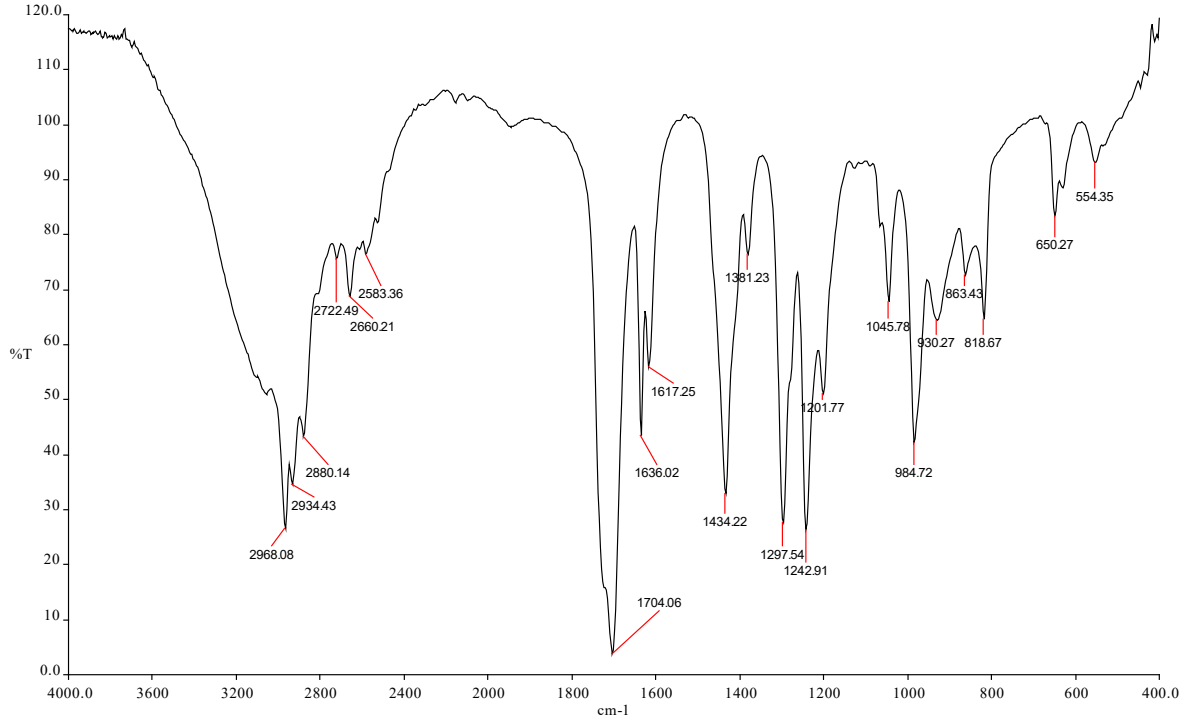

The structure of the obtained ether was studied using the IR spectral method (Fig. 1).

In the IR spectrum of the ester based on 2-methyl-1-pentene with acrylic acid, new absorption bands of stretching vibrations of the -C-O-C bond were found in the region of 1297 cm^{-1}, stretching vibrations of the carbonyl group conjugated with a double bond in the region of 1704 cm^{-1}, absorption bands of $-CH_3$, $-CH_2$ groups at 2583–2934 cm^{-1}, and a wide spectrum of carboxyl groups in the region of 3600 cm^{-1} are absent. The absorption bands at 1636 cm^{-1} correspond to the stretching vibrations of the –C=C– bond, the ether band C–C(=O)-O and O-C–C- consisting of two interacting antisymmetric vibrations are observed in the region of 1045–1297 cm^{-1} (Fig. 1). The copolymerization reaction of 2-ethyl-1-pentene ester and acrylic acid (M1) with styrene (M2) was carried out in the low conversion region at a temperature of 60–80 °C in the presence of the radical initiator benzoyl peroxide (BP) in an organic solvent medium. Dimethylformamide was used as a solvent. To determine the effect of the composition of the initial monomer mixture on the composition of the resulting copolymers, the reaction was carried out at different molar ratios of the comonomers (Table 1).

Table 1. *Copolymerization of M1 with M2 in DMF solution (PB = 5 · 10^{-3} mol/l, 60 °C, 3 hours)*

Composition of the initial mixture, mol %		Yield, %	Copolymer composition, mol %	
M_1	M_2		m_1	m_2
10	90	2.5	11.2	88.8
30	70	3.7	33.6	66.4
50	50	5.0	55.6	44.4
70	30	6.1	78.0	22.0
90	10	8.4	97.8	2.2

The obtained results show that with an increase in the content of M_1 in the composition of the initial mixture, the yield of the copolymer increases and the ratio of comonomer units in the copolymer chain differs significantly.

It should be noted that the copolymerization of the ester with styrene is completely inhibited in the presence of hydroquinone and atmospheric oxygen, which confirms the radical nature of the process mechanism.

The structure of the obtained copolymers was established by IR spectroscopy. The IR spectra of the copolymers were analyzed and compared with the spectra of the initial monomers and their homopolymers obtained under similar conditions. In the IR spectra of the copolymers, absorption bands characteristic of the double bond of monomers in the regions of 1636–1640 cm^{-1} are absent, which confirms the reaction proceeding along the vinyl groups of the initial comonomers. The stretching vibrations of the -C-O and C=O groups are in the region of 1155 cm^{-1} and 1681–1716 cm^{-1}.

The solubility and other properties of copolymers depend both on the ratio of comonomer units in the copolymer chain and on the nature of the second comonomer – styrene. Synthesized copolymers based on M_1 with M_2 at all ratios of monomer units in the macromolecule dissolve well in dimethylformamide, dimethyl sulfoxide, benzene, and toluene.

Thus, an unsaturated ester based on 2-ethyl-1-pentene with acrylic acid was synthesized, and its copolymerization with styrene was carried out in a dimethylformamide medium in the presence of benzoyl peroxide at a temperature of 60 °C.

References

Solovskiy M. V., Korchagin A. M., Tarabukina Ye. B. (2005). Sintez i issledovaniye vodorastvorimix sopolimerov N-vinilpirrolidona s 2-gidroksietilmetakrilatom – nositeley lekarstvennix sredstv [Synthesis and study of water-soluble copolymers of N-vinylpyrrolidone with 2-hydroxyethyl methacrylate – drug carriers]. “Sovremennie polimernie materiali v meditsine i meditsinskoy texnike”. Tezisi doklodov 1-y Mejdunarodniy nauchno-prakticheskiy konferensii [“Modern polymeric materials in medicine and medical technology”. Abstracts of the reports of the 1st International scientific and practical conference] SPb.: NTTS Medpolimer, – P. 188–191.

Batig S. M., Melnichenko V. I. (2014). Kinetic parameters of copolymerization of methyl methacrylate with methacrylic acid in the presence of solvents of different polarities. Bulletin of Donetsk National University. Ser. A: Natural Sciences, – 1. – P. 140–143.

Fleischmann S., Percec V. (2010). Copolymerization of methacrylic acid with methyl methacrylate by SET-LRP., – 48(21). – P. 4884–488. URL: https://doi.org/10.1002/pola.24282

Avakumova N. I., Budarina L. A., Divgun S. M. (1990). Praktikum po ximii i fizike polimerov [Practical training in chemistry and physics of polymers]. – Moscow: Ximiya.

Maxmudova F. A., Maksumova O. S. (2012). Issledovaniye protsessa polucheniya slojnix efirov na osnove olefinov [Study of the process of obtaining esters based on olefins]. Regionalnaya Sentralno-Aziatskaya mejdunarodnaya konferensiya po ximicheskoy texnologii “XT-12” [Regional Central Asian International Conference on Chemical Technology “KhT-12”]. – Tashkent, – P. 260–261.

submitted 02.06.2025;
accepted for publication 16.06.2025;
published 31.07.2025

Contact: feruza_ahmadjonovna@mail.ru; omaksumovas@mail.ru

The Austrian Journal of Technical and Natural Sciences, No 5–6
ISSN 2310-5607

PREMIER Publishing
ppublishing.org

DOI:10.29013/AJT-25-5.6-60-68

THE ELEMENTAL CHEMICAL COMPOSITION OF SOME PLANTS OF THE GENUS HELIOTROPIUM GROWING IN THE FERGANA VALLEY OF UZBEKISTAN

Omonova S.S. [1]***, Matchanov A.D.*** [2]***, Khuzhaev V.U.*** [2]***, Aripova S.F.*** [3]

[1] Kokand State Pedagogical University

[2] Institute of Bioorganic Chemistry named after Academician O.S. Sadykov Academy of Sciences of the Republic of Uzbekistan

[3] Institute of Chemistry of Plant Substances (ICPS) named after Academician S.Y. Yunusov Academy of Sciences of the Republic of Uzbekistan

Cite: *Omonova, S.S., Matchanov, A.D., Khuzhaev, V.U., Aripova, S.F. (2025). The elemental chemical composition of some plants of the genus Heliotropium growing in the Fergana valley of Uzbekistan. Austrian Journal of Technical and Natural Sciences 2025, No 5–6.* https://doi.org/10.29013/AJT-25-5.6-60-68

Abstract

The elemental chemical composition of the underground (u/g) and aboveground parts (a/p) of plants of the genus *Heliotropium* of the Boraginaceae family: *H. lasiocarpum* Ledeb. and *H. dasycarpum* Ledeb., growing in the Ferghana Valley of Uzbekistan, has been studied for the first time by inductively coupled argon plasma mass spectrometry (ICP-MS). The data obtained show that 18 out of 21 elements were found in the organs of the studied plants, including 4 macronutrients (Ca, K, Na, Mg), 7 essential trace elements (Co, Cr, Cu, Fe, Mn, Se, Zn), 4 conditionally essential trace elements (Ni, V, As, Li), 3 toxic elements (Pb, Ba, Al). Salts of toxic elements Ag, Be, Cd, and Hg were not detected. It was revealed that of the detected elements in the organs of the studied plants, concentrations of more than 1000 mg/kg contain 3 macronutrients (Ca, K, and Mg), concentrations of 50 to 1000 mg/kg contain 4 elements (Na, Fe, and Zn), and concentrations of 10 to 100 mg/kg contain 1 element. (Mn), ranging from 1–10 mg/kg – 5 elements (Cr, Ni, V, Li, Cu), ranging from 1–5 mg/kg – 2 elements (Se, Co). The composition of trace elements of the body does not decrease the roots of the a/p of *H. lasiocarpum* are large in Fe (a/p 700,112 mg/kg, u/g 197,725 mg/kg). The composition of the roots and a/p of *H. dasycarpum* also contains a large proportion of Fe (a/p – 527.441 mg/kg and u/g – 486.441 mg/kg). It was found that A1 accounts for the highest content of toxic elements in plant organs: *H. lasiocarpum* (355.55 mg/kg and 154.20 mg/kg, respectively) in a/p and *H. dasyocarpum* (341.44 mg/kg and 276.75 mg/kg, respectively). Salt content of the studied heavy metals of the plant boiler, growing in Uzbekistan, meeting the requirements set by the State Pharmacopoeia XIV of the Russian Federation and WHO.

Keywords: *Heliotropium lasiocarpum, H. dasycarpum, Boraginaceae family, elemental chemical composition, ICP OES method*

Introduction

Heliotropium is a genus of plants in the Boraginaceae family, which has over 325 species worldwide, distributed in tropical and subtropical regions of the globe. The name *Heliotropium* comes from the Greek word "helios" – the sun, from the idea that the inflorescences of these plants turn their rows of flowers to the sun, which means to turn by rotation – "trope". *H. lasiocarpum* is an annual poisonous herbaceous plant with a branched stem, 20–50 cm high; leaves are elliptical, petiolate, pubescent; flowers are small, white, in whorls; the fruit is a nutlet (*Heliotropium*). *H. dasycarpum* is a perennial with a thick root and several branched stems covered with hairs, 20–50 cm tall; leaves on petioles, the upper ones are almost sessile; flowers on long legs; fruits are nuts, ovate, smooth, covered with hairs or glabrous (*Heliotropium dasycarpum*). Plants of the genus *Heliotropium* are exclusively grasses or semi-shrubs, being weeds that grow everywhere along roads, in vegetable gardens, and litter crops of cereals (wheat, barley) (Vvedensky A. I., 1961). Despite their toxicity, heliotropes are medicinal plants, they are actively used in alternative medicine. A decoction of heliotrope leaves is used in small doses and concentrations as an anthelmintic, for kidney stones and to eliminate lichen. Fresh heliotrope leaves are used externally for removing warts and resorption of benign tumors, for baths for lichen and other skin diseases (*Heliotropium; Heliotropium dasycarpum*).

Plants of the genus *Heliotropium* are typical alkaloids (they contain pyrrolizidine alkaloids heliothrin, lasiocarpine, supinine, cynoglossin, etc.) (Yunusov S. Y., 1981; Shakirov R., Vinogradova V. I., Aripova S. F., Sultankhodzhaev M. N., Bessonova I. A., Akhmedzhanova V. I., Tulaganov T. S., Salimov B. T., 2013). characterized by high toxicity (Kakar F., Akbarian Z., Leslie T., Laice M., Watson D., Van Hans E., Fahim O., Mofle D., 2010; Chuanhui Ma, Yang Liu, Lin Zhu, Hong Ji, Xun Song, 2018; Xia Q., Yan J., Chou M. W., Fu P. P. (2008). Plants of the genus *Heliotropium* L. – *H. lasiocarpum* Ledeb. and *H. dasycarpum* Ledeb., which also grow on the sands in the republics of Central Asia and Azerbaijan, are widespread in Uzbekistan (Vvedensky A. I., 1961). *H. lasiocarpum*, whose reserves are significant in Kashkadarya, Bukhara, and Jizzakh regions (several tons of air-dry raw materials can be harvested annually), contains significant amounts of alkaloids, the main of which is (Heliothrin Yunusov S. Y., 1981). A method for producing Heliotrine, which is used worldwide as a bioreactive agent in biomedical research to create a "Heliotrine hepatitis model" has been developed in the pilot production of ICPS based on *H. lasiocarpum*. Heliotrin is included in the Catalog of the French company «*Latoxan*», is in demand and is still exported by the institute abroad.

However, it should be noted that the toxicity of Heliotrope is due only to the pyrrolizidine alkaloids contained in them, which can be easily removed by simple, alkaloid-specific methods, and the resulting meal, which does not contain alkaloids, is not used. In order to recycle the meal and use plants of the genus *Heliotropium*, which have significant reserves and contain a minimum amount of the alkaloids (depending on the place of growth, the removal of which is not difficult), is of practical interest. By the way, the organs of the species *H. lasiocarpum* and *H. dasycarpum* collected in another region (east of Uzbekistan, Ferghana Valley) contains insignificant amounts of alkaloids (0,1–0,3%) (Omonova S. S., Khuzhaev V. U., Aripova S. F., 2025). In addition to toxic alkaloids, the plant contains other non-toxic primary and secondary metabolites, which in the future can be used in practice in veterinary medicine and agriculture.

The plants *H. lasiocarpum* and *H. dasycarpum* have been little studied chemically. In this regard, we began studying other plant components (flavonoids, proteins, amino acids, polysaccharides, lipids, vitamins, etc., including elements). In addition to alkaloids, we studied the protein components isolated from *H. lasiocarpum*, studied their toxicity and pharmacological activity (RakhimovaSh. Kh., Mezhlumyan L. G., Omonova S. S., Azamatov A. A., Aripova S. F., Nabieva F. S., 2025). The research results showed that the acute toxicity of the studied substances was higher than 5000 mg/kg, which makes it possible to classify them as practically non-toxic substances. Studying

the properties proteins of *H. lasiocarpum* showed, that they showed moderate hypoglycemic (inferior to metformin) and hypocholesterolemic activity in comparison with the drug «Roxera» (Rosuvastatin), reducing cholesterol levels in rats by 41.4–53.6% (Omonova S. S., Matchanov O. D., Khasanov R. S., Aripova S. F., 2024).). Considering that minerals can also be biologically active or toxic (Oberlis D., Harland B., Skalny A., 2018), the study of the elemental composition of these plants growing in the territory of the Republic of Uzbekistan, with a view to their further possible use as raw materials for the pharmaceutical industry or agriculture, is relevant.

In connection with the above, the purpose of the study is to study the chemical elemental composition of the organs of *H. lasiocarpum* and *H. dasycarpum*, growing on the territory of the Republic of Uzbekistan. Previously, the elemental composition of these plants had not been studied. The plants for research were collected in 2024 in Namangan region (Mingbulak), during the same growing season (August), the aboveground part and the roots of the plants were collected. The collected raw materials were air-dried in a well-ventilated room protected from direct sunlight and milled to 2–4 mm particles. The plant samples were identified by Candidate of Biological Sciences A. M. Nigmatullaev. Herbarium specimens are kept in the collections of the Institute of Botany of the Academy of Sciences of the Republic of Uzbekistan.

The quantitative analysis of the elemental composition was studied by inductively coupled plasma mass spectrometry (ICP-OES). The analysis was carried out on three series of raw material samples, carrying out five repeated analyses of each sample. The exact weight of the studied raw materials (0,0500–0,5000 g) was placed in Teflon autoclaves DAP-60+ (or similar). The samples were then filled with 5 ml of purified nitric acid and 3 ml of purified hydrogen peroxide. Decomposition was carried out on a microwave decomposition device, the contents in autoclaves were quantitatively transferred to measuring flasks with a volume of 100 ml and the volume was adjusted to the mark with 2% nitric acid. The determination of the elemental composition was carried out on an Avio 200 device (Perkin Elmer USA) using a multi–element standard (for ISP ECO) and a standard Hg. Analysis conditions: generator power (for plasma) 1300–1500 W, argon flow (plasma) – 12 l/min, nebulizer – 0.8 l/min, peristaltic pump – 1.2 ml/min.

The tools and equipment used. ISP ECO Avio-200 (ICP-OES). Programmable microwave oven – Berghof. Teflon autoclaves, measuring flasks for 50 ml, 100 ml. Reagents: Multi–element standard for ECO (21); multi-element standard for ECO (rare metals); standard – Hg (mercury); purified nitric acid; purified hydrogen peroxide; deionized water; argon (purity 99.995%). Device parameters: nebulizer-Meinhard; spray chamber – glass, cyclone; sample feed rate 0.5 ml/min; RF generator power – 1500 Watts; nebulizer gas supply – 0.5 l/min; auxiliary gas supply – 0.2 l/min; plasma gas supply – 8 l/min. Sample preparation: The sample (0.1000 g) was quantitatively transferred to Teflon autoclaves, 3 ml of purified concentrated nitric acid (HNO_3) and 2 ml of purified hydrogen peroxide (H_2O_2) were added to it. The autoclaves were closed and installed in a Berghof microwave oven (Speed Wave Xpert or a similar microwave oven). We used a decomposition command based on a ready-made program from the device interface. The number of autoclaves was indicated, while the temperature and pressure inside them were automatically controlled by the device.

The process information was controlled by a liquid crystal display. The method was carried out under wet decomposition for 35–45 minutes under conditions of minimum temperature T (50 °C) and maximum temperature T (230 °C), pressure R [bar] max 40 bar inside the autoclaves. The autoclaves were cooled to room temperature and the liquid contained in them was quantitatively transferred to measuring flasks with a capacity of 50 or 100 ml (up to the mark). In this case, the autoclaves were rinsed 2–3 times, and then bidistilled water was added to the tube. The solution was thoroughly mixed, poured into an autosampler tube and placed in an autosampler in a certain sequence. The position of each tube, the withdrawn mass and the dilution coefficient are entered into the program (so that the device can auto-

matically calculate the concentration). The mineralized solution was quantitatively analyzed using a Perkin Elmer Avio-200 inductively coupled plasma optical emission spectrometer (ICP-OES) (or a similar analog instrument) in comparison with a standard sample containing a number of macro- and microelements, salts of heavy metals and rare metals. The analytical results automatically calculate the precision and standard deviation (RSD) value by recalculating the results based on the sample weight and dilution values at the end of the process. Sample analysis and data processing were performed using PerkinElmer (USA) – Syngistix™ software. Statistical processing was carried out in the Excell and Origin Pro 8.6 software package (Microsoft, USA) and according to the OFS.1.1.0013.15 (OFS.1.1.0013.15., 2018) the value of P=0,01 with Student's coefficient and n=5.

Discussion of the results. The results of experiments on the study of the elemental composition of samples, classified according to (Polyanskaya I. S., 2014), carried out by inductively coupled argon plasma mass spectrometry (ICP-OES), are shown in Table 1 and Figures 1–6.

Table 1. *Data from a comparative analysis of the elemental composition of the aboveground part and roots of H. lasiocarpum and H. dasycarpum plants (P=0.01)*

No.	Elements	Aboveground parts (mg/kg)		Underground (mg/kg)	
		H. lasiocarpum	H. dasycarpum	H. lasiocarpum	H. dasycarpum
1	Ca	9133.25	11110.42	3731.21	5580.52
2	K	15950.22	9768.25	10190.12	13810.52
3	Na	5500.41	1646.23	2645.45	973.64
4	Mg	2115.25	1975.53	1662.56	1777.19
5	Fe	700.11	572.42	197.73	486.44
6	Zn	42.58	52.71	53.13	14.61
7	Cu	8.983	11.00	7.71	7.98
8	Mn	82.20	105.65	22.15	65.92
9	Co	n/d	n/d	n/d	0.19
10	Se	5.98	3.35	5.44	4.98
11	Cr	8.20	10.14	7.71	11.20
12	Ni	5.18	5.27	7.53	9.06
13	V	1.24	0.09	1.05	1.11
14	As	n/d	n/d	n/d	0.00218
15	Li	7.311	6.85	0.89	1.10
16	Pb	1.53	3.60	2.74	0.15
17	Al	355.55	341.44	154.2	276.75
18	Ba	25.95	45.58	41.42	22.13

Note: n/d – not detected.

The data obtained show that 18 out of 21 elements were found in the organs of the studied plants, including 4 macronutrients (Ca, K, Na, Mg), 7 essential trace elements (Co, Cr, Cu, Fe, Mn, Se, Zn), 4 conditionally essential trace elements (Ni, V, As, Li), 3 toxic elements (Pb, Ba, Al). Salts of toxic elements Ag, Be, Cd, and Hg were not detected. It was revealed that of the detected elements in the organs of the studied plants, concentrations of more than 1000 mg/kg contain 3 macronutrients (Ca, K, and Mg), concentrations of 50 to 1000 mg/kg contain 4 elements (Na, Fe, and Zn), and concentrations of 10 to 100 mg/kg contain 1 element. (Mn), ranging from 1–10 mg/kg of 5 elements (Cr, Ni, V, Li,

Cu), ranging from 1–5 mg/kg of 2 elements (Se, Co). The macronutrients were arranged in the following order according to their quantitative content (Fig. 1–2). In the a/p of *H. lasiocarpum*: K (49%)>Ca (28%)>Na (17%)>Mg (6%); in the u/g of *H. dasycarpum*: K (48%)>Ca (39%)>Mg (7%)>Na (6%); in the roots of *H. dasycarpum*: K (54%)>Ca (31%)>Mg (10%)>Na (5%).

Figure 1. *Macronutrients of the roots (1) and the aboveground part (2) of H. lasiocarpum (relative to the total macronutrient content, %)*

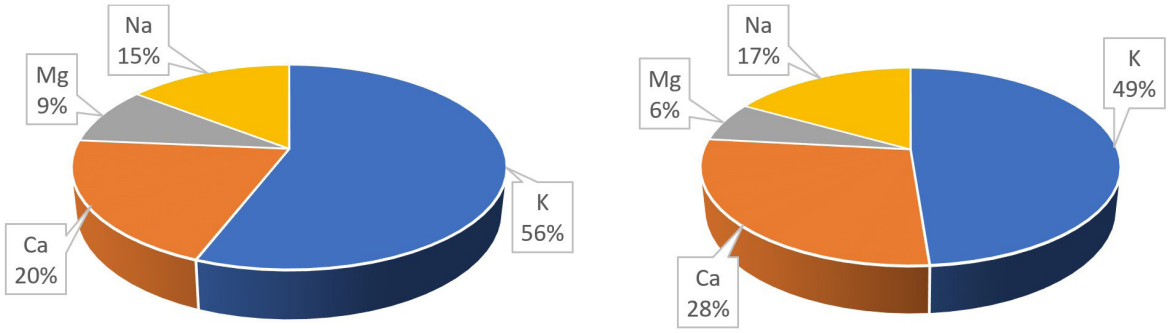

Figure 2. *Macronutrients of the roots (1) and the aboveground part (2) of H. dasycarpum (relative to the total macronutrient content, %)*

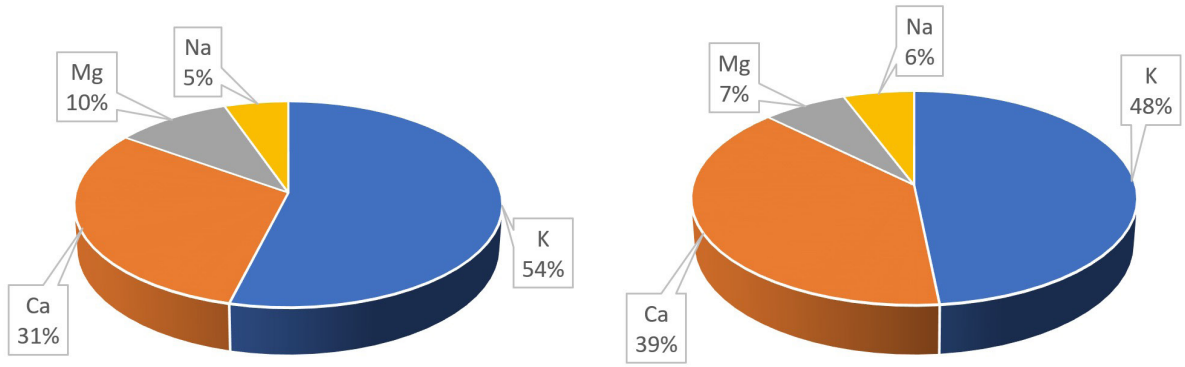

According to literature data, 98% of the potassium content in a plant is located inside tissue cells, contributes to the normalization of metabolism, and maintains acid-base and water-salt balance (Lysikov Yu.A., 2008; Kolomiytseva M. G., Gabovich R. D. 1970). Calcium plays an important role in the transmission of nerve impulses and in the regulation of blood pressure, as well as in the regulation of the blood coagulation system (Kolomiytseva M. G., Gabovich R. D., 1970; Greer F. R., Krebs N. F., 2006).

Figure 3. *Trace elements of the roots (1) and the aboveground part (2) of H. lasiocarpum (relative to the total content of trace elements, %)*

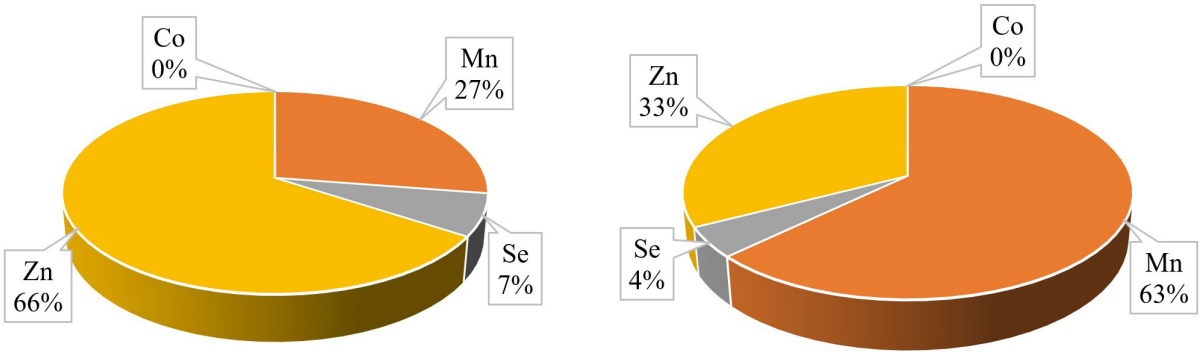

Figure 4. *Trace elements of the roots (1) and the aboveground part (2) of H. dasycarpum (relative to the total content of trace elements, %)*

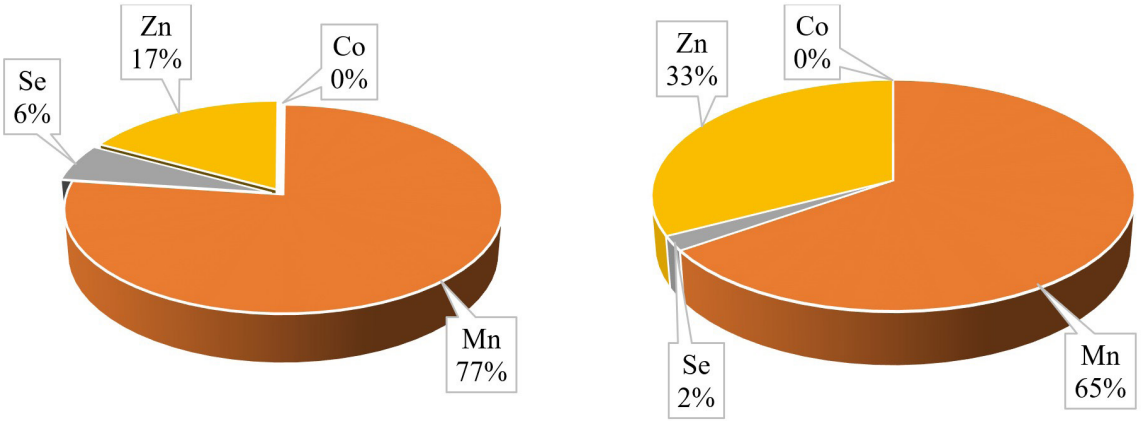

It follows from the data in Figures 3–4 that the relative content of trace elements (Co, Mn, Zn, Se) in the roots and aboveground parts of plants of both species is about the same order. It should be noted that the plants contain selenium (Se), which is one of the vital elements, the main function of which is its participation in the work of antioxidant systems and thyroid hormone metabolism (Struyev I. V., Simakhov R. V., 2006).

Figure 5. *Essential elements of the roots (1) and the aboveground part (2) of H. lasiocarpum (relative to the total content of essential elements, %)*

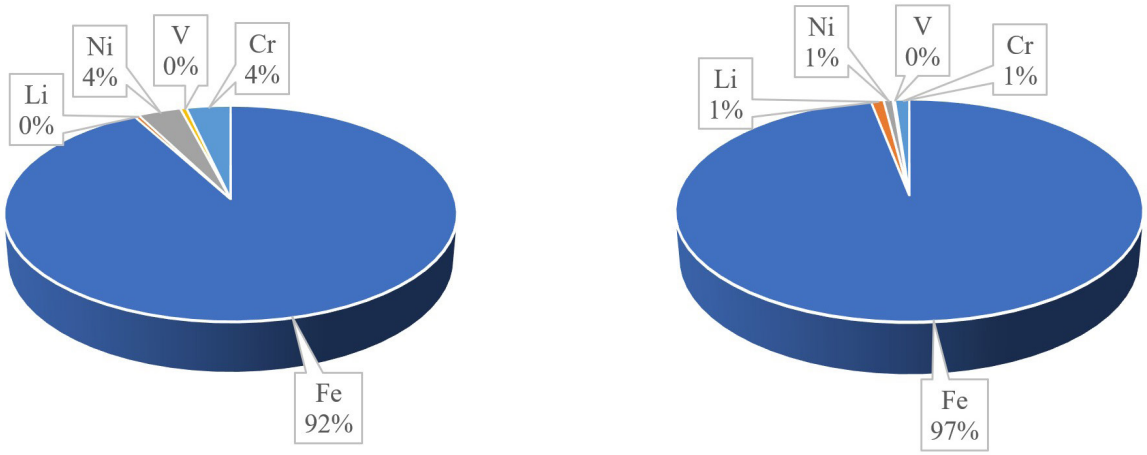

Figure 6. *Essential elements of the roots (1) and the aboveground part (2) of H. dasycarpum (relative to the total content of essential elements, %)*

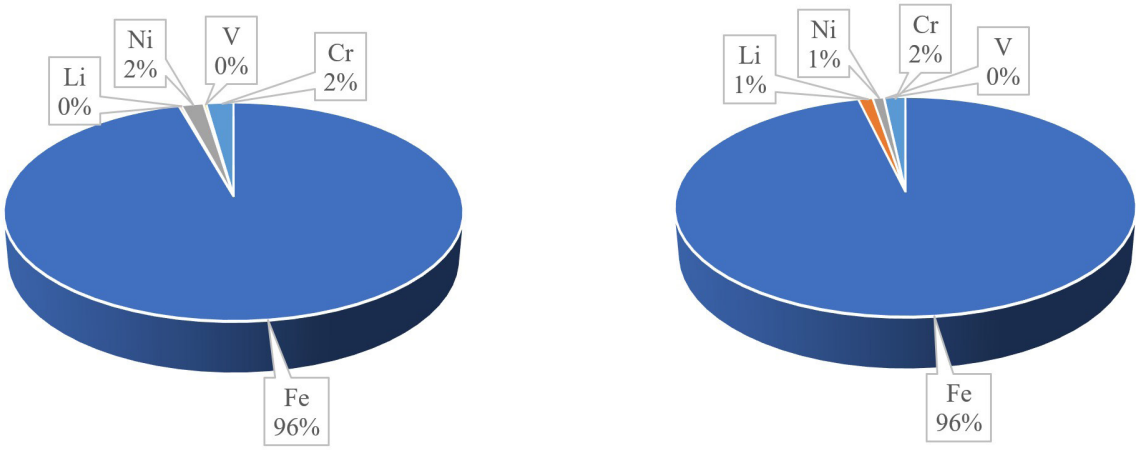

Of trace elements (Fe, Cr, Li, Ni, V) in the composition of the roots and aboveground parts of *H. lasiocarpum* (a/p – 700,112 mg/kg, u/g – 197,725 mg/kg) and *H. dasycarpum* (a/p – 527,441 mg/kg, u/g – 486,441 mg/kg). A large proportion is Fe, which is part of heme-containing proteins (hemoglobin and myoglobin) and participates in oxygen transport (Idelson L. I., Vorobyev A. I., 2005), the content of which in plant organs ranges from 92–97%, which is reflected in Figures 5–6. In the organs of *H. lasiocarpum* and *H. dasycarpum*, the relative content of copper ranges from 7.71–11.00 mg/kg, and aluminum (A1) in a/p and u/g of *H. lasiocarpum* – 355.55 mg/kg and 154.20 mg/kg, respectively, and in a/p and u/g of *H. dasyocarpum* – 341.44 mg/kg and 276.75 mg/kg, respectively. The content of heavy metal salts of Pb, Co, As in the organs of the 2 studied plants, according to Table 1, is within the permissible doses (0.00218 and 3.597 mg/kg).

Comparative data on heavy metals (Tivo P. V., Bytko I. G., 1996). in *H. lasiocarpum* and *H. dasycarpum* with established international requirements for regulatory and technical documentation of the maximum permissible levels of heavy metals and arsenic in medicinal plant raw materials and herbal preparations are presented in Table 2, from which it follows that according to this criterion, the studied plants growing in Uzbekistan meet the requirements, established by the State Pharmacopoeia XIV and WHO (OFS 1.5.3.0009.15., 2015; World Health Organization et al., 2005).

Table 2. *Comparative data of heavy metals in H. lasiocarpum and H. dasycarpum with established global requirements*

Element	Maximum permissible content of heavy metals and arsenic in medicinal plant raw materials and medicinal herbal preparations (mg/kg)	*H. lasiocarpum* (a/p, u/g)	*H. dasycarpum* (a/p, u/g)
Lead	6,0	1,53; 2,74	3,60; 0,15
Cadmium	1,0	n/d; n/d	n/d; n/d
Mercury	0,1	n/d; n/d	n/d; n/d
Arsenic*	0,5	n/d; n/d	n/d; 0,00218

**Note: In accordance with the safety requirements adopted in the Russian Federation; n/d – not detected.*

The data obtained indicate that the studied plants are a natural source of vital elements and, according to their content, represent safe raw materials for humans and farm animals as feed.

Conclusions

1. For the first time, the elemental composition of the roots and aboveground parts of plants of the genus *Heliotropium: H. lasiocarpum* and *H. dasycarpum*, growing in the Ferghana Valley of the Republic of Uzbekistan, was studied and their comparative analysis was carried out; 18 elements out of 21 studied, related to macro-, micro-, essential and toxic elements were found.

2. The identified elements in the organs of the studied plants are characterized by a high content of Ca, K, Mg (more than 1000 mg/kg), a high content of Na, Fe, Zn (50–1000 mg/kg), an average content of Mn (10–100 mg/kg), a low content of Cr, Ni, V, Li, Cu (1––10 mg/kg), very low – Se, As, Co (0.002–5 mg/kg); toxic elements (Ag, Be, Cd, Hg) were not detected in the organs of the studied plants.

3. It has been established that the content of heavy metal salts in the studied plants growing on the territory of the Republic of Uzbekistan is within the limits of the norms that are normalized by the relevant Scientific and Technical Specifications (the State Pharmacopoeia XIV of the Russian Federation and WHO).

References

Heliotropium. Plantarium. Plants and lichens of Russia and neighboring countries: open online gallerie sand plant identification guide. URL: https: //www.plantarium.ru/lang/en/page/ view/ item/ 42844.html.

Heliotropium dasycarpum Ledeb // Plantarium. Plants and lichens of Russia and neighboring countries: open online galleries and plant identification guide. URL: https://www.plantarium.ru/lang/en/page/view/item/18440.html.

Vvedensky A. I. (1961). The genus *Heliotropium*. Flora of Uzbekistan, Volume 5. Tashkent: Publishing House of the Academy of Sciences of the Uzbek SSR. – P. 668.

Yunusov S. Y. (1981). Handbook of Alkaloids, Ed. Academy of Sciences of the Uzbek SSR. Tashkent, – P. 312–313.

Shakirov R., Vinogradova V. I., Aripova S. F., Sultankhodzhaev M. N., Bessonova I. A., Akhmedzhanova V. I., Tulaganov T. S., Salimov B. T., (2013). Natural Compounds: Plant, Sources, Structure and Properties, Springer. – New York. – P. 16–18. URL: http://www.springer.com/us/book/9780387491394

Kakar F., Akbarian Z., Leslie T., Laice M., Watson D., Van Hans E., Fahim O., Mofle D. (2010). // Journal of Toxicology. 1–7. DOI:10.1155/2010/313280.

Chuanhui Ma, Yang Liu, Lin Zhu, Hong Ji, Xun Song. (2018). Determination and regulation of hepatotoxic pyrrolizidine alkaloids in food: A critical review of recent research (англ.) // Food and Chemical Toxicology. 2018–09–01. – Vol. 119. – P. 50–60. ISSN 0278-6915. Doi:10.1016/j.fct.2018.05.037.

Xia Q., Yan J., Chou M. W., Fu P. P. (2008). Formation of DHP-derived DNA adducts from metabolic activation of the prototype heliotridine-type pyrrolizidine alkaloid, heliotrine // Toxicology letters. – V. 178. – No. 2. – P. 77–82.

Omonova S. S., Khuzhaev V. U., Aripova S. F. (2025). Alkaloid Content in Plants of The Genus Heliotropium Growing in The Ferghana Valley of Uzbekistan, Materials of the Scientific and practical conference “Actual problems of chemistry of natural compounds”, Tashkent, April 19, – 58 p.

RakhimovaSh. Kh., Mezhlumyan L. G., Omonova S. S., Azamatov A. A., Aripova S. F., Nabieva F. S., (2025). Investigation of The Protein Components of The Aboveground Part of The *Heliotropium Lasiocarpum* Plant and Its Biological Activity. Materials of the Scientific and practical conference “Actual problems of chemistry of natural compounds”, Tashkent, April 19, – 185 p.

Omonova S. S., Matchanov O. D., Khasanov R. S., Aripova S. F. (2024). Study of the content of flavonoids and vitamins in plants of the genus *Heliotropium* growing in Uzbekistan, Uzbek Biological Journal, – No. 5. – P. 10–13.

Oberlis D., Harland B., Skalny A., (2018). The biological role of macro- and microelements in humans and animals, Orenburg, – 658 p.

OFS.1.1.0013.15. (2018). Statistical processing of the results of a chemical experiment // State Pharmacopoeia of the Russian Federation, XIV ed., – Moscow, – Vol. 1. – P. 289–318.

Polyanskaya I. S. (2014). A new classification of bioelements in bioelementology // Dairy and Economic Bulletin,. – No. 1. – P. 34–42.

Lysikov Yu. A. (2008). Macro- and microelements in the human body: functions, deficit/surplus // Specialist’s Handbook Magazine. – No. 20. – 262 p.

Kolomiytseva M. G., Gabovich R. D. (1970). Microelements in medicine. Monograph, M. Medicine. 1970. – 288 p.

Greer F. R., Krebs N. F., (2006). American Academy of Pediatrics Committee on Nutrition. Optimizing bone health and calcium intakes of infants, children, and adolescents (англ.) // Pediatrics: journal, American Academy of Pediatrics. – Vol. 117. – No. 2. – P. 578–585. PMID 16452385.

Hatfield, D. L., Gladyshev, V. N. How Selenium Has Altered Our Understanding of the Genetic Code (англ.) // Molecular and Cellular Biology: Journal. 2002. – Vol. 22. – No. 11. –

P. 3565–3576. Doi:10.1128/MCB.22.11.3565-3576.2002. PMID 11997494. PMC 133838.

Struyev I. V., Simakhov R. V. (2006). Selenium, its effect on the body and its use in medicine // Collection of scientific papers "Natural Sciences and humanism". Edited by Professor, Doctor of Biological Sciences N. N. Ilyinsky, – 3(2). – P. 127–136.

Idelson L. I., Vorobyev A. I. (2005). Iron deficiency anemia. Guide to Hematology. Edited by A. I. Vorobyov in 3 volumes. Newdiamed. – 123 p.

Tivo P. V., Bytko I. G. (1996). Heavy metals and Ecology, Minsk. Unipol, – 191 p.

OFS 1.5.3.0009.15. (2015). Determination of the content of heavy metals and arsenic in medicinal plant raw materials and medicinal herbal preparations // State Pharmacopoeia of the Russian Federation. XIII ed. – Moscow, – Vol. 2. – P. 421–433.

World Health Organization et al. (2005). National policy on traditional medicine and regulation of herbal medicines: Report of a WHO global survey. Geneva. – P. 168; ОФС.1.1.0009. 4579.1.

Financing. *This work was funded by the budget of the Yunusov Institute of Plant Chemistry of the Academy of Sciences of the Republic of Uzbekistan, the Sadikov Institute of Bioorganic Chemistry of the Academy of Sciences of the Republic of Uzbekistan, and the Kokand State Pedagogical University. No additional grants have been received to conduct or direct this particular study.*

Conflict of interests. *The authors of this paper declare that they have no conflict of interest.*

submitted 05.06.2025;
accepted for publication 18.06.2025;
published 31.07.2025

Contact: salima_ aripova@mail.ru

The Austrian Journal of Technical and Natural Sciences, No 5–6
ISSN 2310-5607

PREMIER Publishing
ppublishing.org

DOI:10.29013/AJT-25-5.6-69-73

STUDY OF THE PROCESS OF COMPLEX FERTILISER PRODUCTION

Saparova G.D.[1], Khairiev F.B.[2], Erkaev A.U.[3], Kucharov B.H.[2], Obidjonov D.[2]

[1] Karakalpak Research Institute of Natural Sciences, Karakalpak Branch of the Academy of Sciences of the Republic of Uzbekistan, Nukus, Uzbekistan

[2] Institute of General and Inorganic Chemistry, Academy of Sciences of the Republic of Uzbekistan, Tashkent.

[3] Tashkent Institute of Chemical Technology

Cite: *Saparova G.D., Khairiev F.B., Erkaev A.U., Kucharov B.H., Obidjonov D. (2025). Study of the process of complex fertiliser production. Austrian Journal of Technical and Natural Sciences 2025, No 5–6.* https://doi.org/10.29013/AJT-25-5.6-69-73

Abstract

This paper presents data on the production of magnesium-containing fertilizers based on the processing of serpentinite of Karakalpak deposit. Their chemical composition, physico-chemical properties (moisture content, volume weight, hygroscopicity, fluidity) were investigated. Chemical analyses of the obtained sample showed that the sample consists mainly of iron-13.7, magnesium-27.2, aluminium-5.66, nickel-7.66, silicon-1.30%. Also present are: calcium-1.25, manganese-0.578, cobalt-0.210 and titanium-0.0662% giving the material strength, heat and corrosion resistance. After the process of ammonization and packing to solid state, the magnesium-containing nitrogen fertilizer (three samples) consists of the sum of nutrient elements 39.5; 44.2 and 41.46%, in particular N-21.86; 22.5; 23.86%, of which 5.44; 4.74; 6.7% in ammonium form, Mg-18.3; 21.7; 17.4% respectively at pH 3; 4 and 5.

Keywords: *serpentenite, magnesium nitrate, magnesium-containing nitrogen fertilizer, physical and chemical properties*

Introduction

The main task of the agro-industrial complex of Uzbekistan is to increase the production of agricultural products in such volumes that will allow to ensure the food programme, as well as to increase the quantity and quality of exported agricultural products, which is inextricably linked to the intensification of the industry, one of the most important conditions of which is the rational use of fertilizers that provide not only an increase in crop yields, but also the preservation and improvement of the overall level of soil fertility

In recent publications magnesium is considered on a par with other basic nutrition elements, since its deficiency in mineral nutrition limits not only the possibility of obtaining high yields, but also a decrease in the quality of agricultural products (Aristarkhov A. N., 2002).

Magnesium is a mesoelement that is directly involved in many metabolic processes in plant development: including photosynthesis, phosphorus uptake and transport, amino acid and protein synthesis, and helps maintain turgor pressure, which is essential for maintaining plant form and structure.

The authors (Aristarkhov A. N., 2000; Mittler R., 2006) state that magnesium supply has a positive effect on the growth of roots and vegetative mass of plants, frost and drought resistance, resistance of plants to leaf burns from solar radiation, and resistance to fungal diseases

Magnesium deficiency has a major impact on the distribution of dry matter and carbohydrates between shoots and roots. One of the earliest plant responses to magnesium deficiency stress is a marked increase in shoot to root dry weight ratio, which is associated with massive accumulation of carbohydrates in leaf sources, especially sucrose and starch. Studies with common bean and sugar beet plants have shown that Mg plays a fundamental role in sucrose loading of the phloem. These results indicate that the accumulation of carbohydrates in magnesium-deficient leaves is directly caused by magnesium deficiency stress (Cakmak I., Kirkby E. A., 2008).

Our interest in obtaining magnesium fertilizers is understandable, one of which magnesium nitrate – a 2-component fertilizer containing the most important elements necessary for the basic life processes of plant organisms – nitrogen and magnesium, in our opinion, can find a worthy application. As part of the development of technology for obtaining magnesium-containing fertilizer from serpentinite, we set the task to create a product that combines high agrochemical activity and a minimum level of impurities. The research is focused on the formation of magnesium-ammonium nitrate, which combines the key nutrients – magnesium and nitrogen.

Materials and Methods. Quantitative analysis of elemental composition was performed on a high-performance energy dispersive X-ray fluorescence spectrometer Rigaku NEX CG EDXRF (Japan). The analyser captures concentrations from tenths of mg/kg. This method indicates the optimum wavelength of the determined micro- and macroelement at which it has maximum emission (Fig. 1). Determination of CaO and MgO content was carried out by volumetric complexometric method: titration with 0.05n Trilon B solution in the presence of indicators fluorexon and chromium dark blue (Vinnik M. M., Erbanova L. N., Zaitsev P. M. et al., 1975). Nitrogen content in the products was determined by Kjeldahl method – by ammonia distillation in alkaline medium with Devard's alloy followed by titration (GOST 30181.4–94.; Myrzakozha, D.A., Mirzakhodzhaev A. A., 2013).

Results of the study. In the process of nitric acid decomposition of local raw material – serpentinite of Karakalpak deposit, composition (weight %): 33–34% MgO and 41–42% SiO_2. It is shown that with increase of pH of the medium up to 3.0–3.5 the degree of iron and aluminum settling is only 99.47–99.52%, and the precipitation of semithin oxides completely falls out, releasing the composition of magnesium nitrate and ammonium nitrate solution. The wet precipitate was dried at room temperature to constant weight. The dry magnesium nitrate contains about 90–95% Mg O. The liquid phase containing ammonium, calcium and magnesium nitrates can subsequently serve as a liquid fertilizer $Mg(NO_{3)2}$, containing up to 15.40% nitrogen, which is in nitrate and ammonium forms in amounts of 7.26% and 8.14% (Saparova G. D., Dzhandullaeva M., Erkaev A. U. Kucharov B. Kh., 2022; Saparova Gulnar Dauletmuratovna, Zhandullaeva Munavvara, Erkayev Aktam Ulashevich, Kucharov Bakhrom Khairievich, Bauatdinov Saliy, 2023; Saparova G. D., Kucharov B. H., Jandullaeva M. S., Erkaev A. U., Zakirov B. S., 2024).

The ammoniated slurry was brought dry state at pH 4 and 5 by packing, resulting in solid iron-magnesium-ammonium-nitrate fertilizer with total nutrient elements of 44.2 and 41.46% and content of 22.5; 4.76 and 23.86 6.7% nitrogen and magnesium respectively.

The resulting iron-magnesium-nitrate-ammonium fertilizer ($Fe\text{-}Mg\text{-}NH_4\text{-}NO_3$), a complex mineral fertilizer containing iron, magnesium and nitrogen in ammonium and nitrate forms, can provide plants with the necessary elements for photosynthesis,

growth and metabolism. The presence of iron and magnesium also stimulates chlorophyll formation, improves metabolic processes and increases resistance to stress. The balanced composition of the fertilizer promotes rapid assimilation of nutrients, reduces the risk of micronutrient deficiency, which will recommend its use for growing grain, vegetable and fruit crops when applied to the soil or as foliar fertilizer to increase yields and product quality.

Figure 1. *Obtained iron-magnesium-nitrate-ammonium nitrate fertiliser (IMNAU)*

pH4.1 **pH5.12**

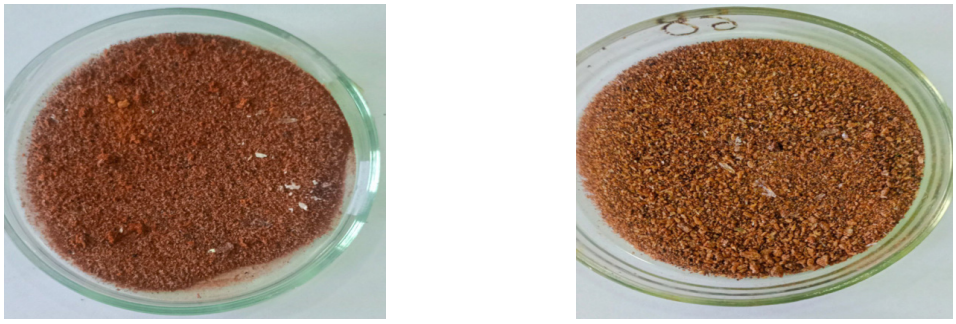

Figure 2. *Analysis of the chemical composition of the udolbronium sample (IMNAU) at pH 5.12 using the FP method*

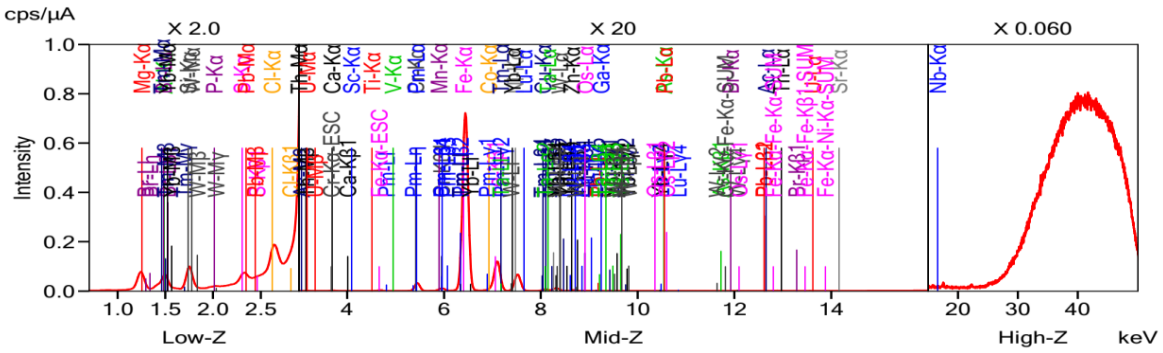

The sample consists mainly of: iron-13.7, magnesium-27.2, aluminium-5.66, nickel-7.66, silicon-1.30%. Calcium-1.25, manganese-0.578, cobalt-0.210 and titanium 0.0662% are also present, giving the material strength, heat and corrosion resistance.

After the ammonization process and packing to solid state, a magnesium-ammonium-nitrate fertilizer with 0.02 and 0.012% aluminum and iron content can be obtained.

Figure 3. *Obtained magnesium-nitrate-ammonium fertilizer (MNAF)*

pH4.1 **pH5.12**

Thus, the magnesium-nitrate-nitrogen fertilizer **MNAF** (three samples) consists of the sum of nutrient elements 39.5; 44.2 and 41.46%, in particular N-21.86; 22.5; 23.86%, of which 5.44; 4.74; 6.7% in ammonium form, Mg – 18.3; 21.7; 17.4% respectively at pH 3; 4 and 5. The obtained magnesium-nitrate-ammonium fertilizer (MNAF) is a complex mineral fertilizer containing magnesium, ammonium and nitrate nitrogen, provides plants with important nutritional elements. Due to high solubility and availability of elements for plant nutrition, MNAF promotes active photosynthesis, stimulates growth and development of plants, improves their resistance to unfavorable conditions. It is well soluble in water, ensuring a uniform supply of nutrients. Unlike traditional magnesium fertilizers, magnesium-ammonium-nitrate fertilizer has a synergistic effect due to the combination of magnesium and ammonium form of nitrogen.

The obtained MNAF and IMNAF have the following marketable properties.

Table 1. *Commodity properties of the fertilizer's obtained*

No.	Fertiliser	Humidity, %	Volume weight, (g/cm³):	Natural slope angle,°C	Hygroscopic point, %	Current, c
1	IMNAF pH 4.1	18.69	0.742	40	50	5.4
2	IMNAF pH 5.12	20.48	0.839	30	55	5.1
3	MNAF pH 4.1	18.19	0.717	35	48	6.2
4	MNAF pH 5.12	18.76	0.723	30	43	6.0

IMNAF has a higher moisture content compared to MNAF, which may be related to the hydrophilicity of iron-containing compounds. Variations in pH (4.1 and 5.12) are related to changes in salt solubility and moisture retention capacity.

Volumetric weight (g/cm³): IMNAF has a high volume mass due to the presence of iron-containing compounds with high density. Increasing the pH increases the bulk mass, probably due to changes in the crystal structure of the fertiliser.

Hygroscopic point (%): IMNAF is less sensitive to moisture than MNAF, which may require special storage conditions to prevent clumping. The exact quantitative hygroscopicity depends on conditions, but, for example, at relative humidity above 45–55% the resulting fertiliser starts to actively absorb water, and at 70–75% it completely dissolves in its own absorbed moisture, forming a saturated solution.

The flowability index characterises the ability of the fertiliser to pour freely. All values are in a similar range, which indicates good bulkiness and convenience for mechanised application.

Conclusion

Thus, as a result of nitric acid decomposition of serpentinite of Karakalpak deposit a liquid phase containing ammonium, calcium and magnesium nitrates is formed, which can serve as a liquid fertiliser $Mg(NO_{3)2}$, containing up to 15.40% of nitrogen, which is in nitrate and ammonium forms in the amount of 7.26% and 8.14%. After the process of ammonisation and packing to a solid state the commercial properties of the obtained fertilizers were investigated. It was found that the volume weight (g/cm³) of the fertilisers has a large volume mass, which is due to the presence of iron-containing compounds with high density. hygroscopic point is less sensitive to moisture, which may require special storage conditions to prevent clumping

References

Aristarkhov A. N. (2002). Agrochemical substantiation of magnesium fertiliser application // Fertility, – No. 3. – P. 15–17.

Aristarkhov A. N. (2000). Optimisation of plant nutrition and fertilizer application in agroecosystems. – M.: CINAO. – 524 p.
Mittler R. (2006). Abiotic stress, the field environment and stress combination // Trends Plant Science, – No. 11. – P. 15–19.
Cakmak I., Kirkby E. A. (2008). Role of magnesium in carbon partitioning and alleviating photooxidative damage // Physiol. Plant., – No. 133.
Vinnik M. M., Erbanova L. N., Zaitsev P. M. et al. (1975). Methods of analysis of phosphate raw materials, phosphate and complex fertilisers, fodder phosphates. Moscow: Khimiya, – 218 p.
GOST 30181.4–94. Mineral fertilisers. Method for determination of total mass fraction of nitrogen contained in compound fertilisers and nitrate in ammonium and nitrate forms (Devard method).
Myrzakozha, D.A., Mirzakhodzhaev A. A. (2013). Modern methods of research / – Almaty., Editorial and publishing centre KBTUB. – 280 p.
Saparova G. D., Dzhandullaeva M., Erkaev A. U. Kucharov B. Kh. (2022). Studies of the Chemical and Mineral Composition of Serpentinite of the Karakalpak Deposit // International Journal of Advanced Research in Science, Engineering and Technology. – Vol. 9. – Issue 8, August, 1966. – P. 6–19670.
Saparova Gulnar Dauletmuratovna, Zhandullaeva Munavvara, Erkayev Aktam Ulashevich, Kucharov Bakhrom Khairievich, Bauatdinov Saliy. (2023). Study of the process of isolation of magnesium compounds from serpentinite // Austrian Journal of Technical and Natural Sciences. – No. 1–2. – P. 38–42
Saparova G. D., Kucharov B. H., Jandullaeva M. S., Erkaev A. U., Zakirov B. S. (2024). Nitric acid processing of serpentinites of Karakalpak deposit // Journal of Chemistry for Sustainable Development. – No. 1. – P. 84–89.

submitted 12.05.2025;
accepted for publication 28.05.2025;
published 31.07.2025

Contact: gulnor-sayler@mail.ru

The Austrian Journal of Technical and Natural Sciences, No 5–6
ISSN 2310-5607

PREMIER Publishing
ppublishing.org

DOI:10.29013/AJT-25-5.6-74-77

STUDY OF CATALYSTS PREPARED BY IMPREGNATION WITH AQUEOUS COBALT NITRATE SOLUTION

Togayev Abror Ikrom ogli [1], ***Kobilov Nodirbek Sobirovich*** [1]

[1] Karshi State Technical University

Cite: *Togayev A.I. Kobilov N.S. (2025). Study of Catalysts Prepared by Impregnation With Aqueous Cobalt Nitrate Solution. Austrian Journal of Technical and Natural Sciences 2024, No 5–6.* https://doi.org/10.29013/AJT-25-5.6-74-77

Abstract

The article considers the catalyst production stage – a gradual increase in the synthesis temperature in a flow of synthesis gas – as a necessary stage of the Fischer-Tropsch synthesis, since during the development process it was determined that the formation of catalytically active centers under the influence of the catalyst was observed. It can be assumed that in this temperature range, water is released from the capillaries of the binder – aluminum oxide and micropores of H-shaped zeolites. In the presence of cationic zeolites, such a plateau is absent due to the hydrophilicity of such zeolites, in which water is retained near the cations under the influence of electrostatic forces.

Keywords: *cation exchange resin, catalyst, Fischer-Tropsch synthesis, conversion, capillary condensation, zeolites, selectivity*

Introduction

In an era of developing modern technologies, one of the main directions of the chemical industry is the creation of effective catalysts and the study of their active properties. Catalysts are of great importance in increasing the speed of chemical reactions, reducing energy consumption, and introducing environmentally friendly technologies. Today, various catalytic systems are widely used in many industries, in particular in the fields of oil and gas chemistry, pharmaceuticals, and environmental protection. In particular, cobalt-based catalysts are distinguished by their high activity and stability (Rakhmatov et al., 2023).

We will talk about the preparation of catalysts using an aqueous solution of cobalt nitrate and the analysis of their physicochemical properties. Scientific research in this area is carried out using the impregnation (i.e., wetting) method, since this method allows the active component to be evenly deposited on the surface of the base material (for example, aluminum oxide, silicon dioxide, etc.) (Togayev, 2023).

Cobalt-based catalysts are widely used in many reactions, such as oxidation, hydrogenation, and Fischer-Tropsch synthesis. Such catalysts are mainly prepared using cobalt nitrate salts. One of the most commonly used methods is the soaking method, in which the preparation process is as follows: first, a solution of cobalt(II) nitrate is prepared in water, then it is poured onto a specially selected support

substance and mixed. As a result, cobalt ions are impregnated on the surface of the support. Then, through the processes of drying and calcination (i.e. heating), the final form of the catalyst is obtained (Rakhimov, 2024).

The efficiency of the catalyst depends on several factors: its surface area, cobalt content, particle size, heat resistance and chemical stability. Modern physicochemical analysis methods – for example, BET (surface characterization), XRD (X-ray diffraction), SEM (scanning electron microscopy) – allow the structure of the catalyst to be studied in depth. Studies show that correctly selected impregnation conditions (pH, concentration, time) allow obtaining catalysts with high activity.

Cobalt catalysts also play an important role in environmental protection. For example, cobalt-based catalysts are used in reactors that decompose harmful substances in automobile exhaust gases and in systems that reduce NOx oxides. In addition, they are widely used in biofuel production and exhaust gas purification.

Catalysts prepared by the impregnation method using cobalt nitrate solution are of great importance in the industrial and environmental sectors. If their physicochemical properties are thoroughly analyzed and effective reaction conditions are determined, even higher results can be achieved. In the future, this type of research will serve as an important basis for creating sustainable and energy-efficient technologies (Rakhimov, 2024).

Metod and material

In this scientific study, catalysts were prepared by the impregnation method using an aqueous cobalt(II) nitrate solution. Various support materials were used for catalyst preparation, namely zeolite-based supports (NaX, KA, CaA and H-form zeolites: HY6, HY30, HB) and granular supports without zeolite.

The impregnation method was carried out as follows: an appropriate amount of cobalt nitrate solution was used for each support. In the preparation of the solution, analytically pure $Co(NO_3)_2 \cdot 6H_2O$ was dissolved in distilled water and then poured onto a zeolite or other granular support and uniformly impregnated. During the impregnation process, the mixture was continuously stirred at room temperature for 3–4 hours. After that, the wet samples were dried at 100 °C and calcined in a muffle furnace at 450 °C for 4 hours. During the calcination stage, cobalt salts decompose and turn into active metal or oxide forms.

Results

The effect of synthesis temperature

It is known that the catalyst production stage – a gradual increase in the synthesis temperature in a stream of synthesis gas – is a necessary stage of the Fischer-Tropsch synthesis, since during the development process catalytically active centers are formed under the influence of. Studies by the authors (Rakhmatov, 2023) showed that during the development of a cobalt catalyst, a change in the state of cobalt occurs: under the influence of the reaction medium, part of CoO is converted to $Co^{\delta+}$. This leads to a change in the nature of CO adsorption. Thus, the active surface of the catalyst is formed during the production process.

In the course of development, the dependence of the main synthesis parameters on temperature was obtained for each catalyst.

Figure 1 shows the dependence of CO conversion on the synthesis temperature in the presence of impregnation catalysts. With increasing temperature, the conversion of CO increased in the presence of all catalysts. The highest CO conversion – 80% – was obtained in the presence of a catalyst with HB zeolite. It is interesting that in the dependence obtained with the presence of Co/HB, Co/HY6 Co/HY30 and without a zeolite catalyst, a “step” was observed when the synthesis temperature increased from 190 to 210 °C, probably due to capillary condensation of the synthesis products. It can be assumed that in this temperature range, water is released from the capillaries of the binder – aluminum oxide and micropores of H-shaped zeolites. In the presence of cationic zeolites, such a plateau is absent due to the hydrophilicity of such zeolites, in which water is retained near the cations under the influence of electrostatic forces. The lowest CO conversion was obtained in the presence of a KA zeolite-based absorption catalyst – no more than 20% over the entire temperature range.

Figure 2 shows the dependence of the selectivity for the formation of C_{5+} hydrocarbons

on the synthesis temperature. In the presence of all catalysts, this indicator decreased with increasing temperature. In the presence of catalysts without zeolites and catalysts containing HB and HY30 zeolites, the selectivity for the formation of C_{5+} hydrocarbons decreased by 1.1–1.2 times in the temperature range 190–210 °C. In the presence of catalysts based on Co/CaA, Co/NaX cationic zeolites, a decrease of this indicator by 1.5 and 1.3 times, respectively, was observed when increasing from 210 to 220 °C. In addition, in the temperature range 210–240 °C, the selectivity for the formation of C_{5+} hydrocarbons was practically independent of the synthesis temperature in the presence of all catalysts except Co/CaA and Co/NaX.

Figure 1. *Dependence of CO conversion on FTS temperature*

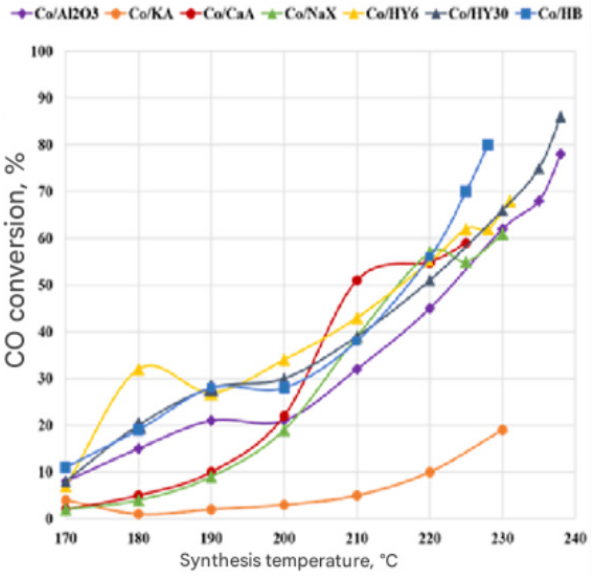

Figure 2. *Dependence of the selectivity of the formation of C_{5+} hydrocarbons on the FTS temperature*

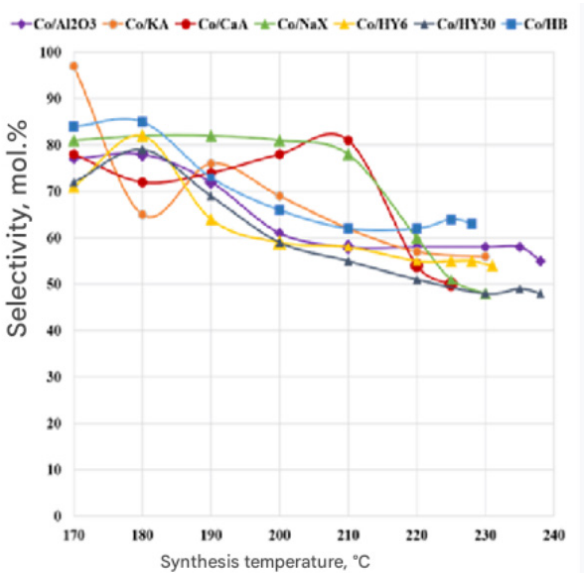

Figure 3 shows the dependence of the yield of C_{5+} hydrocarbons on the synthesis temperature. In the presence of all catalysts, the yield of liquid hydrocarbons increased with increasing synthesis temperature. In the presence of catalysts based on H-forms of zeolites and catalysts without a zeolite, a step was observed at 180–200 °C. The highest yield of C_{5+} hydrocarbons – more than 97 g/m^3 – – was obtained in the presence of a catalyst based on HB zeolite. In the presence of catalysts based on zeolites cationized with alkali and alkaline earth metals, the yield of C_{5+} hydrocarbons was significantly lower and amounted to 58 g/m^3 in the presence of Co/NaX and Co/CaA, and 21 g/m$_3$ in the presence of Co/KA.

The selectivity of methane formation increases with increasing synthesis temperature in the presence of all catalysts. However, the nature of this dependence is somewhat different. In the presence of a zeolite-free catalyst and catalysts based on H-form zeolites, this dependence reaches a maximum at 210–230 °C, which corresponds to 25–30%. In the presence of catalysts based on zeolites cationized with Na and Ca, the selectivity of methane formation increases sharply – by 2.3––3.6 times – with an increase in temperature from 210 to 220 °C. In the presence of Co/CA, this indicator increases from 1 to 20%, in parallel with an increase in the Fischer-Tropsch synthesis temperature.

Thus, despite the literature data on the sharp increase in methane production when using zeolites as carriers compared to conventional Fischer-Tropsch synthesis catalysts, the selectivity of the catalyst with HB zeolite is lower than that of the catalyst without zeolite over the entire temperature range.

Conclusion

The results of this study showed that the composition of cobalt catalysts prepared by the impregnation method, especially with or without zeolite, significantly affects their ac-

tivity and selectivity. This confirms that the formation of catalytic active sites and the process of CO adsorption on the reaction surface depend on the nature of the support material.

Also, as a result of a gradual increase in the synthesis temperature, a partial conversion of CoO to the Co^δ+ form was observed, which is an important factor in the formation of the active surface of the catalyst. Although zeolites have a high surface area and ion exchange capacity, they do not always guarantee high selectivity. In particular, the low selectivity of HB-zeolite indicates that the optimal location of the active sites and metal dispersion may not be sufficiently ensured.

The results indicate that in the development of cobalt-based catalysts, a thorough analysis of the properties of the support material, optimization of synthesis conditions, and consideration of the effect of the reaction medium are important in increasing efficiency.

References

Rahmatov X. B., Togayev A. B., Kamolov L. S. Technology for producing dimethyl ether and converting methane into lower olefins – ethylene, propylene and butylene // QarDU xabarlari – No. 2/1(58). 2023. mart-aprel. – P. 53–56.

Togayev A. B., Rahmatov X. B. , Kamolov L. S. Fisher-tropsh jarayoni asosida benzin qatori suyuq uglevodorodlar sintezining ilmiy asoslarini ishlab chiqish // QarDU xabarlari – No. 3/1(59). 2023. may-iyun. – P. 95–98.

Rakhmatov H. B., Togaev A. I., Kamolov L. S. Production of synthetic gasoline from natural gas // QarDU xabarlari. Maxsus son – (63). 2023. dekabr. – P. 72–74.

Rakhimov, G., & Yuldashev, T. (2024, November). Study of the degree of foaming of absorbent compositions used when purifying gases from acidic components. In *AIP Conference Proceedings* (Vol. 3244, No. 1). AIP Publishing.

Rakhimov, G., & Murtazayev, F. (2024, November). Study of physico-chemical properties of domestic AI-80 automobile gasoline and reduction of benzene content in gasoline. In *American Institute of Physics Conference Series* (Vol. 3244, No. 1, p. 050019).

Rakhimov, G., Kuybokarov, O., & Karshiyev, M. (2024). Research of the catalytic properties of a catalyst selected for the production of high-molecular weight liquid synthetic hydrocarbons from synthesis gas. In *E3S Web of Conferences* (Vol. 498, p. 01008). EDP Sciences.

submitted 17.04.2025;
accepted for publication 01.05.2025;
published 29.05.2025

Contact: king08@mail.ru

The Austrian Journal of Technical and Natural Sciences, No 5–6
ISSN 2310-5607

PREMIER Publishing
ppublishing.org

DOI:10.29013/AJT-25-5.6-78-85

POLYSACCHARIDES OF PLEUROTUS OSTREATUS MUSHROOM

Tursunova Nilufar [1], ***Kamolov Luqmon*** [1], ***Nomozova Mohigul*** [1]

[1] Karshi State University, Republic of Uzbekistan, Karshi

Cite: *Tursunova N., Kamolov L., Nomozova M. (2025). Polysaccharides of Pleurotus Ostreatus Mushroom. Austrian Journal of Technical and Natural Sciences 2024, No 5–6.* https://doi.org/10.29013/AJT-25-5.6-78-85

Abstract

In this study, polysaccharide fractions extracted with water and precipitated with ethanol from the mushroom *Pleurotus ostreatus* growing in Uzbekistan were studied. The functional groups in the fractions were identified by IR spectroscopy and confirmed that they were mainly β –(1 → 3) /(1 → 6)-glucans. The biological activity of the obtained substance was based on its structural properties. Polysaccharides are the most famous and most potent substances derived from mushrooms that have antitumor and immunomodulatory properties. *Pleurotus ostreatus* polysaccharides – β – glucans – are also known to have antitumor activity, as they are known from the literature to strengthen the immune system and activate natural defenses against tumors.

Keywords: *Pleurotus ostreatus, polysaccharides, β – glucans, IR spectrum, biological activity*

Introduction

Pleurotus ostreatus is a species of mushroom widely distributed in Uzbekistan and of nutritional and pharmaceutical importance. This mushroom contains biologically active polysaccharides such as β – glucans, which have immunomodulatory, antioxidant and antitumor properties. Studying the structure of these polysaccharides and evaluating their biological activity is a pressing issue for modern scientific research. Mushrooms have been part of the human diet for thousands of years in many Asian countries, such as China, Korea and Japan. It is known that mushrooms are valuable food for health, as they are rich in fats and proteins, vitamins and rare minerals. Currently, the beneficial effects of mushrooms are increasingly recognized and they are attracting great attention in food and pharmaceutical applications (Zhang Y. et al., 2012). Natural antitumor polysaccharides isolated from mushrooms include acidic and neutral polysaccharides with various glycosidic linkages, and some are linked to protein or peptide residues, such as polysaccharide-protein or peptide complexes. In addition to the primary structure, the higher structure of polysaccharides, such as chain conformation, also plays an important role in their antitumor activity. Most polysaccharides are classified as non-specific bioactive substances because their exact mode of action is unknown and the chain conformation of their active components has not been determined (Zhang, M.,

Cui, S.W., Cheung, P.C.K., & Wang, Q. 2007). Mushroom polysaccharides play an important role in functional foods because they also exhibit biological modulatory properties such as antiviral and antibacterial activities. The production, purification, and characterization of intracellular and extracellular free and protein-bound polysaccharides from *Pleurotus ostreatus* and their growth inhibitory effects on human carcinoma cell lines have been studied (Silva S. et al., 2012). Carbohydrates are one of the main nutrients of mushrooms, accounting for approximately 40–70% of the dry weight, including low and high molecular weight carbohydrates, with low molecular weight carbohydrates consisting primarily of monosaccharides, disaccharides, and sugar alcohols (polyols), such as glucose, trehalose, mannitol, and arabitol. High molecular weight carbohydrates are primarily polysaccharides such as glucans and chitin. Some of the carbohydrates abundant in mushrooms can be obtained for food, medical, and cosmetic purposes. For example, sugar alcohols contain relatively few calories and can be used as sugar substitutes in desserts and other foods. The hygroscopicity of trehalose makes it an ideal humectant for use in cosmetics. Fungal chitin and its deacetylated derivative chitosan have antimicrobial bioactivity and can be used as a wound healing agent. Finally, polysaccharides such as β – glucan have immunomodulatory activity by stimulating macrophages and other white blood cells (Zhou S. et al., 2016). Mushroom carbohydrates are obtained from compost substrates such as wood, straw, and straw, which contain approximately 60–70% cellulose and hemicelluloses. During mushroom growth, cellulose and hemicellulose are hydrolyzed by enzymes from the mycelium, transported into mycelial cells, and then metabolized through various carbohydrate pathways. In addition to being degraded by glycolysis to produce energy for growth, metabolites can be synthesized into structural polysaccharides of the cell wall, such as glucan and chitin. Metabolites can also be synthesized into glycogen, arabitol, trehalose, or mannitol for use in developmental or later growth phases. The distribution of carbohydrates in mushrooms varies significantly in different regions during growth and fruiting. The distribution of carbohydrates in the compost and fruiting bodies of *Pleurotus ostreatus* was analyzed. When the amounts of sugars, polyols, polysaccharides and chitin were determined at different growth stages and in different parts of the fungus, trehalose, mannitol and glucose were first accumulated in the compost, and then decreased during the differentiation and growth of the fruiting body. Polysaccharides were mainly accumulated in the fruiting body and its adjacent regions of the fungus, and chitin was mainly observed in the basal region. These findings provide insights into the function and utilization of carbohydrates during fungal growth (Zhou S. et al., 2016). Of all the biologically active components, polysaccharides in particular, β – glucan is the most studied group of functional compounds in mushrooms. β – glucan is a long-chain polymer of glucose units linked together by glycosidic bonds, found in the cell walls of oats, barley, yeast, and fungi. β – glucans from different sources have different bond types, branching patterns, and molecular weights. In oats and barley, it consists of a linear glucose polymer with β – (1–3), β – (1–4) linkages, and β – (1––6) linkages. The β – glucan content in fungi ranges from 0.21 to 0.53 g/100 g (dry weight basis). Most of the fungal β – glucan is found as an insoluble fraction (54–82%) and only a small portion (16–46%) is found as a soluble fraction. Mushroom β –glucans are known as biological response modifiers (BRM), which are used in both modern medicine and traditional chemotherapeutic drugs to treat cancer and various infectious diseases (Khan A.A. et al., 2017). In fact, β –glucans are the main pathogen-associated molecular pattern recognized in fungal infections and responsible for triggering the immune response. The immune system Modulation by β –glucans is complex, involving many factors that are not yet fully understood (Pérez-Bassart Z. et al., 2023). There are over 200 clinical trials documenting their use for a range of applications. Since 1980, licensed drugs containing β –glucans have also been available on the pharmaceutical market in Japan for the treatment of cancer. β –glucans have been recognized as pharmaceutical agents in several countries, including the United States, Canada, Finland, Sweden, China, and Korea. The diverse functional effects of these molecules include modifying lipid and glucose metabolism, lowering

cholesterol, regulating obesity and reducing the risk of cardiovascular disease and diabetes, modulating the gut microbiome, modifying lipid and glucose metabolism, and beneficial effects on gastrointestinal diseases, etc. β –glucans, especially those derived from non-cereal sources, are widely known for their immunomodulatory properties, their ability to stimulate the immune response and initiate inflammatory properties, and their ability to resist infections. β –glucans derived from fungi are the most potent immune modulators. Patients with nosocomial pneumonia and When β –glucans were administered to prevent sepsis, the treatment group had a lower incidence of pneumonia, as well as a lower mortality rate, compared to the control group. was low (Murphy E. J. et al., 2022).

β –glucans are used in the food industry as gelling agents and thickeners in the production of low-fat foods with improved texture (milk, bread or yogurt). In particular, hydrogels are three-dimensional, hydrophilic, polymeric networks capable of retaining large amounts of water. Furthermore, β –glucans constitute a soluble fiber with strong prebiotic effects. Although β –glucans can be easily extracted with water, more aggressive treatments are required for the upstream β –glucans (i.e., highly alkaline solutions, pH 13–14). However, water-soluble fractions may be a more environmentally sustainable option for the production of new functional ingredients. Furthermore, discarded whole biomass and uncommercialized residues (stipes) that do not meet commercial standards such as size and appearance may be cheap and abundant sources of these compounds (Pérez -Bassart Z. et al., 2024).

Water-soluble β –glucans from *Pleurotus ostreatus,* one of the most widely cultivated mushrooms, have been shown to be an environmentally sustainable option for the production of natural emulsifiers. It is assumed that the structure and composition of β –glucan-rich extracts depend on the source (whole biomass of *P. ostreatus)* and the extraction conditions (more or less purified samples), and therefore these aspects also affect their emulsifying properties. The composition of β –glucan- rich extracts and the presence of proteins or other small compounds have been shown to play an important role in the emulsifying properties of the obtained extracts (Pérez-Bassart Z. et al., 2024). Monounsaturated and polyunsaturated fatty acids such as linoleic, oleic and linolenic acids are used in skin care. The stems of this mushroom contain large amounts of ergosterol, which serves as a valuable hypocholesterolemic supplement by inhibiting cholesterol absorption into the blood and stimulating cholesterol secretion. Ergosterol can also be converted to vitamin D upon UV irradiation, which increases calcium absorption and is essential for the skeletal system in humans (Ayser M. et al., 2023). Unlike yeast, oat, and barley β –glucans, which have been shown to play a role in various cancers, the role and mechanism of *P. ostreatus* -derived β –glucans have been studied in the treatment of cervical cancer. β –glucan particles from *P. ostreatus* have also been isolated as drug carriers for the prevention and treatment of cancer. Their biological activity against cervical cancer was investigated and it was concluded that the modified particles can induce ROS-mediated apoptosis in cancer cells (Seifeldin S. A. et al., 2024). Developing an efficient extraction technology is crucial to ensure high yield while preserving the bioactive properties of the β –glucan component (Frioui M. et al., 2024). The anti-obesity benefits of β –glucan have been studied for a long time. Results show that β –glucan can improve hypertriglyceridemia, hypercholesterolemia, hypertension, hyperglycemia and insulin resistance (Nastiti A. et al., 2024). The immune profile of patients with endocrine-dependent breast cancer (clinical stages I–II) in clinical and imaging remission after pleura (β –glucan from *Pleurotus ostreatus)* administration has shown that long-term pleura administration may have potential benefits on antitumor cellular immunity in breast cancer patients in remission (Spacek J. et al., 2022). The functionality of β –glucans is related to their physicochemical properties, such as thickening, stabilizing, emulsifying, foaming, and gelling properties. These properties have been extensively studied for β –glucans from various cereal crops, but are not well understood for β –glucans from fungi. It has been found that β –glucans from yeast can be used as thickeners, water-retaining or fat-binding agents, and emulsifying stabilizers in food products. Since yeast

and fungal glucans share a common structure, it can be assumed that they also have similar physical and chemical properties (Gallotti F., Turchiuli C., Lavelli V., 2022).

Method

Sample preparation:

Oyster mushroom The mushroom sample was collected from local areas. The dried and ground raw material was prepared for extraction.

Polysaccharide extraction:

280 g of crushed *Pleurotus ostreatus* biomass was extracted with distilled water at room temperature of 25 °C for 24–48 h. The resulting extract was first filtered. The resulting extract was reduced in solvent using vacuum. Then, it was mixed with 3 times the mass of cold ethanol, cooled for 12 hours and filtered. The residue remaining on the filter was squeezed using a cloth and dried at room temperature. As a result, 7 g of polysaccharide was obtained, which was 2.5% of the total biomass.

Results and analysis

The carbohydrates obtained as a result of the extraction were subjected to high-performance liquid chromatography and the chromatographic analysis of the obtained fraction yielded the following results.High-performance liquid chromatography analyses of the extracted carbohydrates were performed(-Figure 1).

Figure 1. *Top layered liquid chromatography results*

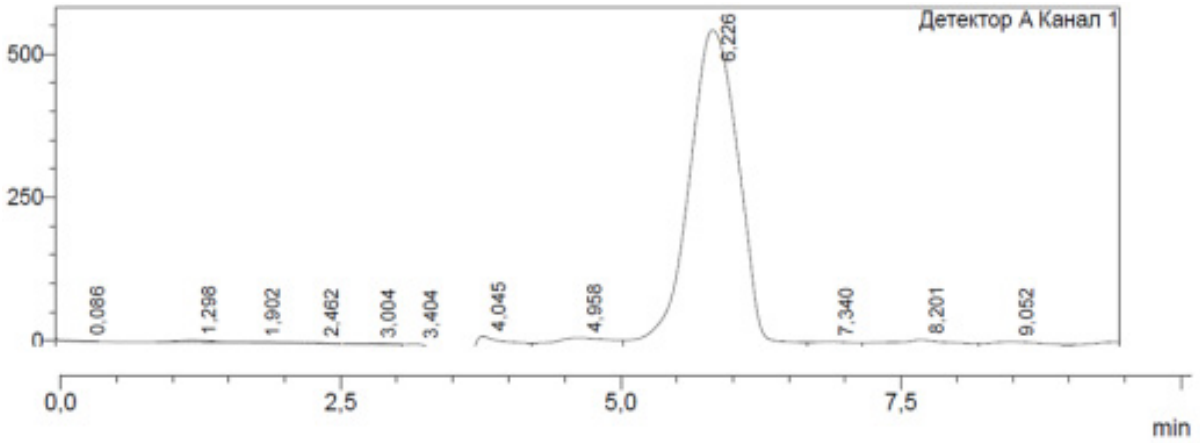

Table 1. *High effective liquid chromatography the results*

Детектор A Канал 1

Peak#	Ret. Time	Area	Height	Conc.	Unit	Mark	Name
1	0,086	5605	370	0,000			
2	1,298	65233	3231	0,000			
3	1,902	15206	734	0,000			
4	2,462	6081	496	0,000			
5	3,004	17524	983	0,000			
6	3,404	1374396	35345	0,000			
7	4,045	5285764	160394	0,000			
8	4,958	6852857	134320	0,000		V	
9	6,226	26871600	638487	0,000		V	
10	7,340	1965940	65534	0,000		V	
11	8,201	2821988	46145	0,000		V	
12	9,052	794137	20917	0,000		V	
Сумма		46076331	1106957				

The results of the table above show that the signal emitted at a time interval of 6.226 minutes was seen to have the highest concentration of 638487 g/mol.

Pleurotus ostreatus mushroom biomass were performed by extraction with distilled water at room temperature. In order to determine the structure of the isolated polysaccharide, acid hydrolysis and thin layer paper chromatography analysis were performed (Figure 2).

Figure 2. *Polysaccharide paper chromatography*

The following table was prepared by comparing the paper chromatography results with the standards (Table 2).

From the results shown in the table, it was confirmed that the polysaccharide was β –(1 → 3)/(1 → 6)-glucans.

To study their structure, IR spectra were obtained (Figure 3).

Table 2.

	Yield %	Quantitative monosaccharide composition					
		Galactose	glucose	Mannose	Arabinose	Xelose	Ravnoza
Polysaccharide	2.5%	7	93	–	–	–	–

3. Pleurotus ostreatus mushroom polysaccharide IR spectrum

The following main lines were detected in the IR spectrum: a broad extended line characteristic of –OH groups around 3279.8 cm^{-1}, 2939.36 cm^{-1} – stretching vibrations characteristic of the CH_2 – group are visible, 1624.36 cm^{-1} – bound water molecules, and in the range of 1261–1020 cm^{-1}, C–O–C and C–O–H stretching vibrations characteristic of β –glucans are visible. In the region of 961–650 cm^{-1}, deformation signals characteristic of the CH- group are visible. These signals indicate that the polysaccharide is β –glucan.

Figure 3.

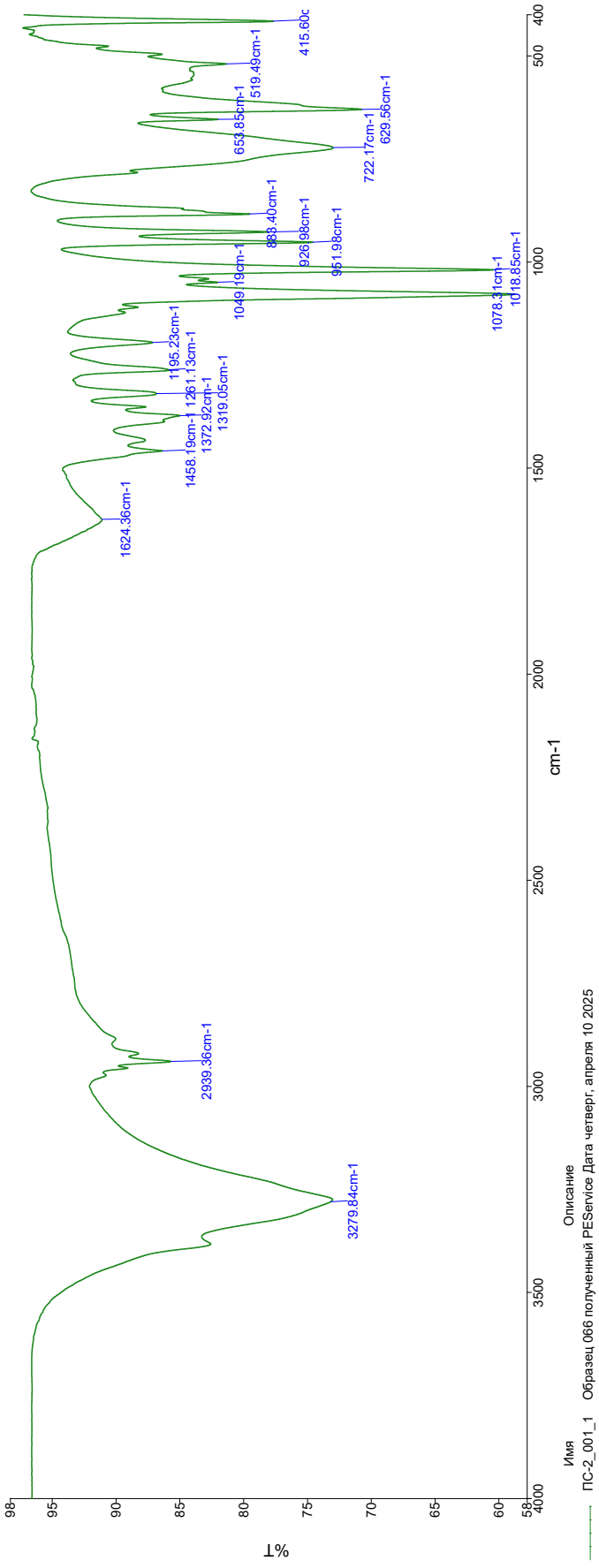
415.60c
519.49cm-1
653.85cm-1
629.56cm-1
722.17cm-1
888.40cm-1
926.98cm-1
951.98cm-1
1049.19cm-1
1078.31cm-1
1018.85cm-1
1195.23cm-1
1261.13cm-1
1319.05cm-1
1372.92cm-1
1458.19cm-1
1624.36cm-1
2939.36cm-1
3279.84cm-1
cm-1
%T
Имя
ПС-2_001_1
Описание
Образец 066 полученный PEService Дата четверг, апреля 10 2025

Conclusion

This study is an important step in the study of the extraction of β –glucans from Pleurotus ostreatus mushrooms and their biological activity. The results obtained by IR spectroscopy and HPLC analysis allowed us to determine in detail the molecular structure of the polysaccharides, their purity and bioactive activity. These results provide the basis for considering Pleurotus ostreatus mushrooms as a potential source for use in the pharmaceutical and food industries. The results obtained in the study indicate the need to study other bioactive properties of β –glucans, such as antioxidant and antibacterial activity. In the future, further study of these polysaccharides and the development of more efficient extraction methods will allow for their wider application in the pharmaceutical industry.

References

Zhang, M., Cui, S.W., Cheung, P.C.K, & Wang, Q. (2007). Antitumor polysaccharides from mushrooms: a review on their isolation process, structural characteristics and antitumor activity. *Trends in Food Science & Technology*, – 18(1). 4–19. URL: https://doi.org/10.1016/j.tifs.2006.07.013

Zhang Y. et al. (2012). Characterization and in vitro antioxidant activities of polysaccharides from Pleurotus ostreatus //International Journal of Biological Macromolecules. – T. 51. – No. 3. – P. 259–265. URL: https://doi.org/10.1016/j.ijbiomac.2012.05.003

Silva S. et al. (2012). Production, purification and characterization of polysaccharides from Pleurotus ostreatus with antitumor activity //Journal of the Science of Food and Agriculture. – T. 92. – No. 9. – P. 1826–1832. URL: https://doi.org/10.1002/jsfa.5560

Zhou S. et al. (2016). Carbohydrate changes during growth and fruiting in Pleurotus ostreatus //Fungal Biology. – T. 120. – No. 6–7. – P. 852–861. URL: https://doi.org/10.1016/j.funbio.2016.03.007

Khan A.A. et al. (2017). Structural, rheological, antioxidant, and functional properties of β –glucan extracted from edible mushrooms Agaricus bisporus, Pleurotus ostreatus and Coprinus attrimentarius //Bioactive Carbohydrates and Dietary Fiber. – T. 11. – P. 67–74. URL: https://doi.org/10.1016/j.bcdf.2017.07.006

Pérez-Bassart Z. et al. (2023). Composition, structural properties and immunomodulatory activity of several aqueous Pleurotus b -glucan-rich extracts //International journal of biological macromolecules. – T. 253. – P. 127255. URL: https://doi.org/10.1016/j.ijbiomac.2023.127255

Murphy E.J. et al. (2022). Immunomodulatory activity of β -glucan polysaccharides isolated from different species of mushroom–A potential treatment for inflammatory lung conditions //Science of the Total Environment. – T. 809. – P. 152177. URL: https://doi.org/10.1016/j.scitotenv.2021.152177

Pérez -Bassart Z. et al. (2024). Antiviral and technological properties of β – glucan-rich aqueous fractions from Pleurotus ostreatus waste biomass //Food Hydrocolloids. 2024. – T. 146. – P. 109308. URL: https://doi.org/10.1016/j.foodhyd.2023.109308

Pérez-Bassart Z. et al. (2024). Emulsifying properties of b -glucan-rich extracts obtained from Pleurotus ostreatus whole mushroom and stipes // Food Hydrocolloids. 2024. – T. 153. – P. 109961. URL: https://doi.org/10.1016/j.foodhyd.2024.109961

Ayser M. et al. (2023). Fractionating chitin-glucan complex and coproducts from Pleurotus ostreatus mushrooms //Waste and Biomass Valorization. – T. 15. – No. 5. – P. 2897–2910.

Seifeldin S.A. et al. (2024). Detection of antimicrobial, antioxidant and reactive oxygen species and caspases 3/9 mediated Anticancerous activity of b -Glucan particles derived from Pleurotus ostreatus against cervical cancer cells HeLa //Journal of King Saud University-Science. – T. 36. – No. 11. – P. 103577. https://doi.org/10.1016/j.jksus.2024.103577

Frioui M. et al. (2024). Isolation of bioactive beta-glucans from mycelium of Pleurotus ostreatus mushroom //Bioactive Compounds in Health and Disease-Online ISSN: 2574–0334; Print ISSN: 2769–2426. – T. 7. – No. 12. – S. 649–658. URL: https://doi.org/10.31989/bchd.v7i12.1511

Nastiti A. et al. (2024). The effect of oyster mushroom (Pleurotus ostreatus) beta-glucan extract on brain-derived neurotrophic factor and neuron in high-fat-high-fructose diet-induced male Sprague Dawley rats // Food Research. – T. 8. – No. 6. – P. 38–45. URL: https://doi.org/10.26656/fr.2017.8(S6).8

Spacek J. et al. (2022). Immunomodulation with β -glucan from Pleurotus ostreatus in patients with endocrine-dependent breast cancer //Immunotherapy. – T. 14. – No. 1. – P. 31–40. URL: https://doi.org/10.2217/imt-2021-0069

Gallotti F., Turchiuli C., Lavelli V. (2022). Production of stable emulsions using β –glucans extracted from Pleurotus ostreatus to encapsulate oxidizable compounds //Journal of Food Process Engineering. – T. 45. – No. 7. – P. e13949. https://doi.org/10.1111/jfpe.13949

submitted 17.04.2025;
accepted for publication 01.05.2025;
published 29.05.2025

Contact: nilufarulugbekovna0202@gmail.com; kamolov.luqmon@mail.ru;
mnomozova1992@gmail.com

The Austrian Journal of Technical and Natural Sciences, No 5–6
ISSN 2310-5607

PREMIER Publishing
ppublishing.org

Section 4. Earth science

DOI:10.29013/AJT-25-5.6-86-90

STUDY OF PATTERNS OF ACCUMULATION AND DISPERSION OF CHEMICAL ELEMENTS IN SOILS OF THE SOUTHERN ARAL SEA REGION

Zhumamuratov Azhimurat [1]***, Zhumamuratov Myrzamurat Azhimuratovich*** [2]***, Sdykov Islambek Muratbaevich*** [2]

[1] Nukus State Pedagogical Institute named after Ajiniyaz

[2] Department of Financial and Accounting, Nuku Innovation Institute

Cite: *Zhumamuratov A., Zhumamuratov M.A., Sdykov I.M. (2025). Study of Patterns of Accumulation and Dispersion of Chemical Elements in Soils of the Southern Aral Sea Region. Austrian Journal of Technical and Natural Sciences 2024, No 5–6.* https://doi.org/10.29013/AJT-25-5.6-86-90

Abstract

The article provides information on the results of a study of the patterns of dispersion of chemical elements in the soils of the Southern Aral Sea region. Comparative analysis of the chemical composition of soils from north to south according to the Muynak-Nukus-Ellikkala scheme, Republic of Karakalpakstan. The content of many elements in soils is low (with the exception of Na, K), and due to the alkaline reaction of the environment and the oxidizing conditions, their mobility in the conditions of the Aral Sea region is low.

Keywords: *Karakalpakstan, Aral Sea region, soil, geochemistry, Muynak, Nukus, Ellikkala, environmental conditions, content*

Introduction

The ecological crisis of the Aral Sea region is a result of irresponsible human interaction with nature and the environment. Specifically, over a short historical period (1960–2017), we have witnessed a profound ecological disaster in the Aral Sea region. Due to the increase in water consumption in the agriculture of the republic, the Aral Sea did not receive the necessary amount of water (about 1000 km³), resulting in the sea's desiccation. The severity of the ongoing processes, both in terms of ecological-geochemical and socio-economic aspects, is quite complex and requires the unification of scientific efforts and the economic potential of the global community.

The causes and effects of the ecological crisis in the Aral Sea region have been thoroughly researched by scientists from Karakalpakstan and the Republic of Uzbekistan, as well as by scientists from other

countries – Russia, Kazakhstan, and others. However, published works lack data on the ecological-geochemical state of the environment in the region. There is no information on the biogeochemistry of individual chemical elements, and background levels of chemical elements in the biosphere, which are essential for predictive assessments of the ecosystem's condition and the development of measures to prevent the worsening of the current level of ecological disaster or its improvement, have not been established.

The aim of the study and discussion of the results

The initial studies on the ecological-agrogeochemical conditions of soils were conducted from 2010 to 2012 by Ibragimov B., Jumamuratov A. (Zhumamuratov A., Ibragimov B. A., 2014; Zhumamuratov A., Zhumamuratov M. A., Sdykov I. M., Usmanov U., 2017). These studies demonstrated soil enrichment with Na, Cl, Zn, Cu, As, Sb, Se, Br, Hf, Ta, U, REE, while simultaneously observing a depletion of K, Sc, Mn, Fe, Co, Ba, Sr, and included a cartogram of Na distribution in the soils of the northern part (above Nukus) of Karakalpakstan. Subsequent observations of the ecological-agrogeochemical condition of soils at the same control points were continued by us in the following years – not only to assess the degree of soil contamination but also to establish other soil parameters. Soil samples were collected during 2017–2022.

Soil samples were collected from the arable layer of the Ellikkala district (Bostan farm) – moderately saline soils, and samples of highly saline soils in the Muynak district (vicinity of Muynak city) and the surroundings of Nukus city. Given that the Ellikkala district is located far from the Aral Sea (380 km) and, according to data (Zhumamuratov A., Ibragimov B. A., 2014), the soils of this district are less prone to salinization, this area was taken as a benchmark, and the data on the elemental composition of soils obtained from the other two districts were compared with Ellikkala. Let's examine these relationships, i.e., the comparison of the average content of elements in the soils of the Muynak (Cm) and Nukus (Cn) districts with the data for the Ellikkala (Ce) district. Soil samples were collected from the arable layer of the Ellikkala district (Bostan farm) – moderately saline soils, and samples of highly saline soils in the Muynak district (vicinity of Muynak city) and the surroundings of Nukus city. Given that the Ellikkala district is located far from the Aral Sea (380 km) and, according to data (Zhumamuratov A., Ibragimov B. A., 2014), the soils of this district are less prone to salinization, this area was taken as a benchmark, and the data on the elemental composition of soils obtained from the other two districts were compared with Ellikkala. Let's examine these relationships, i.e., the comparison of the average content of elements in the soils of the Muynak (Cm) and Nukus (Cn) districts with the data for the Ellikkala (Ce) district.

Sodium and potassium. The content of Na decreases from north to south in the sequence Muynak-Nukus-Ellikkala. The potassium content is highest (2.2%) in the soils surrounding Nukus and lowest in the soils of the Ellikkala district (1.1%). The high potassium content indicates that these soils have either not been used in agricultural rotation for a long time or are contaminated by uncontrolled application of potassium fertilizers (Fig. 1).

Iron, Manganese, Cobalt. For this group of elements, an enrichment of the soils in the Ellikkala district is observed. Compared with other areas, it is noted that the contents of Fe, Mn, Co in the soils are relatively low compared with other republics (Zhumamuratov A., Ibragimov B. A., 2014), and a deficiency of these elements can cause anemia and other diseases, i.e., the content is insufficient for the normal progression of metabolic processes in plants, animals, and humans (Tarmaeva I. Yu., Boeva A. V. 2014).

Scandium and REEs (La, Ce, Sm, Eu, Tb, Yb, Y). The biological role of this group of elements is not well understood, although these elements are always found in the composition of soils, plants, in the organs and tissues of animals and humans. The work (Tarmaeva I. Yu., Boeva A. V. 2014) demonstrates the involvement of these elements in the pathogenesis of cotton wilt, hepatitis, and diabetes in humans, in particular, a correlation was found between the content of scandium and the blood sugar levels in sick and healthy individuals. From table 1., it is

apparent that the soils of the Ellikkala district and the surroundings of Nukus and Muynak districts are enriched with these elements and are more evenly distributed within the limits of elemental determination errors. We tend to explain this situation by the fact that this group of elements is part of phosphate fertilizers, and their application has led to the contamination of the soils in this region (since within).

Table1. *Content of chemical elements in the arable layer of soils from characteristic regions of Karakalpakstan (mg/kg)*

	Ellikkala district	Muynak district		Nukus district		$\bar{C}$	$\bar{C}$ [3]	$\bar{C}/\bar{C}$ [3]
	Ce	Cm	$\bar{C}_м/\bar{C}_э$	$\bar{C}_н/\bar{C}_э$	$\bar{C}_н/\bar{C}_э$			
Na%	1.3	4.5	3.5	2.8	2.2	2.87	1.7	1.69
K%	1.1	1.58	1.43	2.2	2.0	1.63	1.8	0.91
Sc	11.5	7.3	0.60	9.8	0.8	9.54	7.8	1.22
Cr	46.7	25.8	0.50	55.0	1.1	24.3	75.3	0.32
Mn	624.0	450.0	0.72	496.8	0.80	523.6	434	1.21
Fe%	1.85	1.52	0.84	1.35	0.73	1.57	1.4	1.12
Co	11.7	8.2	0.70	9.84	0.86	9.91	8.9	1.11
Rb	35.9	50.9	1.42	41.2	1.15	56	52.7	1.06
Y	29.0	34.0	1.17	33.0	1.3	32	–	–
Zr	11.0	13.2	1.2	12.4	1.1	12.2	–	–
Sb	3.6	2.61	0.72	2.25	0.61	2.82	1.6	1.76
Cs	6.50	3.86	0.59	3.50	0.54	4.29	1.6	2.68
Ba	967.0	635.0	0.66	400.0	0.41	667.3	340	1.96
La	33.6	19.2	0.57	26.9	0.80	26.53	19	1.59
Ce	30.6	26.7	0.87	27.0	0.73	28.1	18.1	1.56
Sm	2.5	2.1	0.84	3.7	1.48	2.77	2.9	0.96
Eu	0.90	1.07	1.18	1.72	1.91	1.23	1.0	1.23
Tb	3.7	3.5	0.95	5.2	1.41	4.13	3.3	1.25
Yb	1.2	1.50	1.25	1.38	1.15	1.36	1.8	0.78
Hf	2.3	2.12	0.91	2.30	1.0	2.21	3.5	0.63
Th	5.2	4.88	0.94	6.3	1.21	5.7	5.3	1.1
U	2.82	2.60	0.93	2.1	0.75	2.51	2.1	1.2

Rubidium, Cesium, Barium. The elements of this group are analogs of Na, K, and Ca. Their content (except for Ba) is higher in the soils of the Muynak district, and slightly lower in the Nukus district. The enrichment of the soils in the Ellikkala district (967.0 mg/kg) with barium can be explained by a disturbance in the Ca/Ba or Mg/Ba ratio, which leads to the depletion of Ca or Mg in the soils and is associated with changes in the pH of the environment (pH-8.9), or the composition of humus in the soils.

Thorium and uranium. The maximum content of thorium was found in the arable layer of soils in the Nukus district (6.6 mg/kg), Ellikkala (5.2 mg/kg), and the minimum in the soils of the Muynak district (4.88 mg/kg). In the case of uranium, we see the opposite picture: Ellikkala (2.82 mg/kg), Muynak (2.60 mg/kg), Nukus (2.10 mg/kg). As will be shown in the next chapter, these elements, along with their natural component, also have anthropogenic components, hence here we find disturbances in their ratios, which are associated with the environmental

situation of the region. The average data we obtained for Th and U are 1.05 and 1.2 times higher, respectively, than the averages for (Karakalpakstan Zhumamuratov A., Ibragimov B. A., 2014). A slight increase in the content of these elements in the soils is observed.

Figure 1. *Comparative analysis from north to south following the scheme Muynak-Nukus-Ellikkala in the Republic of Karakalpakstan (Sodium and Potassium)*

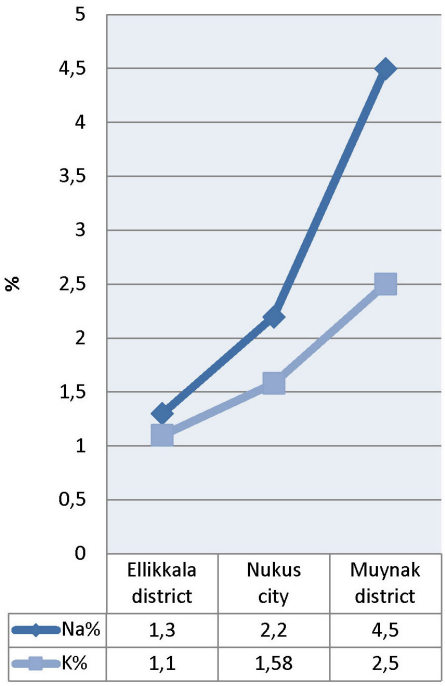

	Ellikkala district	Nukus city	Muynak district
Na%	1,3	2,2	4,5
K%	1,1	1,58	2,5

Antimony. The maximum content of antimony was found in the soils of the Ellikkala district (3.60 mg/kg), and the minimum in the soils around Nukus city (2.25 mg/kg). This element is a component of pesticides. The obtained results for antimony do not have an anthropogenic impact on the environment, although this statement requires further research on the participation of antimony in the biogeochemical cycle.

Comparative analysis of the results we obtained with the data presented in the work (Esimbetov A. T., Ametov Ya.I., Allamuratov K. K., 2018) shows that over 8–10 years (our samples were taken at the same points), the arable soil layer has been enriched with Na, Sc, Mn, Fe, Co, Rb, Sb, Cs, Ba, La, Ce, Eu, Tb, Th, U, and other chemical elements. In the soils of the designated sampling points to this day (with the exception of three out of seven sampling points in Muynak), cotton is still being cultivated. Therefore, the decrease in the content of K, Cr, Sm, Yb, Hf can be associated with their removal by cotton.

The process of enrichment with Na, Sb, Cs, Ba, La, Ce is linked to irrigation with saline water, the introduction of aerosol particles, the application of mineral fertilizers (in the case of REEs, Sc, Th, U), and due to the rise of groundwater levels to the surface, which contain high concentrations of many chemical elements (Table 1).

In principle, over 10 years, the content of chemical elements in the arable layer increased by 1.05–2.6 times. To establish the reliability of such a statement, it is necessary to conduct systematic research over time and space on a sufficiently large statistical basis, which is planned for the future.

Study results show, it should be noted that the content of many elements in the soils is small (with the exception of Na, K), and due to the alkaline reaction of the environment and the oxidative conditions, their mobility in the conditions of the Aral Sea region is low. Therefore, plants, animals, and humans may experience their deficiency, which is evident in the example of reduced soil productivity in the region.

Soil salinization has led to a quantitative and qualitative change in the pattern of migration of chemical elements in the biosphere of the region due to the reduction in the accumulation of bio-philic elements, disruption of the ratio between elements, and an increase in the proportion of toxicants in the soil. Therefore, studying the distribution pattern of a wide range of chemical elements across the soil profile is important in this regard.

References

Esimbetov A. T., Ametov Ya. I., Allamuratov K. K. (2018). Environmental Problems of the Aral Sea and the Aral Sea Region. Bulatov Readings, collection of articles. – P. 84–87.

Zhumamuratov A., Ibragimov B. A. (2014). Content of mangenese in irrigated soils of the Southern Aral Sea region // V International Scientific and Practical Conference “Problems

of rational use and protection of biological resources of the Southern Aral Sea region" Nukus, July 11–12, – P. 99–100.

Zhumamuratov A., Zhumamuratov M. A., Sdykov I. M., Usmanov U. (2017). Study of the background level of chemical elements and assessment of the ecological state of soils in Karakalpakstan // Journal of Ecological Systems and Instruments. – Moscow. – No. 1. – P. 4–6.

Tarmaeva I. Yu., Boeva A. V. (2014). Minerals, vitamins: their role in the body. Problems of micronutrient deficiency. Textbook Irkutsk IGMU – P. 36–46.

submitted 17.04.2025;
accepted for publication 01.05.2025;
published 29.05.2025

Contact: mirza.aj.1974@mail.ru; i.sdikov@yandex.ru

The Austrian Journal of Technical and Natural Sciences, No 5–6
ISSN 2310-5607

PREMIER Publishing
ppublishing.org

Section 5. Medical science

DOI:10.29013/AJT-25-5.6-91-96

CLINICAL ASPECTS OF THYROID DYSFUNCTION DURING COMBINED THERAPY FOR BREAST CANCER

Azimova Makhbuba Abrorjon qizi [1],
Nasirova Khurshidakhon Kudratullayevna [1]

[1] Tashkent Medical Univesity

Cite: *Azimova M.A., Nasirova Kh. K. (2025). Clinical Aspects of Thyroid Dysfunction During Combined Therapy For Breast Cancer. Austrian Journal of Technical and Natural Sciences 2024, No 5–6.* https://doi.org/10.29013/AJT-25-5.6-91-96

Abstract

Breast cancer is among the most prevalent cancers affecting women and often necessitates a multifaceted treatment approach. However, combined treatment methods such as chemotherapy and radiotherapy can negatively impact thyroid gland (TG) function, potentially causing hormonal imbalances. These thyroid issues can deteriorate a patient's general health, lower their ability to tolerate treatment, and possibly affect the effectiveness of therapy. In Uzbekistan, this area has not been thoroughly explored, emphasizing the importance of a detailed evaluation of thyroid function in women with BC.

Keywords: *breast cancer, chemotherapy, thyroid gland, thyroid dysfunction, anti-TPO antibodies, thyroid hormones, combined therapy*

Introduction

Breast cancer (BC) remains one of the most prevalent oncological conditions among women globally. According to data from the Republican Specialized Scientific and Practical Medical Center of Oncology and Radiology (RSSPMCOR) under the Ministry of Health of Uzbekistan, a total of 4,757 new cases of BC were reported in 2024, with 86.7% of these diagnosed at stages II–IV, necessitating intensive multimodal treatment approaches. In recent years, growing attention has been directed toward the effects of anticancer therapies on the endocrine system, particularly the thyroid gland.

Thyroid dysfunction observed in oncology patients may arise as a consequence of therapeutic interventions or may reflect pre-existing, undiagnosed thyroid abnormalities prior to the initiation of cancer treatment. The development of hypothyroidism in this context has the potential to adversely influence the clinical trajectory of BC, diminish patient tolerance to treatment, and negatively impact overall quality of life.

The primary aim of the present study was to evaluate the effects of different combined

treatment modalities for BC on both clinical and laboratory indicators of thyroid gland function.

Materials and Methods

The study included 136 female patients with histologically confirmed BC treated at RSSPMCOR and its regional branches between 2023 and 2025. Patients' ages ranged from 30 to 73 years (mean 56.3 ± 0.4 years).

Patients were divided into three groups:

- Group 1 (n=52): Stage II BC, treatment consisted of surgery plus 6–8 courses of chemotherapy without neoadjuvant treatment;
- Group 2 (n=64): Stage II–III BC, neoadjuvant and adjuvant chemotherapy;
- Group 3 (control, n = 20): Stage I BC, no chemotherapy.

Previous studies have reported the prevalence of anti-thyroid peroxidase antibodies (anti-TPO) in patients with BC to be approximately 34%, compared to 36% in control populations. Based on an estimated effect size of 0.55, a significance level of 5%, and a statistical power of at least 80%, the minimum required sample size was determined to be 20 participants in the control group and 93 in the experimental (BC) group.

All participants provided written informed consent prior to enrollment, and the study protocol was reviewed and approved by the institutional Ethics Committee.

The research protocol encompassed comprehensive clinical and laboratory evaluations, along with instrumental diagnostic procedures including ultrasound, magnetic resonance imaging (MRI), and positron emission tomography-computed tomography (PET-CT). Thyroid function was assessed through measurements of serum thyroid-stimulating hormone (TSH), total triiodothyronine (T3), free thyroxine (T4), luteinizing hormone (LH), and follicle-stimulating hormone (FSH), in addition to thyroid ultrasound imaging.

Reference ranges for thyroid hormones were:

- TSH: 0.5–4.5 μIU/mL;
- Total T3: 80–200 pg/mL;
- Free T4: 4–12 ng/mL;
- Anti-TPO levels > 40 IU/mL were considered positive.

Statistical Analysis

Data were analyzed using SPSS v.19.

Normality was assessed by the Kolmogorov-Smirnov test.

Group comparisons employed Student's t-test for normally distributed data,

Mann-Whitney U test for nonparametric data,

Chi-square and Fisher's exact test for contingency tables.

Statistical significance was set at $p < 0.05$.

Results

Clinical manifestations:

- The most frequently observed symptoms of thyroid dysfunction during the post-chemotherapy period included general weakness (88.9%), palpitations (up to 31.1%), neck discomfort (up to 37.8%), and a sense of a lump during swallowing (up to 26.5%). In contrast, these clinical manifestations were largely absent in the control group.

Laboratory findings:

- TSH, T3, and T4 levels were assessed at three time points: prior to the initiation of chemotherapy, one month following its completion, and six months post-treatment. Alterations in thyroid hormone profiles were identified in 78.7% of patients, with subclinical hypothyroidism being the most prevalent abnormality. Additionally, elevated levels of cholesterol and triglycerides were observed, suggesting a potential link between thyroid dysfunction and the development of metabolic syndrome during chemotherapy.
- While no statistically significant difference in TSH levels was observed between the patient and control groups ($p = 0.166$), significant intergroup differences were noted for mean free T4 ($p = 0.001$), total T3 ($p < 0.017$), and anti-thyroid peroxidase antibodies (anti-TPO) ($p = 0.05$). Further analysis using Chi-square and Fisher's exact tests confirmed significant differences between groups for T3 ($p = 0.017$) and anti-TPO ($p = 0.044$), whereas no significant differences

were found for TSH (p = 0.34) or free T4 (p = 0.14).

Ultrasound and imaging studies:

Thyroid ultrasound examinations were conducted using 5 MHz convex transducers positioned perpendicular to the midline of the neck, enabling evaluation of the thyroid gland's structure, volume, and dimensions throughout the course of BC chemotherapy. Thyroid volume was calculated using the A. F. Tsyba formula (1990):

$$V = 0.52 \times A \times B \times C \ (sm^3)$$

where:

- *A* represents the length of the thyroid lobe;
- *B* – is the thickness, and
- *C* – is the width measured in the transverse plane.

When indicated, Doppler mapping was employed to assess vascularization and characterize nodular formations.

MRI of the thyroid, using T1-weighted sequences, was performed in 53 patients to detect structural abnormalities. Additionally, PET-CT using 18F-fluorodeoxyglucose (18F-FDG) was employed for disease staging and to evaluate thyroid metabolic activity based on radiotracer uptake.

Patients were instructed to fast for 12 hours prior to receiving an intravenous injection of 18F-FDG at a dose of 200 MBq/m² (total dose ranging from 370 to 420 MBq). Following a 60–90 minute uptake phase, patients were encouraged to consume up to 500 mL of water and to void the bladder in order to reduce background radiotracer activity. A preliminary CT scan was performed to define the anatomical region for PET imaging, and established synchronization protocols were applied for accurate PET-CT data alignment.

Statistical Analysis of the Material

The data obtained in the study were statistically analyzed using SPSS version 16.0 (USA). The degree of statistical significance for various comparative parameters was determined accordingly. Parametric data were reported as means ± standard deviations (SD), while non-parametric data were expressed as medians with interquartile ranges (Q1–Q3). Independent samples were analyzed using the Mann–Whitney U-test for non-parametric variables. Categorical variables were evaluated using the Chi-square test and Fisher's exact test. A p-value less than 0.05 was considered indicative of statistical significance. Differences in mean values between groups were assessed using the Student's *t*-test and Fisher's exact test.

To compare long-term (5-year) outcomes of different treatment modalities based on survival stratification, the actuarial life table method – specifically the "Lise-Table method" developed by Cutler S. J. and Ederer F. and endorsed by the Union for International Cancer Control (UICC)—was employed.

Patient survival was further analyzed using the Kaplan–Meier method, applying the formula:

$$s(t)=N\times(1-d_1/n_{10})$$

where *s(t)* represents the survival probability at time *t*, d_1 the number of events (deaths) at that time, and n_{10} the number of individuals at risk.

Median durations of disease-free and metastasis-free intervals were determined according to the methodology proposed by D. Collett (1999).

Discussion

Our study confirms a high prevalence of thyroid dysfunction among BC patients undergoing combined therapeutic regimens. This aligns with previous research linking thyroid disorders – such as nodular hyperplasia, hyperthyroidism, autoimmune thyroiditis, and elevated anti-TPO antibody levels – to breast cancer pathophysiology (Turken O., NarIn Y., DemIrbas S., Onde M. E., Sayan O., KandemIr E. G., 2003; Agarwal D. P., Soni T. P., Sharma O. P., Sharma S., 2007; Giustarini E., Pinchera A., Fierabracci P., Roncella M., Fustaino L., Mammoli C., 2006). Several studies have reported associations between BC and various thyroid-related biomarkers, including anti-TPO, TSH, T3, T4, and estradiol levels (Fierabracci P., Pinchera A., Campani D., Pollina L. E., Giustarini E., Giani C. 2006; Sabitha Suneetha, Mohanty S, Rao P., 2009; Ali A., Mir M. R., Bashir S., Hassan T., Bhat S. A., 2011; Smyth P. P., Shering S. G., Kilbane M. T., Murray M. J., McDermott E. W., Smith D. F., 2017; (Fierabracci P., Pinchera A., Campani D., Pollina L. E., Giustarini E., Giani C., 2006; Sabitha Suneetha, Mohanty S, Rao P., 2009; Ali A., Mir M. R., Bashir S., Hassan T., Bhat S. A., 2011; Smyth P. P., Shering S. G., Kilbane M. T.,

Murray M. J., McDermott E. W., Smith D. F., 2017; Ditsch N., Liebhardt S., Von Koch F., Lenhard M., Vogeser M., Spitzweg C., 2010).

In our cohort, BC patients exhibited significantly elevated anti-TPO (p=0.011) and free T4 (p=0.001) levels compared to controls, while total T3 levels were significantly reduced (p=0.001), and TSH levels were lower but not statistically significant (p=0.166). These findings are consistent with prior literature (Ali A., Mir M. R., Bashir S., Hassan T., Bhat S. A., 2011; Wang G., Chen X-S., Mao Y., Li Y-F., Chen W-G., Shen K-W., 2014; Takatani O., Okumoto T., Kosano H., Nishida M., Hiraide H., Tamakuma S., 1989; Kuijpens J. L., Nyklictek I., Louwman M. W., Weetman T. A., Pop V. J., Coebergh J. W., 2005; Saraiva P., Figueiredo N., Padovani C., Brentani M., Nogueira C., 2005; Rose D. P., Davis T. E., 1979), reinforcing the hypothesis that thyroid dysfunction – potentially driven by autoimmune mechanisms – may influence BC development and progression.

One proposed mechanism involves the estrogen-mimetic action of thyroid hormones and their receptors in modulating cellular proliferation and differentiation (Tosovic A., Bondeson A. G., Bondeson L., Ericsson U. B., Malm J., Manjer J., 2010). Notably, the ratio of free T3 to free T4 has been suggested as a potential tumor biomarker (Ditsch N., Liebhardt S., Von Koch F., Lenhard M., Vogeser M., Spitzweg C., 2010). Some studies have associated elevated free T4 levels with increased BC risk, whereas higher anti-TPO antibody levels may exert a protective effect (Wang G., Chen X-S., Mao Y., Li Y-F., Chen W-G., Shen K-W., 2014; Cengiz O., Bozkurt B., Unal B., Yildirim O., Karabeyoglu M., Eroglu A. 2004; Tosovic A., Becker C., Bondeson A. G., Bondeson L., Ericsson U. B., Malm J., 2012). Additionally, thyroid dysfunction has been reported to correlate with higher tumor grades, suggesting a relationship with malignancy severity (Lemaire M., Baugnet-Mahieu L., 1986).

However, other investigations have failed to identify significant associations between thyroid disorders and BC risk (Michalaki V., Kondi-Pafiti A., Gennatas S., Antoniou A., Primetis H., Gennatas C., 2009; Kuijpens J. L., Nyklictek I., Louwman M. W., Weetman T. A., Pop V. J., Coebergh J. W., 2005). These discrepancies may reflect methodological variability, differences in population characteristics, variability in assay sensitivity, or racial and geographic influences.

An interesting observation from our study was a non-significant trend toward reduced symptoms of thyroid dysfunction in patients receiving prophylactic levothyroxine. Although this finding lacked statistical significance, it suggests a potential benefit that warrants further exploration through randomized controlled trials with larger sample sizes.

In conclusion, the observed associations between thyroid dysfunction and breast cancer highlight the need for comprehensive endocrine assessment in this patient population. Future prospective studies employing standardized methodologies and larger cohorts are essential to clarify the clinical implications and to explore the potential role of thyroid hormone modulation in BC management.

Conclusions

1. Combined antitumor therapy for BC is associated with a high incidence of thyroid dysfunction, mainly subclinical hypothyroidism, especially in patients receiving neoadjuvant and adjuvant chemotherapy.
2. Common clinical manifestations of post-chemotherapy thyroid dysfunction include general weakness, palpitations, neck discomfort, and difficulty swallowing.
3. Significant hormonal changes involve free T4, total T3, and anti-TPO levels, indicating autoimmune involvement in the pathological process.
4. Ultrasound and radionuclide imaging (PET-CT) reveal structural-functional thyroid alterations correlating with treatment intensity.
5. Preliminary data suggest potential benefits of prophylactic thyroid hormone (levothyroxine) to mitigate thyroid dysfunction symptoms, requiring further randomized trials.
6. Due to the high prevalence and clinical relevance of thyroid dysfunction during BC treatment, routine thyroid status assessment is recommended in oncological patient management protocols.

Rseferences

Jemal A., Bray F., Center M.M., Ferlay J., Ward E., Forman D. (2011). Global cancer statistics. CA Cancer J Clin; – 61: 69–90.
Shering S. G., Zbar A. P., Moriarty M., Mc Dermott E. W., O'Higgins N.J., Smyth P. P. (1996). Thyroid disorders and breast cancer. Eur J Cancer Prev; – 5: 504–506.
Giani C., Fierabracci P., Bonacci R., Gigliotti A., Campani D., De Negri F. (1996). Relationship between breast cancer and thyroid disease: relevance of autoimmune thyroid disorders in breast malignancy. J Clin Endocrinol Metab; – 81: 990–994.
Clarke R., Dickson R. B., Brunner N. (1990). The process of malignant progression in human breast cancer. Ann Oncol; – 1: 401–407.
Gogas J., Kouskos E., Tseleni-Balafouta S., Markopoulos C., Revenas K., Gogas G. (2001). Autoimmune thyroid disease in women with breast carcinoma. Eur J Surg Oncol; – 27: 626–630.
Turken O., NarIn Y., DemIrbas S., Onde M. E., Sayan O., KandemIr E. G. (2003). Breast cancer in association with thyroid disorders. Breast Cancer Res; – 5: 110–113.
Perry M., Goldie D. J., Self M. (1978). Thyroid function in patients with breast cancer. Ann R Coll Surg Engl; – 60: 290–293.
Smyth P. P. (2003). The thyroid, iodine and breast cancer. Breast Cancer Res; – 5: 235–238.
Vorherr H. (1978). Thyroid disease in relation to breast cancer. Klin Wochenschr; – 56: 1139–1145.
Saraiva P., Figueiredo N., Padovani C., Brentani M., Nogueira C. (2005). Profile of thyroid hormones in breast cancer patients. Braz J Med Biol Res; – 38: 761–765.
Smyth P. Thyroid disease and breast cancer. J Endocrinol Invest 1993; 16: 396–401.
Agarwal D. P., Soni T. P., Sharma O. P., Sharma S. (2007). Synchronous malignancies of breast and thyroid gland: a case report and review of literature. J Cancer Res Ther; – 3: 172–173.
Fierabracci P., Pinchera A., Campani D., Pollina L. E., Giustarini E., Giani C. (2006). Association between breast cancer and autoimmune thyroid disorders: no increase of lymphocytic infiltrates in breast malignant tissues. J Endocrinol Invest; 29: 248–251.
Giustarini E., Pinchera A., Fierabracci P., Roncella M., Fustaino L., Mammoli C. (2006). Thyroid autoimmunity in patients with malignant and benign breast diseases before surgery. Eur J Endocrinol; – 154: 645–649.
Sabitha Suneetha, Mohanty S., Rao P. (2009). Serum anti-TPO levels in benign and malignant breast tumors. Indian J Clin Biochem; – 24: 266–268.
Ali A., Mir M. R., Bashir S., Hassan T., Bhat S. A. (2011). Relationship between the levels of serum thyroid hormones and the risk of breast cancer. J Biol Agric Health; – 1: 56–59.
Smyth P. P., Shering S. G., Kilbane M. T., Murray M. J., McDermott E. W., Smith D. F. (2017). Serum thyroid peroxidase autoantibodies, thyroid volume, and outcome in breast carcinoma. J Clin Endocrinol Metab 1998; – 83: 2711–2716. Motie/Taheri/Noorian 8628 Biomed Res – Vol. 28. – Issue 20.
Ditsch N., Liebhardt S., Von Koch F., Lenhard M., Vogeser M., Spitzweg C. (2010). Thyroid function in breast cancer patients. Anticancer Res; – 30: 1713–1717.
Michalaki V., Kondi-Pafiti A., Gennatas S., Antoniou A., Primetis H., Gennatas C. (2009). Breast cancer in association with thyroid disorders. J Buon; – 14: 425–428.
Wang G., Chen X-S., Mao Y., Li Y-F., Chen W-G., Shen K-W. (2014). Patients with breast cancer have a higher level of serum free thyroxine (T4) compared with those with benign breast diseases. Tumor; – 34: 366–369.
Takatani O., Okumoto T., Kosano H., Nishida M., Hiraide H., Tamakuma S. (1989). Relationship between the levels of serum thyroid hormones or estrogen status and the risk of breast cancer genesis in Japanese women. Cancer Res; – 49: 3109–3112.
Kuijpens J. L., Nyklictek I., Louwman M. W., Weetman T. A., Pop V. J., Coebergh J. W. (2005). Hypothyroidism might be related to breast cancer in post-menopausal women. Thyroid; – 15: 1253–1259.

Saraiva P., Figueiredo N., Padovani C., Brentani M., Nogueira C. (2005). Profile of thyroid hormones in breast cancer patients. Brazil Med Biol Res; – 38: 761–765.
Rose D. P., Davis T. E. (1979). Plasma triiodothyronine concentrations in breast cancer. Cancer; – 43: 1434–1438.
Tosovic A., Bondeson A. G., Bondeson L., Ericsson U. B., Malm J., Manjer J. (2010). Prospectively measured triiodothyronine levels are positively associated with breast cancer risk in postmenopausal women. Breast Cancer Res; – 12: 33.
Cengiz O., Bozkurt B., Unal B., Yildirim O., Karabeyoglu M., Eroglu A. (2004). The relationship between prognostic factors of breast cancer and thyroid disorders in Turkish women. J Surg Oncol; – 87: 19–25.
Tosovic A., Becker C., Bondeson A. G., Bondeson L., Ericsson U. B., Malm J. (2012). Prospectively measured thyroid hormones and thyroid peroxidase antibodies in relation to breast cancer risk. Int J Cancer; – 131: 2126–2133.
Lemaire M., Baugnet-Mahieu L. (1986). Thyroid function in women with breast cancer. Eur J Cancer Clin Oncol; – 22: 301–307.

Sources of funding: *The work did not receive any specific funding.*

Conflict of interest: *The authors declare no explicit or potential conflicts of interest associated with the publication of this article.*

Contribution of the authors:

Azimova A. Makhbuba – writing the text; editing the article;

Nasirova K. Khurshida – ideological concept of the work, editing the article

submitted 17.04.2025;
accepted for publication 01.05.2025;
published 29.05.2025

Contact: azimovamakhbuba@gmail.com; hursh77@mail.ru

The Austrian Journal of Technical and Natural Sciences, No 5–6
ISSN 2310-5607

PREMIER Publishing
ppublishing.org

DOI:10.29013/AJT-25-5.6-97-100

PREDICTIVE ROLE OF CD4⁺ T-LYMPHOCYTES IN TREATMENT RESPONSE OF SOFT TISSUE SARCOMAS

Polatova Jamila Shagayratovna [1], ***Karimova Nargiza Mansurovna*** [1], ***Kahharov Alisher Jamoliddinovich*** [1]

[1] Department of Oncology and Medical Radiology, Tashkent State Dental Institute, Tashkent, Uzbekistan

Cite: *Polatova J. Sh., Karimova N. M., Kahharov A.J. (2025). Predictive Role of Cd4⁺ T-Lymphocytes in Treatment Response of Soft Tissue Sarcomas. Austrian Journal of Technical and Natural Sciences 2024, No 5–6.* https://doi.org/10.29013/AJT-25-5.6-97-100

Abstract

This study highlights the particular importance of CD4 T-lymphocyte levels in the immune microenvironment of soft tissue sarcomas. Data analysis shows that high levels of active CD4⁺ T-lymphocytes inside the tumor are associated with more favorable morphological responses to therapy, as well as improved clinical outcomes. CD4 levels serve as a promising prognostic marker and can contribute to more accurate prediction of the results of complex treatment, including immunotherapy. The obtained results emphasize the need for expanded research to develop new individualized strategies to enhance the immune response and improve the effectiveness of soft tissue sarcoma therapy.

Keywords: *soft tissue sarcoma, tumor microenvironment, chemotherapy, radiation therapy*

Introduction

The relevance of the study is due to the high heterogeneous nature of soft tissue sarcomas and their complexity in diagnosis and treatment, which is confirmed by numerous international studies. According to modern data, soft tissue sarcomas constitute about 1% of all malignant tumors and are characterized by a high degree of morphological and molecular diversity, which complicates not only the diagnosis but also the selection of optimal therapy (Huang H., Fan Y., Zhang S., Bai X., Wang X., Shan F., 2025). These tumors are characterized by high aggressiveness, a high risk of recurrence, and low patient survival rates, especially in advanced stages of the disease. In the context of modern trends in global oncology, the role of the tumor's immune microenvironment and its components, primarily the activity of T-lymphocytes with the CD4 marker, which perform regulatory and supporting functions in the antitumor immune response, is gaining particular importance. International studies show that the presence of active CD4⁺ T-lymphocytes within the tumor tissue is associated with improved prognosis, reduced metastasis risk, and higher tumor sensitivity to immunotherapeutic approaches (Van der Graaf W.T.A., Orbach D., Judson I. R., Ferrari A., 2017).

An additional factor is that the activity of CD4⁺ cells contributes to the activation of

cytotoxic T-lymphocytes and macrophages, increased cytokine synthesis, and the development of an immunological microenvironment favorable for the elimination of tumor cells. In light of the rapid implementation of immunotherapy as an innovative method in oncological practice, understanding the role of $CD4^+$ T-lymphocytes as a prognostic and predictive marker is becoming particularly relevant. The introduction of an assessment of the immune status, in particular the level of CD4, can contribute to a more accurate prediction of treatment outcomes, the selection of personalized therapeutic regimens, and the development of new combined methods that enhance the antitumor immune response (Lee A. Q., Hao C., Pan M., Ganjoo K. N., Bui N., 2024).

Thus, the study and assessment of the role of CD4-lymphocytes in the microenvironment of soft tissue sarcomas is a crucial area contributing to increased treatment efficacy, reduced risk of relapses, and increased life expectancy. These tasks correspond to the current global trends in the development of oncology and require further scientific research to confirm and implement them in clinical practice (Wood G. E., Meyer C., Petitprez F., D'Angelo S.P., 2024; Recine F., Vanni S., Bongiovanni A., Fausti V., Mercatali.L, Miserocchi G., et al., 2024).

Materials and methods

The study was conducted at the Children's Oncology, Hematology and Immunology Scientific and Practical Medical Center, as well as the Republican Specialized Scientific and Practical Medical Center of Oncology and Radiology and its Tashkent City Branch, in the period from 2014 to 2024. 174 patients diagnosed with rhabdomyosarcoma of various localizations participated in the study.

Inclusion criteria: diagnosis of soft tissue sarcoma, availability of data on chemotherapy and material for immunohistochemical analysis. Patients with preliminary immunotherapy or insufficient volume of biopsy material were excluded.

To assess the immune microenvironment, tumor tissue samples obtained by biopsy were used. The samples were fixed in 10% formalin and enclosed in paraffin. 4 μm thick sectional cuts were stained using antibodies to determine the status of CD4, CD8, CD20, and CD68. The results of the pathohistological examination were evaluated by two independent pathologists. Assessment of the location of immune cell infiltration was carried out by dividing the samples into intratumoral and peritumoral zones. Cell counting was performed in 5 independent fields of view using microscopy. The results were recorded as the percentage of positive cells from the total number of cells in the visual field.

To analyze the differences in the level of infiltration and response to chemotherapy, Pearson's chi square and Fisher's precision criteria were used. The significance level was established at $p<0.05$. All calculations were carried out using statistical software.

This approach provided a detailed assessment of the immune microenvironment and its impact on clinical outcomes in patients with soft tissue sarcomas.

Results

An analysis of the therapy effectiveness was conducted depending on the CD4 status.

Table 1. *Analysis of therapy effectiveness depending on CD 4 status*

Indicators	Category	CD 4 Status		p
		negative status	positive status	
Chemotherapy effect (complete-1, partial-2, stabilization-3, progression-4)	Full effect	7 (10.0)	15 (17.2)	0.320
	Partial effect	28 (40.0)	37 (42.5)	
	Stabilization	32 (45.7)	29 (33.3)	
	Progression	3 (4.3)	6 (6.9)	
Degree of therapeutic pathomorphosis	therapeutic pathomorphosis I	21 (30.0)	11 (12.6)	0.002*

Indicators	Category	CD 4 Status		p
		negative status	positive status	
Radiation therapy response	therapeutic pathomorphosis II	31 (44.3)	28 (32.2)	0.253
	therapeutic pathomorphosis III	10 (14.3)	26 (29.9)	
	therapeutic pathomorphosis IV	8 (11.4)	22 (25.3)	
	Full effect	6 (15.8)	12 (16.9)	
	Partial effect	20 (52.6)	25 (35.2)	
	Stabilization	6 (15.8)	22 (31.0)	
	Progression	6 (15.8)	12 (16.9)	

** – differences in indicators are statistically significant ($p < 0.05$)*

Analysis of the presented data shows that there is a statistically significant correlation ($p = 0.002$) between the status of CD4 and the effectiveness of therapy, in particular, the degree of therapeutic pathomorphosis. This indicates that the presence of a positive CD4 status (presence of active T-lymphocyte helpers) contributes to more pronounced morphological regression of the tumor and, possibly, a more effective response to the ongoing treatment. Positive CD4 status apparently reflects the body's more active immune response, which contributes to a decrease in tumor mass and an increase in therapeutic effect.

At the same time, the influence of the CD4 status on the clinical response, measured by signs of complete, partial, stabilizing effect and progression, was not revealed, since no statistically significant differences in this indicator ($p = 0.320$) were recorded. This indicates that macroscopic effectiveness and morphological pathomorphism can be more sensitive to the immune status than the clinical response in terms of symptomatic or hormonal improvement.

Theoretically, a positive CD4 status contributes to the enhancement of phagocytic and stimulatory functions of immune cells, activates the cytokine mechanism, promotes the development of anti-tumor T-lymphocytes, which together enhances the anti-tumor immune response. This promotes more pronounced regression of tumor tissues under the influence of treatment, including radiation therapy. At the same time, the absence of significant differences in the effects of radiation therapy in different CD4 states can be explained by the fact that the immune system plays a role more as an auxiliary component in the context of radiation therapy, while the main effect is due to radiation load.

Summarizing, it can be said that the presence of a positive CD4 status is an important biological factor predisposing to more effective morphological regression of the tumor, which confirms the active role of the immune mechanism in the treatment of sarcomas. These data indicate the need for further research to clarify the precise mechanisms of interaction between immune cells and radiotherapy and to find immunological markers capable of predicting treatment outcomes and developing new approaches to immunoradiotherapy.

Conclusion

The presence of a positive CD4 status is associated with more pronounced morphological regression of the tumor and a high level of therapeutic pathomorphosis, which indicates the important role of T-helper lymphocytes in enhancing the anti-tumor effect in the treatment of soft tissue sarcomas. However, the influence of CD4 status on the clinical response (complete, partial, stabilization, progression) has not been established, which may indicate more complex mechanisms of immune system interaction and treatment effectiveness. These

data indicate the need for further research to understand the role of immune cells and their potential in predicting and improving sarcoma therapy.

References

Huang H., Fan Y., Zhang S., Bai X., Wang X., Shan F. (2025). Emerging immunotherapy and tumor microenvironment for advanced sarcoma: a comprehensive review. Front Immunol. May 21;16:1507870. Doi: 10.3389/fimmu.2025.1507870. PMID: 40469285; PMCID: PMC12133756

Van der Graaf W.T.A., Orbach D., Judson I.R., Ferrari A. (2017). Soft tissue sarcomas in adolescents and young adults: A comparison with their paediatric and adult counterparts. Lancet Oncol. 18: e166-e75. Doi: 10.1016/s1470-2045(17)30099-2

Lee A.Q., Hao C., Pan M., Ganjoo K.N., Bui N. (2024). Use of histologic and immunologic factors in sarcoma to predict response rates to immunotherapy. J Clin Oncol. 42:11569. Doi: 10.1200/JCO.2024.42.16_suppl.11569

Wood G.E., Meyer C., Petitprez F., D'Angelo S.P. (2024). Immunotherapy in sarcoma: current data and promising strategies. Am Soc Clin Oncol Educ Book. 44: e432234. Doi: 10.1200/edbk_432234

Recine F., Vanni S., Bongiovanni A., Fausti V., Mercatali.L, Miserocchi G., et al. (2024). Clinical and translational implications of immunotherapy in sarcomas. Front Immunol. 15:1378398. Doi: 10.3389/fimmu.2024.1378398

Sources of funding: *The work did not receive any specific funding.*

Conflict of interest: *The authors declare no explicit or potential conflicts of interest associated with the publication of this article.*

Contribution of the authors:

Polatova D.Sh. – ideological concept of the work, writing the text; editing the article;

Karimova N.M. – collection and analysis of literature sources, writing the text;

Kahharov A.J. – assistance in text correction

submitted 17.04.2025;
accepted for publication 01.05.2025;
published 29.05.2025

Contact: polatova.dj@gmail.com; karimovanargiza939@gmail.com;
djumaniyazova.gulnoza@bk.ru

The Austrian Journal of Technical and Natural Sciences, No 5–6
ISSN 2310-5607

PREMIER Publishing
ppublishing.org

DOI:10.29013/AJT-25-5.6-101-105

IMPACT OF CD4+ LYMPHOCYTE DISTRIBUTION ON THE IMMUNE MICROENVIRONMENT, MORPHOLOGICAL CHANGES, AND THERAPEUTIC OUTCOMES IN SOFT TISSUE SARCOMAS

Polatova Jamila Shagayratovna [1], ***Karimova Nargiza Mansurovna*** [1], ***Kahharov Alisher Jamoliddinovich*** [1]

[1] Department of Oncology and Medical Radiology, Tashkent State Dental Institute, Tashkent, Uzbekistan

Cite: *Polatova J. Sh., Karimova N. M., Kahharov A.J. (2025). Impact Of CD4+ Lymphocyte Distribution on the Immune Microenvironment, Morphological Changes, and Therapeutic Outcomes in Soft Tissue Sarcomas. Austrian Journal of Technical and Natural Sciences 2024, No 5–6.* https://doi.org/10.29013/AJT-25-5.6-101-105

Abstract

This study examines the significance of CD4 lymphocyte localization in the tumor microenvironment of soft tissue sarcomas and their impact on the efficacy of therapy. The analysis showed that intratumoral (intra-umoral) infiltration of these cells is significantly associated with pronounced morphological regression and a high level of therapeutic pathomorphosis, indicating the important role of immune mechanisms in the formation of an antitumor response. Localization of CD4+ T lymphocytes inside the tumor enhances the immune response, stimulates cytotoxic cells and helps to reduce tumor volume, which confirms the theoretical concept of strengthening local immune activation to improve treatment efficacy. At the same time, the effect of CD4 lymphocyte localization on short-term clinical indicators of responses to therapy (complete, partial, stabilization, progression) was statistically insignificant, which indicates the need for further research for a deeper understanding of the mechanisms of interaction between immune cells and the therapeutic effect. The data obtained emphasize the prospects of using CD4 lymphocyte localization as a prognostic marker for assessing the morphological and long-term response, as well as for the development of new methods for optimizing immunotherapy for soft tissue sarcomas.

Keywords: *soft tissue sarcoma, tumor microenvironment, chemotherapy, radiation therapy*

Introduction

The rapid development of areas in oncology, especially the active study of the role of the tumor's immune microenvironment as a key factor influencing the progression, response to treatment, and prognosis of patients, necessitates the relevance of the study. According to modern international data, soft tissue sarcomas are a heterogeneous group of malignant tumors, comprising more than 50 histological subtypes united by a common term. These tumors constitute approximately 1% of all malignant neoplasms and are characterized by high morphological and molecular diversity,

which makes diagnosis, selection of effective therapy, and prediction of clinical outcomes difficult (Huang H., Fan Y., Zhang S., Bai X., Wang X., Shan F., 2025).

Numerous studies show that in soft tissue sarcomas, the immune microenvironment plays a significant role, and the specific status of active immune cells within the tumor is a predictor of therapeutic outcomes and long-term prognosis. A particularly significant factor is the localization and activity of CD4+ T-lymphocytes, which perform regulatory and supporting functions in anti-tumor immunity, activating cytotoxic T-lymphocytes and enhancing the body's immune response. These cells participate in the regulation of immune mechanisms and the creation of an immunoactive microenvironment, which contributes to more pronounced morphological regression of the tumor (Van der Graaf WTA., Orbach D., Judson I. R., Ferrari A., 2017.

In the context of the introduction and widespread use of immune methods of cancer treatment, such as control point inhibitors, the study of the role and localization of CD4+ T-lymphocytes within tumor structures is becoming particularly relevant. International studies confirm that active $CD4^+$ lymphocytes within the tumor tissue are associated with more favorable outcomes, less recurrence, and increased survival. However, the role of their localization – within the tumor (intra-umoral infiltration) or around it (peritumoral infiltration) – has not been fully studied and requires additional evidence (Lee A. Q., Hao C., Pan M., Ganjoo K. N., Bui N., 2024).

Thus, the relevance of the study is especially high in light of the need to improve the accuracy of diagnosis and prognosis of treatment for soft tissue sarcomas, the prospects of implementing immunological markers for personalized treatment, as well as the development of new combined therapeutic strategies that increase the effectiveness and resistance of treatment. These tasks correspond to global standards and trends in the field of oncology and require further research to optimize the diagnosis, treatment, and prevention of relapses, which determines the scientific and practical relevance of this work (Wood G. E., Meyer C., Petitprez F., D'Angelo S. P., 2024; Recine F., Vanni S., Bongiovanni A., Fausti V., Mercatali L., Miserocchi G., et al., 2024).

Materials and methods

The study was conducted at the Children's Oncology, Hematology and Immunology Scientific and Practical Medical Center, as well as the Republican Specialized Scientific and Practical Medical Center of Oncology and Radiology and its Tashkent City Branch, in the period from 2014 to 2024. 174 patients diagnosed with rhabdomyosarcoma of various localizations participated in the study.

Inclusion criteria: diagnosis of soft tissue sarcoma, availability of data on chemotherapy and material for immunohistochemical analysis. Patients with preliminary immunotherapy or insufficient volume of biopsy material were excluded.

Tumor tissue samples obtained by biopsy were used to assess the immune microenvironment. The samples were fixed in 10% formalin and enclosed in paraffin. 4 μm thick sectional cuts were stained using antibodies to determine the status of CD4, CD8, CD20, and CD68. The results of the pathohistological examination were evaluated by two independent pathologists.

Assessment of the localization of immune cell infiltration was carried out by dividing the samples into intratumoral and peritumoral zones. Cell counting was performed in 5 independent fields of view using microscopy. The results were recorded as the percentage of positive cells from the total number of cells in the visual field.

To analyze the differences in the level of infiltration and response to chemotherapy, Pearson's chi square and Fisher's precision criteria were used. The significance level was established at $p<0.05$. All calculations were carried out using statistical software.

This approach provided a detailed assessment of the immune microenvironment and its impact on clinical outcomes in patients with soft tissue sarcomas.

Results

We analyzed the effectiveness of therapy depending on the location of CD4 lymphocytes in the tumor stroma or parenchyma.

A statistically significant difference ($p = 0.020$) was revealed when analyzing the relationship between the degree of pathomorphism and the localization of CD4 lymphocytes. In particular, in intratumoral

infiltration, cases of low-grade pathomorphosis are more pronounced, while in peritumoral infiltration, more pronounced changes (grade II and higher) are more frequently recorded. This suggests that the activity of CD4 lymphocytes, localized within tumor structures, can play a more significant role in tumor regression, contributing to a more pronounced morphological response, higher pathomorphism.

Table 1. *Analysis of therapy effectiveness depending on location*

Indicators	Category	localization (intratumor-1, peritumor-2)			p
		intratumoral infiltration	peritumoral infiltration	Indicator 3.	
Chemotherapy effect (complete-1, partial-2, stabilization-3, progression-4)	Full effect	3 (6.8)	12 (18.8)	4 (12.5)	
	Partial effect	17 (38.6)	23 (35.9)	17 (53.1)	
	Stabilization	22 (50.0)	27 (42.2)	7 (21.9)	
	Progression	2 (4.5)	2 (3.1)	4 (12.5)	0.071
Degree of therapeutic pathomorphosis	therapeutic pathomorphosis I	14 (31.8)	7 (10.9)	6 (18.8)	0.020* intratumoral infiltration – peritumoral infiltration = 0.019
	therapeutic pathomorphosis II	20 (45.5)	23 (35.9)	9 (28.1)	
	therapeutic pathomorphosis III	6 (13.6)	21 (32.8)	8 (25.0)	
	therapeutic pathomorphosis IV	4 (9.1)	13 (20.3)	9 (28.1)	
Radiation therapy response	Full effect	6 (15.8)	10 (18.9)	2 (11.1)	
	Partial effect	20 (52.6)	19 (35.8)	6 (33.3)	
	Stabilization	6 (15.8)	15 (28.3)	7 (38.9)	
	Progression	6 (15.8)	9 (17.0)	3 (16.7)	0.521

** – differences in indicators are statistically significant ($p < 0.05$)*

When comparing the response to chemotherapy and radiation therapy by localization types, no significant statistical differences were found ($p > 0.05$). This suggests that, despite the effect of CD4 lymphocyte localization on tumor morphological regression, they are less dependent on the short-term clinical effectiveness of therapy.

The localization of $CD4^+$ T-lymphocytes within the tumor tissue (intratumoral infiltration) may indicate an active immune response to tumor development, contributing to its regression, as these cells perform regulatory and auxiliary functions, activate cytotoxic T-lymphocytes, and contribute to the synthesis of antibodies, enhancing the anti-tumor immune response. In peritumor infiltrates (peritumoral infiltration), the role of these cells may be less stable or less active in the context of the morphological response, which is associated with less permeability or less intensive activation of immune mechanisms within the tumor.

It has been proven that the localization of CD4 lymphocytes plays a significant role in the morphological regression of the tumor and the degree of pathomorphism, which is important for prognostic assessment and the development of immunotherapeutic strategies. It should be noted that the activity of circulating or peritumor CD4-lymphocytes may have less value for predicting short-term clinical effects, while localization within the tumor is a critical factor for assessing the potential of the immune response.

The localization of CD4 lymphocytes within the tumor (intratumoral infiltration) is significantly related to the severity of mor-

phological regression and a higher level of therapeutic pathomorphosis. The activity of immune cells within the tumor stroma component contributes to a more effective morphological response to treatment and can serve as a prognostic marker for assessing the potential of immune-responsible regression in soft tissue sarcomas. At the same time, the effect of CD4 localization in the peri-tumor zones is less pronounced and does not significantly affect the response to reconstructive therapy.

Conclusion

As a result of the conducted research, it was established that the localization of CD4-lymphocytes within the tumor tissue – in particular, their infiltration into the tumor parenchyma (intratumoral infiltration) – is significantly related to the pronounced morphological regression of the tumor process and the high level of therapeutic pathomorphosis, which indicates the important role of these cells in the formation of an effective antitumor immune response. The activity of CD4+ T-lymphocytes within tumor structures contributes to the strengthening of the immune mechanism, stimulates cytotoxic T-lymphocytes and other components of the immune system, which conditionally leads to a decrease in tumor volume and more pronounced morphological tissue. These data confirm the theoretical concept that local immune activity within the tumor is the most important driver of therapy, capable of improving morphological indicators and, possibly, long-term clinical outcomes.

At the same time, the absence of statistically significant differences in clinical response, expressed in the form of complete, partial, stabilizing effects and progression, indicates the complexity of the relationship between immune activity and short-term therapeutic outcomes. This may be due to the fact that immune status, especially the localization and activity of CD4-lymphocytes, primarily affects morphological regression and long-term defense mechanisms rather than acute clinical indicators such as symptomatic dynamics or shortened response time.

These results emphasize the need to consider immune factors when planning complex therapy for soft tissue sarcomas. In particular, assessing the localization of CD4-lymphocytes in tumor tissue can serve as an additional predictor of the effectiveness of the morphological response and long-term prognosis. In the future, the use of this marker in clinical practice can contribute to individualizing treatment strategies, increasing the effectiveness of immunotherapy, and developing new methods for activating immune mechanisms within the tumor microenvironment. Overall, the obtained conclusions confirm the prospects for further research aimed at a deeper understanding of the role of the immune system in the regression of sarcomas and the optimization of immunotherapy.

References

Huang H., Fan Y., Zhang S., Bai X., Wang X., Shan F. (2025). Emerging immunotherapy and tumor microenvironment for advanced sarcoma: a comprehensive review. Front Immunol. May 21; – 16: 1507870. Doi: 10.3389/fimmu.2025.1507870. PMID: 40469285; PMCID: PMC12133756

Van der Graaf W. T. A., Orbach D., Judson I. R., Ferrari A. (2017). Soft tissue sarcomas in adolescents and young adults: A comparison with their paediatric and adult counterparts. Lancet Oncol. – 18: e166-e75. Doi: 10.1016/s1470-2045(17)30099-2

Lee A. Q., Hao C., Pan M., Ganjoo K. N., Bui N. (2024). Use of histologic and immunologic factors in sarcoma to predict response rates to immunotherapy. J Clin Oncol. – 42: 11569. Doi: 10.1200/JCO.2024.42.16_suppl.11569

Wood G. E., Meyer C., Petitprez F., D'Angelo S. P. (2024). Immunotherapy in sarcoma: current data and promising strategies. Am Soc Clin Oncol Educ Book. – 44: e432234. Doi: 10.1200/edbk_432234

Recine F., Vanni S., Bongiovanni A., Fausti V., Mercatali L., Miserocchi G., et al. (2024). Clinical and translational implications of immunotherapy in sarcomas. Front Immunol. – 15: 1378398. Doi: 10.3389/fimmu.2024.1378398

Sources of funding: *The work did not receive any specific funding.*

Conflict of interest: *The authors declare no explicit or potential conflicts of interest associated with the publication of this article.*

Contribution of the authors:

Polatova D.Sh. – ideological concept of the work, writing the text; editing the article;
Karimova N. M. – collection and analysis of literature sources, writing the text;
Kahharov A. J. – assistance in text correction

submitted 17.04.2025;
accepted for publication 01.05.2025;
published 29.05.2025

Contact: polatova.dj@gmail.com; karimovanargiza939@gmail.com;
djumaniyazova.gulnoza@bk.ru

The Austrian Journal of Technical and Natural Sciences, No 5–6
ISSN 2310-5607

PREMIER Publishing
ppublishing.org

DOI:10.29013/AJT-25-5.6-106-110

EFFECT OF ALCOHOL INTOXICATION ON TOXICOKINETIC INDICES IN ACUTE ACETIC ACID POISONING

Sultanova N. D. [1]***, Iskandarov A. I.*** [2]***, Yadgarova Sh. Sh*** [2]

[1] Tashkent city branch of the Republican scientific and practical center of forensic medical examination. Tashkent, Republic of Uzbekistan

[2] Department of Forensic medicine of the Tashkent Pediatric Medical Institute; Tashkent, Republic of Uzbekistan

Cite: *Sultanova N. D., Iskandarov A. I., Yadgarova Sh. Sh. (2025). Effect of Alcohol Intoxication on Toxicokinetic Indices in Acute Acetic Acid Poisoning. Austrian Journal of Technical and Natural Sciences 2024, No 5–6.* https://doi.org/10.29013/AJT-25-5.6-106-110

Abstract

The article presents data from a retrospective analysis of 40 victims and 30 corpses, persons who died from acute acetic acid poisoning against the background of alcohol intoxication. The toxicokinetics were assessed according to the WHO guidelines (1981). The nonlinear resistance analysis method was used to determine the main parameters of toxicokinetics: the elimination rate constant, the half-life of the poison in the blood, and the maximum duration of the toxicogenic phase in acetic acid poisoning against the background of alcohol intoxication.

Keywords: *toxicokinetics, elimination rate constant, half-life of poisons in the blood, maximum duration of the toxicogenic phase*

Relevance of the problem:

Forensic examination of acute poisoning is one of the important and complex sections of forensic toxicology. Statistics show that a significant number of the total number of acute poisonings are caused by cauterizing poisons, including acetic acid (Kazsuba A., Viter A. et all., 2000; Penner G. E. 2008; Zamir O., Hod G. et al., 1985). Acetic acid is widely used in everyday life. Among the causes of poisoning with this poison, suicidal tendencies (Akhmedov D. A., 2019; Akhunov A. A., 1989; Klimov I. A., Gorbakov V. V., 2009) and accidental poisoning prevail, although accidental poisonings are fatal.

Acute oral poisoning with acetic acid is characterized by a severe course and high mortality (WHO Guidelines, 1981; Mills S. W., Okoe M. I., 2007; Weintraub B. A., 2007).

The clinical and morphological picture of acute poisoning with acetic acid has been studied for a long time. However, the main studies concern the pathogenesis, clinical picture and treatment of these intoxications. Thus, Rusakov A. V. (1930) was the first to establish an expert opinion on hemoglobinuric nephrosis in cases of poisoning with acetic essence, as the most characteristic complication of intravascular hemolysis, and N. K. Permyakov in 1979 proposed an

original classification of the stages of developmenthemoglobinuric nephrosis and by the nature of the disorders in the kidneys, substantiating the possibility of determining the duration of hemolysis. However, these studies were purely empirical in nature, and the effects of free hemoglobin in acid poisoning on the entire area of morphological changes in the internal organs have never been systematically studied. It is known that in everyday life, acetic acid poisoning is accompanied by alcohol intoxication (10). How concomitant alcohol intoxication leads to the removal of poison from the body and in the available literature was not found.

Purpose of the study:

To study the toxicometry of acute poisoning with acetic acid for toxicokinetics of the poison and to develop exogenous criteria for quantitative assessment.

Materials and methods:

This study is based on 140 cases of acute non-ideal poisoning with acetic acid, of which 92 cases (65.7%) were poisoned against the background of alcohol intoxication. Of these, 75 cases (81.5%) were poisoned with suicidal intent and only 17 cases were due to accidental ingestion of poison. The victims were treated at the Republican Scientific Center for Emergency Medical Care in the toxicology department. Forensic medical examination of corpses was carried out according to the generally accepted method in the first 10–8 hours, but not later than 24 hours after death.

In all expert cases, poisoning with acetic acid against the background of alcohol intoxication was confirmed by the case materials, the clinical picture of the poisoning, the results of the forensic medical examination of the corpse and the data of the forensic chemical and toxicological examination.

The severity of acute acetic acid poisoning was assessed based on the extent of chemical burns of the gastrointestinal tract, the shift in capillary blood pH, and the level of intravascular hemolysis.

In the clinic, when assessing the severity of the pathological process, they mainly focused on the level of hemoglobinemia, i.e. the concentration of free hemoglobin in the blood.

Ethyl alcohol was determined in a forensic chemical laboratory using liquid chromatography methods.

We assessed the toxicokinetics of the poison according to the WHO guidelines (1981). The kinetics of diffusion processes is described by exponential laws and is called first-order kinetics. In this case, the rate of change in the concentration of the poison in the blood plasma can be expressed as a linear differential equation:

$$\frac{d}{c} = Ke \times C(t)dt$$

Where: $C(t)$ is the concentration of poison in the blood plasma at time t; Ke is the elimination rate constant.

Solutions of this differential equation with initial conditions $C(t) = C(o)$ at the time of admission of the victim to the hospital (zero time) gives:

$$C(t) = C(0)^{-Kext}$$

Based on this model, the following main parameters of acetic acid toxicokinetics were determined using the nonlinear resistance analysis method: the rate constant of elimination of the poison, the half-life of the poison in the blood, and the maximum duration of the toxicogenic phase of poisoning.

The elimination rate constant (Ke) shows what proportion of the total amount of toxic substance present in the circulatory system is removed during each time interval; it is measured in units of inverse time (l/t).

The half-life of a poison in the blood is the time required for its concentration to decrease by half. This indicator, widely used in theoretical toxicology, is designated as T ½ and can be determined from the equation:

$$T_{1/2} = \frac{\ln 2}{Ke} = \frac{0.693}{Ke}$$

The maximum duration of the toxicogenic phase is determined by the time the poison is present in the blood.

Results and discussions

Based on the kinetic model presented in the “Materials and Methods”, using a computer and the method of nonlinear repressive analysis, the above parameters of the toxicokinetics of acetic acid (Table No. 1) and

their changes against the background of alcohol intoxication of varying degrees were quantitatively determined.

Table 1. *Toxicokinetics of acetic acid against the background of alcohol intoxication*

Acetic acid and concomitant alcohol intake of varying degrees	Initial blood poison level (free hemoglobin mg/ml)	Ke	T ½ (hour)	Maximum duration of the toxicogenic phase (hours)
Acetic acid (free hemoglobin)	12.3±4.73	0.043	16.5	56
Free hemoglobin in combined moderate alcohol poisoning	11.8±5.12	0.039	17.8	59
Free hemoglobin in combined severe alcohol poisoning	10.40±3.72	0.027	23.6	64

Figure 1. *Toxicokinetics of free hemoglobin in acetic acid poisoning against the background of alcohol intoxication: a) typical; b) moderate alcohol intoxication; c) severe alcohol intoxication*

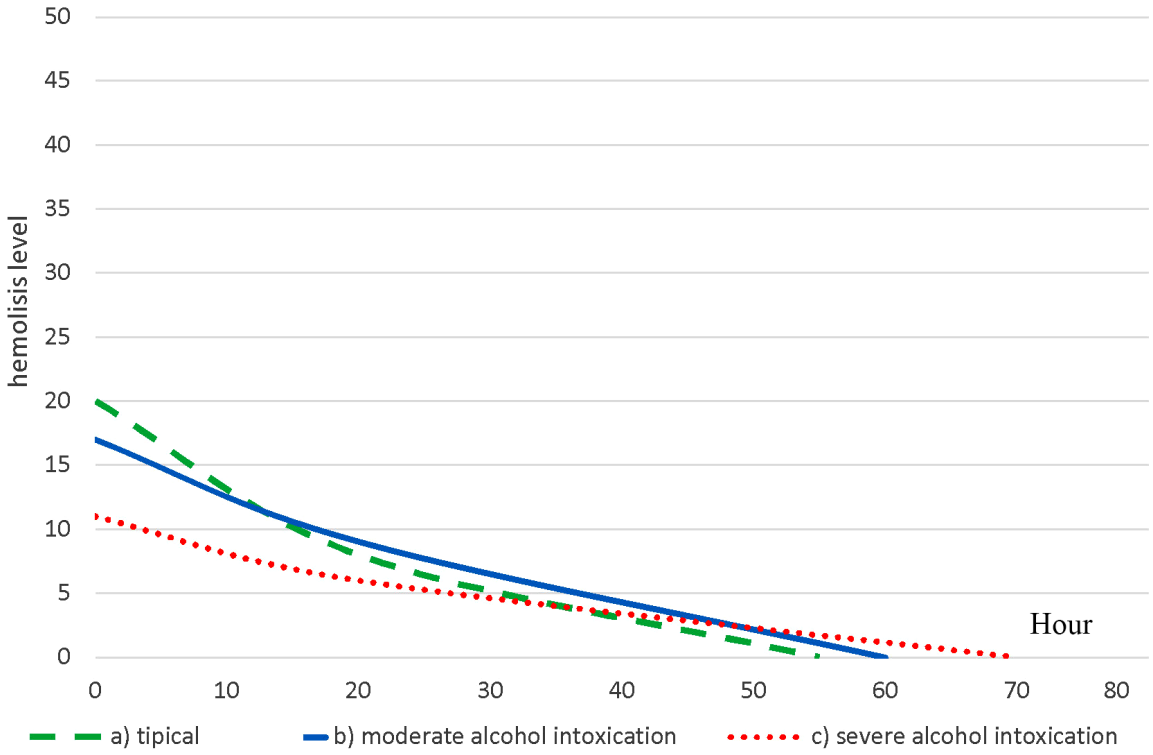

As follows from the table, if the rate of elimination of acetic acid from the blood can be estimated as comparatively high in acute poisoning with acetic acid alone (0.043), and in combined poisoning with this poison against the background of moderate alcohol intoxication (1.5–2.5‰), as moderate with Ke-0.039, T ½ –17.8 hours with the duration of the toxicogenic phase – 59 hours, then in combined poisoning with acetic acid and severe alcohol intoxication (2.5–3.5‰ and more). Ke was equal to 0.027, i.e. the rate of elimination of the poison from the body was much lower than in isolated poisoning with acetic acid alone. Moreover, even with an initial value of the free hemoglobin level equal to 10.40±3.72 mg/ml, much lower than in isolated poisonings (12.3±4.78), the half-life of the poison (free

hemoglobin) was 23.6 hours (versus 16.5 hours in isolated poisoning), and the maximum duration of the toxicogenic phase increased from 56 hours to 64 hours (P<0.01).

Thus, it can be stated that in acute poisoning with acetic acid against the background of alcohol intoxication, the main indicators of the toxicokinetics of acetic acid change significantly and depend on the degree of intoxication of the victims, which must be taken into account in the expert assessment of the severity of chemical injury. Figure 1 shows the standard kinetic curve (graph) based on the toxicokinetics of free hemoglobin against the background of alcohol intoxication of varying degrees.

According to modern views, the pathogenesis of acute poisoning should be studied in two aspects: what the poison does to the body and what the body does to the poison. To solve this problem, the method of covariance analysis was used. As part of our studies, we determined the effect of exotoxic shock on the kinetics of free hemoglobin, since exotoxic shock is one of the main causes of death in acid poisoning (Table 2).

Table 2. *The effect of decompensated exotoxic shock on the kinetics of free hemoglobin in acetic acid poisoning against the background of alcohol intoxication*

Types of acetic acid poisoning	Baseline free hemoglobin level (mg/ml)	Ke	T ½	Maximum duration of the toxicogenic phase
Acetic acid:				
1) hemodynamics are stable	11.62±8.76	0.036	22.6	58
2) Decompensated shock	22.34±9.36	0.028	28.2	64
Acetic acid against the background of alcohol intoxication:				
1) hemodynamics are stable	16.50±48.28	0.026	29.6	68
2) Decompensated shock	24.18±9.36	0.034	24.6	60

Changes in the main parameters of toxicokinetics of free hemoglobin against the background of exotoxic shock are primarily associated with the disruption of the pathways for removing the poison from the body. According to our observations, exotoxic shock is naturally accompanied by oliguria and a significant delay in the fluids removed from the body. Since the removal of free hemoglobin from the body is carried out mainly through the urinary system, it is natural that under these conditions the toxicokinetics of the poison is also disrupted.

As follows from the data of Table 2, acetic acid poisoning against the background of alcohol intoxication proceeds in exotoxic shock in a completely ambiguous manner. Here, alcohol in small concentrations (from 1.5 to 2.5‰) has a favorable effect on the course of poisoning. Thus, with an initial hemolysis level of 24.18 ± 9.36 mg / ml, the elimination rate constant has a value of 0.034, i.e., an acceleration of the rate of elimination of free hemoglobin from the bloodstream is observed, and the half-life of the poison in the blood is equal to 24.6 hours, the maximum duration of the toxicogenic phase is shortened to 60 hours. This effect of alcohol in small concentrations is apparently due to the fact that alcohol activates metabolic processes in the liver, which ultimately leads to the rapid elimination of the poison from the bloodstream, which leads to a more accelerated exit of the body from the state of decompensated shock. However, it should be noted that such a beneficial effect of alcohol on the course of decompensated shock is observed only with moderate alcohol intake. With ethyl alcohol concentrations in the blood of more than 2.5–3.0‰, we noted a sharp deterioration in the condition of the victims and often exotoxic shock led to a fatal outcome.

Thus, the results of these studies showed the forensic significance of the degree of hemolysis and the main patterns of its tox-

icokinetics and their changes against the background of alcohol intoxication.

Conclusions:

1. The outcome of chemical trauma largely depends on how quickly and effectively the absorbed dose of poison can be eliminated.

2. The use of graphs for assessing the main parameters of free hemoglobin kinetics in cases of acetic acid poisoning allows for a quantitative assessment of the risk of death and the effectiveness of detoxification measures.

3. The effect of concomitant alcohol intoxication in acetic acid poisoning on toxicokinetic indices is not clear and depends on the initial concentration of ethyl alcohol in the blood.

References

Akhmedov D.A. (2019). Intensive care and resuscitation of patients in a state of hemolytic shock // Current issues of anesthesiology and resuscitation. Dushanbe, – No. 7. – P. 163–165.

Akhunov A.A. (1989). Forensic medical examination of acute poisoning with acetic acid // Author. diss. candidate of medical sciences, – Moscow Medicine, 18th article.

Berezhnoy R.V. et al., (1989). Guide to forensic medical examination of poisonings. – M. Meditsin, – P. 55–79.

Gorin E.E. (1980). Critical condition in acetic acid poisoning (diagnostics, prognosis, resuscitation) // Author. diss. candidate of medical sciences, 19th article.

Klimov I.A., Gorbakov V.V. (2009). Acute oral poisoning with acetic acid // military medical journal, – No. 3. – P. 38–41.

WHO Guidelines (1981). (Determination of toxicokinetics of poisons).

Kazsuba A., Viter A. et all. (2000). Gastric hualinization as a possible conseguence os corrosive injury. Endoscopy-Jasbereny, Hungary, Apri – 32 (4). – P. 356–358.

Mills S.W., Okoe M.I. (2007). Sulfuric acid poisoning. Am J. Forensic Med. Pathol., Flint, Michigan, Sept. – 8 (3). – P. 252–255.

Penner G.E. (2008). Acid ingestion: toxicology and treatment, jul: – 9(7). – P. 374–379.

Ross D. (1985). Case history: an acid fumes hazard. Occup Health (London), Apr. – 37(4). – P. 187–188.

Weintraub B.A. (2007). A fatal case of acid ingestion. Chicago, Illinois, USA, oct. – 23(5). – 413 p.

Zamir O., Hod G. et al. (1985). Corrosive injury to the stomaclidue to acid ingestion. Am Z. Surg., Mar. – 51 (3). – P. 170–172.

submitted 17.04.2025;
accepted for publication 01.05.2025;
published 29.05.2025

Contact: sudmeduztash@gmail.com; iskandarov50@mail.ru; shabnamibragim@gmail.com

The Austrian Journal of Technical and Natural Sciences, No 5–6
ISSN 2310-5607

PREMIER Publishing
ppublishing.org

Section 6. Technical science in general

DOI:10.29013/AJT-25-5.6-111-115

PROSPECTS FOR USING ROBOTIC COMPLEX IN THE MINING INDUSTRY (using basalt mining as an example)

Alimova Nodira Batirdjanovna [1], ***Yusupov Bekmurod Bayotovich*** [1], ***Ozodova Dilrabo Oltinbek qizi*** [1]

[1] Department of Mechatronics and robotics,
Tashkent State Technical University, Uzbekistan

Cite: *Alimova N.B., Yusupov B.B., Ozodova D.O. (2025). Prospects for Using Robotic Complex in the Mining Industry (using basalt mining as an example). Austrian Journal of Technical and Natural Sciences 2024, No 5–6.* https://doi.org/10.29013/AJT-25-5.6-111-115

Abstract

The main technological stage in the extraction of minerals is the mining and processing complexes. The article analyzes the current state, prospects and general directions of development of robotic mining equipment. Robots are key tools for increasing productivity because they perform a wide range of manual tasks more efficiently and consistently than humans. Therefore, the development of robotic systems is an important development task for the mining industry.

Keywords: *minerals, basalt, robotic complex, safety, efficiency*

Introduction

Currently, the mining industry is in constant development, which determines the use of innovative technologies and modern equipment. Increased efficiency of a mining enterprise can be achieved by increasing the productivity of the process of transporting rock mass, saving fuel, reducing the vehicle fleet, reducing operating and maintenance costs. In addition, the mining industry has to work in all climate zones in more dangerous and complex mining, geological and natural conditions, in hard-to-reach regions, complicated by the deepening of quarries, dust, gas pollution and difficulty of ventilation. These and other factors have a negative impact on the health of personnel.

Robotization of production is an integral part of complex automation and is the process of implementing a robotic complex, which includes isolated or combined robotic sections and lines.

Robotization of production provides an undeniable advantage in increasing production productivity, increasing the number of manufactured products per unit of time, improving their quality and reducing production costs. Modern industrial robots can

flexibly and quickly switch from one technological operation to another by replacing the control program. Robotic complexes (RC), like robots, are widely used in various industries, from industry to medicine and military affairs. In industry, RTCs are used to automate production, improve quality and reduce production cycles. In other areas, they are used for reconnaissance, monitoring, search and disposal of explosive objects (Dzhigaris, D. D., Makhova, M. F., 2002).

Formulation of the problem

The introduction of robots in the mining industry has revolutionized the sector. Mining companies now use robotics in a variety of operations, from open-pit mining to underground mining and mineral processing. The main benefits of robots in the mining industry include increased safety and efficiency.

In the mining industry, robots are used in a variety of operations, such as transportation, drilling, blasting, and mineral exploration. Some of the most commonly used robots include autonomous trucks, drilling robots, and robotic conveyor systems (Kamolov, B. S., 2023).

In recent decades, comprehensive scientific research work aimed at saving metals has been conducted in the Republic of Uzbekistan. Since not only in our country, but also throughout the world, there is an acute shortage of metals. This is evidenced by information available in technical sources of the press (Kurbanov, A. A., 2009). Scientists argue that there is a need to expand research into unexplored areas of nature and increase the volume of processed natural resources, especially those that are little studied, which can create import-substituting types of products (Kurbanov, A. A., 2018).

The study showed that there are little-studied minerals in nature that consist of metal-containing oxides. Basalt rocks can be classified as such minerals. According to the Ministry of Geology, the raw material reserves of basalt rock today amount to more than million tons with an iron content of, for example, 15÷20% (Shevchenko, V. P., Gulamova, D. D., 2011, Kurbonov, A., Sattorov, L., Kamolov, B., Rakhimov, O., 2023, Kamolov, B. S., Kurbanov, A. A., Sattorov, L. K., 2023).

Basalt is a natural igneous rock formed by the cooling of lava. It is widespread on Earth, making up a significant portion of oceanic crust and volcanic rocks. Due to its properties, basalt has found application in many industries, including construction, industry, and even space technology.

Basalt is distinguished by its color variety: from black to gray and greenish shades. The structure of basalt depends on the composition. So, if it includes minerals, then when cut, inclusions of green, white or gray color are noticeable. Glass wool is also characterized by small impurities, but there are very few of them.

Basalt is characterized by columnar jointing. This means that high columns are visible in the structure. They are formed due to uneven cooling of lava. Moreover, their height fluctuates from several centimeters to meters. Therefore, the rock pattern looks original. If the basalt is marine, then instead of columns, separate pillows are formed.

The rock texture should be massive, porous, with almond-shaped formations – oval areas that are filled with other minerals such as calcite or feldspar.

The main advantage of basalt is its strength and resistance to environmental influences. The material is practically not subject to corrosion, does not lose its properties under the influence of moisture, temperature changes or chemical reagents.

Basalt processing involves various types of processing of this igneous rock, from crushing to the production of various materials and products. Basalt is used as a raw material for crushed stone, basalt fiber, as well as for the production of building blocks, tiles, statues and other products. Innovative technologies have expanded the range of applications of basalt (Drobot, N.F., Noskova, O.A., Steblevskii A. V., 2013).

Solution to the problem:

Basalt can be processed in a variety of ways, depending on the desired end product. The main processing methods include:

– **Mechanical processing:**

Basalt can be processed manually to create small parts, while large slabs are produced using conveyor production.

– **Heat treatment:**

Basalt is heat treated to produce basalt fibers, which can then be used in a variety

of applications, such as insulation, building materials, and other products.

– **Melting:**

To produce basalt fiber, basalt is crushed, washed and melted at high temperature, then extruded through nozzles to produce continuous strands.

– **Flake processing:**

Basalt rock is loaded into a furnace, melted, and then the melt is discharged through a feeder to produce basalt flakes, which are used in various fields.

Figura 1. *Basalt and its crushing*

The use of robots in basalt mining is possible and promising in various operations, including transportation, drilling, blasting and exploration. Robots can be used to improve productivity, safety and reduce costs in mining operations. In particular, autonomous trucks and drilling robots, as well as robotic conveyor systems, can significantly simplify and optimize the basalt mining process.

Advantages of using robots in basalt mining:

– **Increased productivity:** robots can work around the clock and without breaks, which allows for an increase in the volume of basalt mined.

– **Increased safety:** work in hazardous conditions (for example, in tunnels or during blasting operations) can be performed by robots, minimizing the risk to personnel.

– **Reduced Costs:** Robots can reduce labor requirements and lower equipment maintenance costs.

– **Improved Product Quality:** Robots can provide more precise and controlled extraction, which can improve the quality of the final product.

Types of robots used in basalt mining:

– **Autonomous trucks:** These are used to transport basalt from the mine.

– **Drilling robots:** These are used to drill into rocks.

Figura 2. *Basalt crushing scrreningplant*

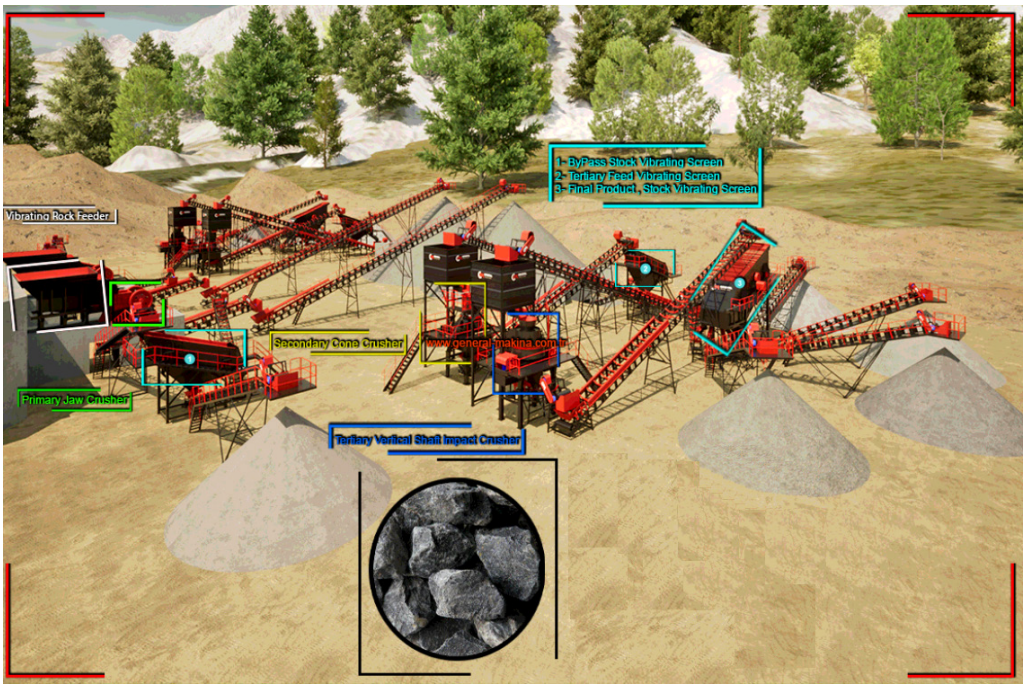

– **Robotic conveyor systems:** These are used to transport basalt around mines and quarries.

– **Mobile mapping robots:** These are used to create accurate maps of the mines.

Applications of robots in basalt mining:

– **Open-pit mining:** Autonomous trucks and drilling robots are widely used in open-pit mines.

– **Underground mining:** Robots can be used for drilling, transporting and blasting in mines.

– **Exploration and geological survey:** Mobile robots can be used to collect information about deposits.

Examples of robots being used in basalt mining:

– Some companies use autonomous trucks to transport basalt from mines, allowing them to reduce transportation costs and improve safety.

– Other companies are using robots for drilling and blasting operations in mines, helping them increase productivity and reduce risks to personnel.

– In some cases, robotic conveyor systems are used to transport basalt, making the mining process easier and faster (Alimova, N. B., Ozodova, D. O., 2025).

Conclusion

Basalt is thus a versatile and environmentally friendly material that continues to find new applications. Its unique properties make it indispensable in both traditional and high-tech applications.

As the industry is under pressure to reduce costs and improve efficiency and safety, automation is becoming the solution.

Based on the above studies, the need to develop a concept for processing different types of basalt raw materials for maximum satisfaction of the growing demand of the national economy for new, cheap, competitive and currency-saving basalt products, and thus rational and comprehensive use of natural raw materials, has been proven.

In this regard, robotics surpasses human capabilities in performing tasks with precision, resulting in increased efficiency, reduced waste in mining operations, reduced machine damage, increased equipment life, and reduced manual labor. Therefore, the topic of robotics is prominent in the sector, highlighting it as one of the key investment areas that the industry prioritizes.

In addition, safety is increased by performing dangerous tasks without the need for humans.

References

Dzhigaris D. D., Makhova M. F. Basics of production of basalt fibers and products: monograph. – M.: Teploenergetik, 2002. – 411 p.

Kamolov B. S. O rasprostranenii syr'yevykh zapasov bazal'tov po Uzbekistanu // Journal of Innovations in Scientific and Educational Research. 2023. – № 6(10). – P. 126–132.

Kurbanov A. A. Spetsificheskiye osobennosti bazal'tov Kyzylkuma. Monografiya. – Tashkent: Fan. 2009. – 160 p.

Kurbanov A. A. Razrabotka ratsional'noy tekhnologii pererabotki raznotipnykh bazal'tov Uzbekistana. – Navoi, 2018. – 257 p.

Kurbanov A. A., Rakhmatov B. U., Kamolov B. S., Rakhmatov KH. B. Sravnitel'nyy analiz fiziko-khimicheskikh svoystv bazal'tovykh porod dlya vybora kriteriy pri vypuske raznoobraznoy produktsii // KarDU KHAB. 2019. – 78 p.

Shevchenko V. P., Gulamova D. D. Polucheniye i issledovaniye svoystv bazal'tovogo volokna na osnove prirodnogo syr'ya Uzbekistana // Khimiya i khimicheskaya tekhnologiya. – Tashkent, 2011. – № 2. – P. 10–12.

Kurbonov A., Sattorov L., Kamolov B., Rakhimov O. Chemical and mineralogical studies of basalt "Aydarkul" BIO // Web of Conferences. 2023. – № 71. – P. 02040.

Kamolov B. S., Kurbanov A. A., Sattorov L. K. (2023). Features of filtration of industrial gases from dust with a basalt filter // E3S Web of Conferences. – Vol. 411. – P. 01036.

Drobot N. F., Noskova O. A., Steblevskii A. V. et al. // Use of Chemical and Metallurgical Methods for Processing of Gabbro – Basalt Raw Material // Theoretical Foundations of Chemical Engineering. 2013. – V. 47. – No. 4. – P. 484–488.

Alimova N. B., Ozodova D. O. Analysis of existing methods of basalt ore processing in Uzbekistan. Internauka. 2025. – No. 20 (384). Part 5. – P. 10–13.

submitted 17.04.2025;
accepted for publication 01.05.2025;
published 29.05.2025

Contact: nodira.alimova.71@gmail.com

The Austrian Journal of Technical and Natural Sciences, No 5–6
ISSN 2310-5607

PREMIER Publishing
ppublishing.org

DOI:10.29013/AJT-25-5.6-116-119

PRODUCTION OF HIGH-ACTIVITY CATALYSTS FOR OBTAINING LIQUID HYDROCARBONS FROM NATURAL GAS

Togayev Abror [1]

[1] Karshi State Technical University, Karshi, Uzbekistan

Cite: *Togayev A. (2025). Production of High-Activity Catalysts for Obtaining Liquid Hydrocarbons From Natural Gas. Austrian Journal of Technical and Natural Sciences 2024, No 5–6.* https://doi.org/10.29013/AJT-25-5.6-116-119

Abstract

The article presents the use of highly catalytically active catalysts in industrial processes of petrochemistry and oil refining, mainly for converting low-molecular hydrocarbons to obtain liquid hydrocarbons from natural gas. It also describes the stages of developing modern processes for obtaining environmentally friendly liquid fuels, with a minimum amount of harmful impurities, and a group composition that meets the requirements for motor fuels.

Keywords: *Catalyst, methods, hydrocarbon, zeolite, Fisher-Tropsch-Synthesis, gas, stage*

Introduction

Catalytic reforming is one of the main technological processes in petrochemical synthesis, which serves to obtain high-octane gasolines, which are important for internal combustion engine fuels. Fischer-Tropsch synthesis (FTS) is the main stage of the technology for producing high-quality liquid fuels from low-molecular hydrocarbon feedstocks. This is a heterogeneous catalytic process for converting a mixture of CO and H_2 (synthesis gas) into organic substances, which can be widely used as fuel and raw material for organic synthesis. The relevance of developing technologies based on FISHER-TROPCH SYNTHESIS is currently determined by a number of factors, primarily the need to use natural resources with unconventional hydrocarbon content and increasing requirements for the properties of motor fuels. The most acute problem is the utilization of tail gas (TSG). (Kuybokarov O. et al., 2024).

Catalysts considered for Fischer-Tropsch synthesis are based on transition metals of iron, cobalt, nickel and ruthenium. FT catalyst development has largely been focused on the preference for high molecular weight linear alkanes and diesel fuels production. Among these catalysts, it is generally known that:

- Nickel (Ni) tends to promote methane formation, as in a **methanation process;** thus generally it is not desirableIron (Fe) is relatively low cost and has a higher water-gas-shift activity, and is therefore more suitable for a lower hydrogen/carbon monoxide ratio (H_2/CO) syngas such as those derived from coal gasification;
- Cobalt (Co) is more active, and generally preferred over ruthenium (Ru)

because of the prohibitively high cost of Ru;
- In comparison to iron, Co has much less water-gas-shift activity, and is much more costly. (Mark Crocker, 2010).

Catalysts with high catalytic activity for the production of liquid hydrocarbons from natural gas were prepared by two-stage impregnation of composite supports with a 75% aqueous solution of cobalt nitrate (Rahimov G. et al., 2024).

Materials and methods

Catalysts with high catalytic activity for the production of liquid hydrocarbons from natural gas were prepared by two-stage impregnation of composite supports with a 75% aqueous solution of cobalt nitrate.

The mechanical strength of the granules was determined by the impact force required to break and crush the granules under compression between two parallel planes. The strength of a catalyst with high catalytic activity intended for the production of liquid hydrocarbons from natural gas was calculated as the average value of the breaking force based on a sufficient number of tests.

The crushing (crushing) force of the granules was measured using the Vollstadt Diamant Diatest-S device. The force required for radial crushing (kilogram-force expended per granule) was determined. The result was obtained as an average value for 20 granules.

The device was equipped with a special pneumatic and hydraulic system, which allowed the possibility of adjusting the rate of load generation on the granules, which did not require the participation of the experimental scientist in the process (Murtazayev F. et al., 2024).

Composite supports are prepared in stages:

Stage 1 – preparation of the binder.

In a glass container, a solution of nitric acid, 0.45 ml of HNO_3 (64%) and 7 ml of distilled water were prepared. In a porcelain container, 2 g of beechmite and 1 g of zeolite with high sorption and catalytic properties were thoroughly mixed and the resulting acid solution was added. The resulting mixture was mixed until a homogeneous gel-like mass was formed.

Stage 2 – preparation of aluminum metal powders. Simultaneously with stage 2, 4 g of aluminum metal powder with an average particle size of 20 μm was weighed in a separate container. 1.13 g of TEG and 2.25 g of ethyl alcohol were added to the resulting mixture (strictly in this order). The aluminum was mixed gently, without force, so that it was evenly moistened with a mixture of alcohol and TEG.

Stage 3 – preparation of the carrier composition (paste). The mixture prepared in step 3 was added to the mixture obtained in step 2 and mixed thoroughly until a uniform consistency of soft and plastic dough was obtained.

Stage 4 – molding. The dough was transferred to an extruder and pressed onto trays through a die with a diameter of 2.5 mm. The extrudates were placed on trays so that they did not obstruct the air flow and were kept in the air for at least 15 hours.

Step 5 – drying and polishing the carrier. The extrudates stored in air were annealed in a muffle furnace at temperatures from 60 to 450 degrees Celsius for 20 to 480 minutes as follows:

The extrudates were cooled to room temperature, removed from the muffle furnace, and ground to 2.5 × 2.0 mm.

The amount of components for the preparation of cobalt nitrate solution was calculated as follows:

The amount of cobalt required to obtain 10 g of a highly catalytically active catalyst for the production of liquid hydrocarbons from natural gas containing 20 wt. % cobalt.

The second impregnation and final annealing were carried out in a manner similar to the first impregnation and intermediate annealing.

To study the effect of the degree of cationization, zeolites with different K cations content and high sorption and catalytic properties were prepared. KHB and HKA zeolites with high sorption and catalytic properties were prepared by the following methods for cationization and decationization of HB and KA zeolites with high sorption and catalytic properties, respectively. (Togayev A, 2023).

Method for cationization of HB zeolite with high sorption and catalytic properties:

Initial components:

15 gr of HB zeolite with high sorption and catalytic properties

150 ml of 0.1 N KNO_3

15 gr of HB zeolite with high sorption and catalytic properties were added to 150 ml of 0.1 N KNO_3 solution and stirred with a magnetic stirrer without heating for 2 hours, after which it was kept at room temperature for at least 12 hours. Then the resulting solution was washed to a neutral pH in a Buchner funnel and dried at

120 °C for two hours. Decatation procedure of zeolite KA with high sorption and catalytic properties

Initial components:

15 gr of highly sorption and catalytic zeolite KA

300 ml of 0.5 n NH_4NO_3

The highly sorption and catalytic zeolite KA was kept in a drying oven at 120 °C for 2 hours. Then, the highly sorption and catalytic zeolite KA was added to the 0.5 n NH_4NO_3 solution and stirred with a magnetic stirrer for 5 hours at 60–70 °C. Then, it was kept overnight and then washed with hot distilled water in a Buchner funnel to a neutral pH value. Subsequently, the resulting zeolite, which has high sorption and catalytic properties, is annealed in the following mode:

Heating to –120 °C
– 2 hours isotherm 120 °C
– 1 hour heating to 220 °C
– 2 hours isotherm 220 °C
– 1 hour heating to 550 °C
– 4 hours isotherm 550 °C

The whole process was repeated 3 times.

Results and discussion

Sorption volume analyzers are usually used to analyze the specific surface area of nanoporous materials (pore sizes from 0.4 to 500 nm). The method consists in saturating the pre-cleaned surface of the tested substance with adsorbate gas at a constant negative temperature with a gradual increase in pressure. The specific surface area of the catalytic system can be calculated based on the amount of adsorbate gas used to form a single layer. With further increase in pressure, the specific surface of the catalyst with high catalytic activity for the recovery of liquid hydrocarbons from natural gas continues to be filled with adsorbate molecules until all the pores of the solid are completely filled. In this way, the pore volume and pore volume distribution on the surface of the catalyst with high catalytic activity for the recovery of liquid hydrocarbons from natural gas are calculated.

The BET method can be used to determine the specific surface area with an accuracy of 5–10% in the range of p/p_0 = 0.05––0.35. Additional computational models are required to determine the volume of pores of different diameters in the total pore volume for determining the fraction from adsorption isotherms.

The process of catalytic synthesis of high molecular weight synthetic hydrocarbons from natural gas, from pentane to pentadecane, was carried out in a flow reactor operating in differential mode.

The reactor for obtaining high molecular weight synthetic hydrocarbons from natural gas, from pentane to pentadecane, in the form of a steel tube with an internal diameter of 20 mm, contains an immobile bed of a catalyst selected for obtaining high molecular weight synthetic hydrocarbons from pentane to pentadecane from 5 synthesis gases, i.e., a mixture consisting of carbon monoxide and hydrogen.

The catalytic activity per unit volume of the catalyst selected for obtaining high molecular weight synthetic hydrocarbons from pentane to pentadecane from synthesis gases, i.e., a mixture consisting of carbon monoxide and hydrogen, was determined by the following formula:

$$\mathbf{W=A\times S\times \eta.}$$

Here, W – is the catalytic activity per unit volume of the catalyst;

A – is the relative activity of the catalyst,

S – is the surface area of the catalyst;

η – is the utilization rate of the selected catalyst.

The reactor for the production of high molecular weight synthetic hydrocarbons from natural gas, from pentane to pentadecane, is placed in a cylindrical electric furnace. The temperature in the furnace is controlled. The temperature in the furnace is measured thermocouple, and in the reactor for the production of high molecular weight synthetic hydrocarbons from natural gas, from pentane to pentadecane. Both thermocouples are made of chromel wires. The temperature in the reactor for the production of high molecular weight synthetic hydrocarbons from

natural gas, from pentane to pentadecane, is maintained with an accuracy of +10 °C.

Conclusion

1. It was found that granular cobalt catalysts containing cationic zeolites allow the production of synthetic oil with a final boiling point of up to 360 °C from CO and H_2 in one step.

2. In this work, it was shown that the use of zeolites cationized with alkali and alkaline earth metals allows the production of liquid hydrocarbons containing more than 40% of the C_{11}–C_{15} fraction, suitable for the production of high-quality diesel fuel.

3. It is shown that the degree of cationization of the zeolite affects the main characteristics of the process and the composition of synthetic oil.

4. It was confirmed that secondary transformations of hydrocarbons with the participation of composite cobalt catalysts based on zeolites cationized with alkali and alkaline earth metals proceed mainly by a monomolecular mechanism.

References

Kuybokarov, O., & Karshiyev, M., Rakhimov, G. (2024). Research of the catalytic properties of a catalyst selected for the production of high-molecular weight liquid synthetic hydrocarbons from synthesis gas. In *E3S Web of Conferences* (Vol. 498, p. 01008). EDP Sciences.

Mark Crocker, ed. *Thermochemical Conversion of Biomass to Fuels and Chemicals*, (2010). Royal Society of Chemistry.

Murtazayev, F. & Rakhimov, G. (2024, November). Study of physico-chemical properties of domestic AI-80 automobile gasoline and reduction of benzene content in gasoline. In *American Institute of Physics Conference Series* (Vol. 3244, No. 1, p. 050019).

Rakhimov, G., & Yuldashev, T. (2024, November). Study of the degree of foaming of absorbent compositions used when purifying gases from acidic components. In *AIP Conference Proceedings* (Vol. 3244, No. 1). AIP Publishing.

Togayev A., Rahmatov B. Study of the kinetics of the reaction of high molecular hydrocarbons with synthesis gas. European Chemical Bulletin Eur. Chem. Bull. 2023, 12(Special Issue 4), – P. 14456–14462.

submitted 17.04.2025;
accepted for publication 01.05.2025;
published 29.05.2025

Contact: king08@mail.ru

The Austrian Journal of Technical and Natural Sciences, No 5–6
ISSN 2310-5607

PREMIER Publishing
ppublishing.org

DOI:10.29013/AJT-25-5.6-120-126

STUDY OF THE REMOVAL OF SODIUM AND CALCIUM IONS FROM SATURATED DIETHYLENE GLYCOL (SDEG) USING SODA ASH SOLUTIONS

***Mamarasulov B. S.*[1], *Koshanova B. T.* [1], *Erkaev A. U.*[1], *Reymov A. M.* [2], *Reymov K. D.* [2]**

[1] Tashkent Institute of Chemical Technologyт

[2] Karakalpak State University named after Berdakh

Cite: *Mamarasulov B. S., Koshanova B. T., Erkaev A. U., Reymov A. M., Reymov K. D. (2025). Study of the Removal of Sodium and Calcium Ions from Saturated Diethylene Glycol (SDEG) Using Soda Ash Solutions. Austrian Journal of Technical and Natural Sciences 2024, No 5–6.* https://doi.org/10.29013/AJT-25-5.6-120-126

Abstract

This paper explores the process of removing sodium and calcium ions from saturated diethylene glycol (SDEG), used in natural gas dehydration. It was established that during operation, SDEG accumulates impurities, including sodium and calcium chlorides, which affect its efficiency. Studies were conducted on the solubility of these salts in DEG solutions at varying temperatures and concentrations. It was shown that calcium mainly remains in solution during evaporation, complicating regeneration. A two-stage purification process is proposed: preliminary precipitation of calcium as carbonate using a 30% soda ash solution, followed by evaporation and removal of sodium chloride. X-ray diffraction analysis and chemical composition of the precipitates confirm the effectiveness of the proposed method. The developed approach enhances DEG regeneration quality and prevents impurity buildup in the system.

Keywords: *diethylene glycol, saturated diethylene glycol (SDEG), regeneration, soda ash, sodium chloride, calcium chloride, solubility, precipitation, natural gas purification, calcium carbonate*

Introduction

The purification and dehydration of natural gas are crucial stages in the preparation of raw materials for transportation and processing. One of the most effective absorbents used for moisture removal is diethylene glycol (DEG), which possesses high hygroscopicity as well as thermal and chemical stability (Korneev A. A., Yakovlev I. M., 2004; Grishin A. M., 2011). However, during operation, DEG becomes saturated with moisture and contaminated with inorganic salts, primarily sodium and calcium chlorides originating from formation water (Reznikov A. A., Pleshkov Yu. P., 1987). This leads to a decline in its absorption properties and necessitates regeneration (Perry R. H., Green D., 2007).

DEG regeneration processes involve the removal of moisture, volatile organic compounds, and mineral impurities. In recent years, particular attention has been paid to the removal of calcium and sodium ions, as their presence promotes salt deposition on equipment surfaces, reduces heat transfer efficiency, and increases the risk of corrosion (Akhmetov G. Kh., 2009; Marchenko A. V., 2017).

The literature describes various approaches to reducing salt concentrations in saturated DEG (SDEG), including evaporation, extraction, and chemical precipitation techniques (Chernyshev I. G., Titov V. P., 2006). It is known that calcium can be effectively removed from solution in the form of sparingly soluble calcium carbonate through interaction with carbonate-containing solutions such as soda ash (Na_2CO_3) (Chandrasekaran V., 2019). This method is widely used in water treatment and in the purification of industrial process solutions (Chandrasekaran V., 2019).

The solubility of sodium and calcium chlorides in water-glycol systems has been thoroughly studied in several works (Knaebel K. S., 2006; Kovács G., Vatai G., 2010; Aliev I. A., Mukhamedov Sh. D., 2005). It has been established that $CaCl_2$ exhibits significantly higher solubility in DEG compared to NaCl, thereby necessitating a staged approach to their removal. The use of refractometric methods to monitor DEG concentration and salt content is also described in the literature as an effective analytical tool (Aliev I. A., Mukhamedov Sh. D., 2005; Mamarasulov B. S., Yuldashev N. Kh., Begdullaev A. K., Reymov K. D., Toirov Z. K., Erkaev A. U., 2022).

Thus, modern research confirms the relevance of an integrated approach to DEG regeneration, with a focus on preliminary precipitation of calcium ions followed by the removal of sodium chloride. This enables a significant improvement in absorbent efficiency and extends the operational life of processing equipment.

Nevertheless, during operation, DEG inevitably becomes saturated with moisture and various impurities, including salts, organic compounds, and suspended solids, which decrease its effectiveness. To restore the operational performance of diethylene glycol, a regeneration process is employed that removes unwanted components and returns DEG to the production cycle.

Objects and Methods

Formation water contains various salts (NaCl, $CaCl_2$, $MgCl_2$, etc.) that can interact with saturated diethylene glycol (SDEG).

At gas treatment facilities – specifically, at the integrated gas treatment unit (IGTU), where natural gas is separated from formation water and gas condensate – salt deposits also precipitate on the internal surfaces of equipment. The chemical and mineralogical composition of these deposits was determined, and micrographs were obtained. The corresponding data are presented in Table 1.

Table 1. *Ionic Composition of Deposits Precipitated on the Internal Surfaces of Equipment CGTP*

Name of sediment	Ionic composition of sediments, mass.%						
	Na	K	Ca	Mg	Cl	SO_4	H.o
Salt deposits CGTP	28.531	0.132	1.535	0.943	48.596	0.658	2.632

The solubility of sodium and calcium chlorides in diethylene glycol plays a significant role in natural gas purification processes. The low solubility of NaCl and the high solubility of $CaCl_2$ can lead to various issues related to contamination and salt deposition within equipment. Optimization of operating conditions and control over salt concentrations in the system can help minimize these problems.

To determine the relationship between DEG concentration and NaCl content, the solubility and density of the DEG–NaCl–H_2O system were studied over a temperature range of 20–100 °C.

Table 2 presents the solubility of sodium and calcium chlorides (DEG–NaCl–H_2O and DEG–$CaCl_2$–H_2O systems) at different temperatures.

Table 2. *Solubility of Sodium and Calcium Chlorides in DEG Solutions as a Function of Temperature and DEG Concentration*

Concentration DEG, %	Temperature,°C				
	20	40	60	80	100
Solubility of Sodium Chloride, mg/l					
40	1643	1693	1714	1786	1850
50	1167	1433	1500	1571	1601
60	737	816	1000	1200	1267
70	632	737	895	947	1033
77	375	575	775	825	875
80	344	406	600	620	670
90	225	300	400	467	517
100	183	233	317	341	367
Solubility of Calcium Chloride, mg/l					
40	1723	2525	2545	2725	2986
50	1503	1723	2004	2204	2604
60	822	982	1102	1182	1303
70	301	741	962	1082	1202
77	180	602	922	1002	1383
80	90	581	621	640	681
90	24	281	296	607	621

Results and Discussion

As the data show, with an increase in temperature from 20 °C to 100 °C, the solubility of sodium and calcium chlorides increases from 1,643 and 1,723 mg/L to 1,850 and 2,986 mg/L, respectively. At a 40% DEG concentration, within the range of 40–80% and up to 90%, the solubility of sodium and calcium chlorides decreases by a factor of approximately 4.17–5.64 and 4.31–8.99, respectively. The solubility of calcium chloride is 1.6 to 1.01 times higher than that of sodium chloride. However, in the original SDEG solution, the calcium chloride content is 3.7 times lower. Therefore, during the evaporation of SDEG to a DEG concentration of 90%, only sodium chloride precipitates, while calcium chloride accumulates in the regenerated DEG (RDEG), leading to an increase in its viscosity.

Table 3 shows that the refractive index of the system is affected by the DEG concentration and the presence of dissolved chloride salts.

Table 3. *Determination of Diethylene Glycol (DEG) Concentration Based on Refractive Index in Pure and Contaminated Solutions*

No.	Concentration DEG	Pure DEG n^{20}	Saturated Solution with Chloride Salts				$\Delta n^{20}_{д}/2$	Determination of DEG Concentration in the Sample
			NaCl	$\Delta n^{20}_{д}/2$	$CaCl_2$	$\Delta n^{20}_{д}/2$		
1.	40	1.382	1.408	0.026	1.425	0.043	0.0345	
2.	50	1.394	1.416	0.022	1.429	0.35	0.0230	
3.	60	1.407	1.422	0.015	1.438	0.031	0.0210	

No.	Concentration DEG	Pure DEG n^{20}	Saturated Solution with Chloride Salts				$\Delta n^{20}_{д}/2$	Determination of DEG Concentration in the Sample
			NaCl	$\Delta n^{20}_{д}/2$	$CaCl_2$	$\Delta n^{20}_{д}/2$		
4.	70	1.417	1.430	0.013	1.445	0.028	0.0170	
5.	77	1.425	1.435	0.010	1.449	0.024	0.0170	
6.	80	1.428	1.439	0.011	1.451	0.023	0.0170	
7.	90	1.437	1.445	0.008	1.457	0.020	0.0140	
8.	100	1.443	1.451	0.008			0.0100	
9.	SDEG	1.414						39.5
10.	30% evaporation	1.443						80.4
11.	40% evaporation	1.454						90.0
12.	50% evaporation	1.460						92.0
13.	RDEG	1.424						60.0

For example, when using a 40% DEG solution, the refractive index in the pure solution and in solutions containing sodium and calcium chlorides is 1.382, 1.408, and 1.425, respectively. The difference in refractive index ($\Delta n_{20}D$) between pure DEG and the sodium and calcium chloride solutions is 0.025 and 0.043, respectively, with an average difference of 0.0345. As the DEG concentration increases, both the $\Delta n_{20}D$ values and their average decrease to 0.008, 0.020, and 0.014, respectively.

Using this table, the DEG content in a solution can be quickly determined with any standard refractometer, with a margin of error of ±1.5%.

The studies have shown that dissolved calcium salts significantly affect the stages of spent SDEG purification. Therefore, prior to evaporation, it is necessary to investigate the decalcification process. Table 4 presents data on the effect of soda ash solution dosage on the evaporation process.

Table 4. *Effect of Soda Ash Solution Dosage on the Evaporation Process*

No.	Ratios SDEG: Soda Ash Solution (30%)	I stage		II stage (degree of allocation)	
		Degree of Precipitate Formation, %	Humidity, %	Sediment after (60%) evaporation, %	Humidity, %
1.	1:0.038	4.44	61.9	6.32	11.3
2.	1:0.061	6.20	58.0	9.35	10.5
3.	1:0.076	7.21	50.6	7.48	13.0
4.	1:0.083	7.31	72.4	8.34	4.06

The decalcification process was carried out according to the stoichiometry of the calcium carbonate formation reaction:

$$CaCl_2 + Na_2CO_3 \rightarrow CaCO_3\downarrow + 2NaCl$$

A 30% aqueous solution of soda ash (Na_2CO_3) was used as the precipitating agent for calcium ions, with the SDEG-to-soda ash solution ratio ranging from 1:0.038 to 1:0.083.

According to the data presented in the table, during the first stage of precipitation, as the ratio of SDEG to soda ash solution increases from 1:0.038 to 1:0.076, the mass of the resulting precipitate (relative to the total mass of the initial components) increases from 4.44% to 7.21%, with a moisture content of 50.6–61.9%.

At a 60% degree of evaporation, up to 9.35% of solid phase is separated, with a moisture content not exceeding 13.0%.

Table 5 and Figure 1 present the elemental composition and X-ray diffraction (XRD) patterns of the unwashed precipitate formed:

in the first stage, during calcium ion precipitation with the addition of soda ash solution;

in the second stage, during the precipitation of sodium chloride from the decalcified SDEG solution in the evaporation process.

Table 5. *Elemental Composition of Samples (Sample Numbers Correspond to Table 4)*

Element	Spectors. massa %			
	I stage		II stage	
	1	2	3	4
O	45.6	39.3	8.9	0
Ca	33.8	41.6	2.0	0
Na	8.2	8.0	34.4	41.5
Cl	8.9	7.7	54.7	58.5
Mg	3.6	3.3		

As shown in Table 5, the precipitates formed during the first stage primarily contain calcium and oxygen. The contents of sodium, magnesium, and chlorine do not exceed 8.2%, 3.6%, and 8.9%, respectively.

In the second stage of precipitation, sodium and chlorine atoms dominate, with concentrations ranging from 34.4–41.5% and 54.7–58.5%, respectively. Meanwhile, the calcium content does not exceed 2.0%.

Picture1. *X-ray of samples*

Sample № 1 (I stage)

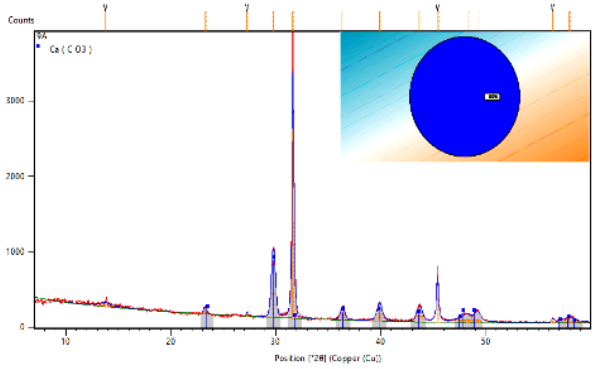

Sample № 1 (II stage)

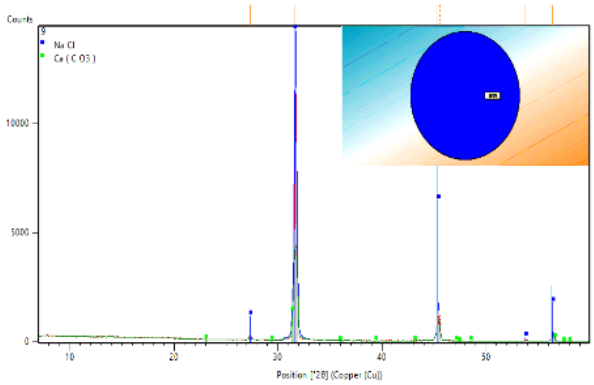

Sample № 1 (II stage)

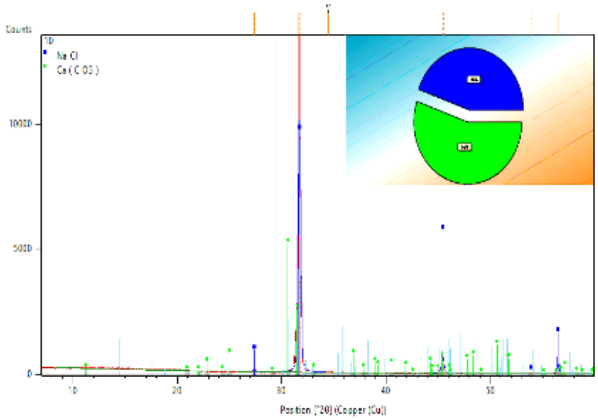

(Sample numbers correspond to those in Table 3)

Table 6. *Mineralogical Composition of the Samples*

No.	Name of mineral	Formula of mineral	Ref. code	Номер образцов		
				1 (II stage)	1' (I stage)	1' (II stage)
1.	Calcium carbonate	$CaCO_3$	01–080–9776		100%	
2.	Sodium chloride	NaCl	01–080–3969	100%		
3.	Calcium carbonate	$CaCO_3$	01–087–1863			55%
4.	Sodium chloride	NaCl	01–078–0751			45%

As can be seen from the X-ray diffraction pattern (Pic. 1), the precipitate formed during the first stage predominantly consists of calcium carbonate ($CaCO_3$), confirming the effectiveness of calcium removal through the addition of soda ash solution. In the second stage, following the evaporation of the decalcified solution, the main crystalline phase of the precipitate is sodium chloride (NaCl).

According to the obtained data, the separation process can be conventionally divided into two stages: first, calcium is removed as poorly soluble calcium carbonate; then sodium chloride is removed by evaporation. This allows for the production of a purified DEG solution, saturated with sodium and calcium chlorides, and enables regulation of its ionic composition according to specific technological requirements.

Conclusion

Sample analyses revealed that during the evaporation of spent saturated diethylene glycol (SDEG), sodium chloride crystals precipitate, while calcium chloride remains in solution. As a result of regenerated solution circulation, the Ca/Na ratio increases from 0.29 to 4.11, complicating further evaporation and deteriorating the absorption properties of the regenerated diethylene glycol (RDEG).

The conducted experiments confirmed the advantages of a staged separation process for calcium and sodium chlorides using inorganic precipitating agents – specifically, soda ash solutions. The kinetic patterns of SDEG evaporation after preliminary calcium ion precipitation were established under various residual pressure conditions.

References

Korneev A. A., Yakovlev I. M. (2004). Technology of preparation and processing of natural gas. – Moscow: Nedra, – 384 p.

Grishin A. M. (2011). Drying of natural gas: a tutorial. – Ufa: Ufa State Petroleum Technical University, – 118 p.

Reznikov A. A., Pleshkov Yu. P. (1987). Adsorbents and absorbents in the gas industry. – Moscow: Chemistry.

Perry R. H., Green D. (2007). Perry's Chemical Engineers' Handbook. 8th ed. Mc Graw-Hill.

Akhmetov G. Kh. (2009). Technology and equipment of gas processing plants. – Ufa: Ufa State Petroleum Technical University.

Marchenko A. V. (2017). Corrosion problems in the processing and transportation of natural gas. // Gas industry. – No. 7. – P. 22–25.

Chernyshev I. G., Titov V. P. (2006). Removal of salts from glycol solutions. // Petrochemistry. – Vol. 46. – No. 5. – P. 387–392.

Chandrasekaran V. (2019). Industrial Wastewater Treatment. CRC Press, – 405 p.

Kirk-Othmer (2004). Encyclopedia of Chemical Technology. – Volume 12: Glycols. Wiley-Interscience.

1Knaebel K. S. (2006). Glycol Dehydration of Natural Gas: A Do-It-Yourself Workshop. // Gas Processors Suppliers Association.

Kovács G., Vatai G. (2010). Effect of temperature and pressure on solubility of salts in glycols. // Desalination. – Vol. 251. – P. 145–150.

Aliev I. A., Mukhamedov Sh. D. (2005). Methods of analysis of water-glycol solutions. – Moscow: Chemistry.
Abdullayeva Sh.M., Mamarasulov B. S., Toirov Z. K., Erkaev A. U. (2023). Technology for the production of calcium chloride adsorbent used in gas drying from the distiller liquid of the kunhirot soda plant. IBET – volume 3, – issue 6, june. – P. 151–157.
Mamarasulov B. S., Yuldashev N.Kh., Begdullaev A. K., Reymov K. D., Toirov Z. K., Erkaev A. U. (2022). Study of the process of obtaining tableted calcium chloride from waste from the production of soda ash of Kungrad Soda Plant LLC. Universum; – No. 9 (102). September.

submitted 17.04.2025;
accepted for publication 01.05.2025;
published 29.05.2025

Contact: bekzod.mamarasulov.1993@gmail.com

Contents